

ABSTRACT

AWOSANYA, EMMANUEL OLUWASEYI. Dynamic and Structural Studies of Membrane Proteins by Oriented-Sample Solid State NMR. (Under the direction of Dr. Alexander A. Nevzorov).

Oriented Sample Solid state NMR (OS-NMR) has become an important tool for the structural studies of membrane proteins (MPs) under their nearly physiological conditions. To advance the application of the method for characterizing MPs, the development of methods, which provide highly aligned samples for MPs and new multidimensional separated local field pulses sequences, is necessary.

To accomplish the above goals, a new membrane mimetic has been developed. A 15-mer peptoid polymer has been used to stabilize DMPC lipid by forming a peptoid-based macrodisc. The peptoid macrodiscs provided a higher order parameter than the bicelles. This allowed for reconstitution of Pf1 coat protein in peptoid-macrodisc for two-dimensional OS-NMR experiments.

Moreover, the previously developed SAMPI4 pulse sequence has been modified for other types of experiments with the purpose of obtaining rotational diffusion coefficients and additional angular constraints for structure determination. The incorporation of a spin-lock period before detection in the pulse sequence enabled the measurement of orientationally dependent relaxation times in the rotating frame, or $T_{1\rho}$. A quantitative uniaxial rotational diffusion on a cone model was used to estimate inhomogeneous contribution to $T_{1\rho}$ relaxation as a function of rotational diffusion coefficient. Pf1 coat protein reconstituted in DMPC/DHPC bicelles has been used as a molecular probe to quantify the viscosity of the lipid membrane interior via measuring the rotational diffusion coefficient of the protein. The experimentally obtained diffusion coefficient values $D_{\parallel} = 8.0 \times 10^5 \text{ s}^{-1}$ and $7.7 \times 10^5 \text{ s}^{-1}$ are close to the estimated

value of $D_{\parallel} = 8 \times 10^5 \text{ s}^{-1}$ obtained from the Stokes-Einstein equation if the protein is modeled as a cylinder with the radius of gyration of 10 Å with the local bilayer viscosity of about 1 Poise.

Additionally, triple-resonance pulse sequence SAMPi4² was developed and applied to a uniformly labeled ¹³C – ¹⁵N Pf1 coat protein. The experimental aims were to utilize the Cα geometry to provide additional chiral restraints for structure determination of aligned proteins. The Cα connects side chains with the backbone and plays an important role in defining the torsion angles between the adjacent peptide planes. Therefore, exploiting the CαHα dipolar couplings in the separated local field experiments would be highly beneficial. The new proposed experiment provided an additional spectral correlation of ¹Hα - ¹³Cα dipolar couplings and ¹⁵N chemical shifts along with the usual correlation of ¹H-¹⁵N dipolar couplings and ¹⁵N chemical shifts. These angular restraints are then used to calculate torsion angles (Φ and Ψ) for Pf1 coat protein structure refinement and validation. The development of the triple-resonance pulse sequences and the development of a new membrane mimic represent new tools for investigating larger MPs using oriented sample solid state NMR.

© Copyright 2020 by Emmanuel Oluwaseyi Awosanya

All Rights Reserved

Dynamic and Structural Studies of Membrane Proteins by Oriented-Sample Solid State NMR

by
Emmanuel Oluwaseyi Awosanya

A dissertation submitted to the Graduate Faculty of
North Carolina State University
in partial fulfillment of the
requirements for the degree of
Doctor of Philosophy

Chemistry

Raleigh, North Carolina

2020

APPROVED BY:

Dr. Alexander A. Nevzorov
Committee Chair

Dr. Alex I. Smirnov

Dr. Wei-Chen Chang

Dr. David A. Shultz

DEDICATION

I dedicate this to my wonderful family and friends for all their love and support.

BIOGRAPHY

Emmanuel Oluwaseyi Awosanya was born in Lagos, Nigeria on September 7, 1983. Emmanuel started undergraduate at North Carolina State in 2001. He left to complete and receive his Bachelor of Science in Biochemistry from East Carolina University in May of 2007. After several years as a pharmaceutical analytical chemist, he moved to Los Angeles. There, he received his Master of Science in Chemistry from California State University Los Angeles in 2015. In August of 2015, he returned to North Carolina State University to start his chemistry graduate program and has been studying the structures of membrane proteins reconstituted in biological membranes using Oriented-Sample Solid-State Nuclear Magnetic Resonance under the direction of Alexander A. Nevzorov for the past five years.

ACKNOWLEDGMENTS

First, I want to thank professors: Alex Smirnov, Tatyana Smirnova, Wei-Chen Chang, David Shultz, Belinda Akpa for agreeing to be on my committee. I would especially like to thank my advisor Dr. Alexander Nevzorov, whose great mentorship and support has made these five years a wonderful, successful period. I want to thank the current and past member of the Nevzorov group. Thank you, Sophie and Deanna, for showing me the way and helping me get started. I want to thank many of my friends who have made my graduate program enjoyable. Thank you, Sergey and Melanie, for your friendship.

Lastly, I would like to thank my family, my brother and sisters who have always supported and encouraged me. To my father and mother, thank you for inspiring me and for the many prayers and support, e seun!

TABLE OF CONTENTS

LIST OF TABLES	vii
LIST OF FIGURES	viii
Chapter 1: Introduction	1
1.1 Membrane Protein: Significance and Structure Determination	1
1.2 Current techniques for membrane protein structure determination	2
1.3 Solid-state NMR of lipid aligned protein: Methods and Pulse Sequences	4
1.3.1 Theoretical Description for Solid State NMR experiments	6
1.3.2 Sensitivity Enhancement Pulse Sequences	7
1.3.3 Separated Local Field Pulse Sequences	13
1.3.4 Data Analysis	16
1.4 Summary of Present Research	19
References	20
Chapter 2 Peptoid-Membrane mimetic For Oriented Sample NMR Studies	
.....	23
2.1 Abstract	23
2.2 Introduction	24
2.3 Peptoid-Macrodisc	27
2.4 Materials and Methods	29
2.5 Results and Discussion	32
2.6 Conclusion	40
References	41

Chapter 3 Membrane Protein Rotational Dynamics Probed by Anisotropic NMR Relaxation ..	46
3.1 Abstract	46
3.2 Introduction.....	47
3.3 The diffusion-on-a-cone model for $T_{1\rho}$ Relaxation.....	49
3.4 Materials and Methods.....	55
3.5 Results and Discussion	57
3.6 Conclusion	63
References.....	65
Chapter 4 Chiral $^{13}\text{C}\alpha\text{1H}\alpha$ Couplings Detection for Membrane Protein Structure	
Determination by Solid-State NMR.....	70
4.1 Abstract	70
4.2 Introduction.....	72
4.3 Methods.....	74
4.4 Results and Discussion	75
4.5 Conclusion	85
References.....	86
APPENDICES	91
Appendix A: MATLAB codes for $T_{1\rho}$ rotational diffusion calculation.....	92
Appendix B: Triple Resonance pulse program with SAMPI4 ² and MMHH Blocks	96

LIST OF TABLES

Table 2.1	DLS size distribution report parameters.....	32
Table 3.1	Anisotropic rotating-frame relaxation times and rates for Pf1 coat protein residues (26-42).....	58
Table 3.2	Parameters obtained from diffusion on cone model determined by $T_{1\rho}$ relaxation..	63

LIST OF FIGURES

CHAPTER 1 INTRODUCTION

- Figure 1.1 Representation of a cell membrane consisting of a phospholipid bilayer, glycolipids, cholesterol, and proteins.
https://teaching.ncl.ac.uk/bms/wiki/index.php/Membrane_protein caption text..... 2
- Figure 1.2 A. Schematic representation of aligned ‘unflipped’ bicelles: the bilayer normal is perpendicular to the direction of the external static magnetic field and B. Parallel or ‘flipped’ bicelles: in the presence of YbCl_3 , the bilayer normal is parallel to the static magnetic field. (9) 4
- Figure 1.3 A. Characteristic features of membrane proteins in bicelles. From left to right are isotropic reorientation to immobile, and no alignment to complete alignment. The samples are described by the lipid molar ratio q . B. Bicelle alignment temperature per percentage of DMPC at different q . (1) 5
- Figure 1.4 Cross-polarization pulse sequences: A. HHCP, B. CP-MOIST, and C. REP-CP. (21,22)..... 7
- Figure 1.5 Constant-time 1D spectra of Pf1 in unflipped bicelles containing 5-DOXYL stearic acid radical: CP-MOIST (black; acquired with 50 kHz rf B_1 fields, 6 s recycle delay and 140 scans); low-power REP-CP (blue; acquired with 18 kHz rf B_1 fields, 6 s recycle delay and 128 scans); low-power REP-CP (red; acquired with 18 kHz rf B_1 fields, 0.6 s recycle delay and 698 scans). The total experimental time is ~14 min in each spectrum. (23) 11
- Figure 1.6. Constant-time 1D spectra of Pf1 in Yb^{3+} -flipped bicelles containing 5-DOXYL stearic acid radical: CP-MOIST (black; acquired with 50 kHz B_1 field, 6 s recycle delay and 256 scans); low-power REP-CP (blue; acquired with 35 kHz B_1 field, 6 s recycle delay and 256 scans); low-power REP-CP (red; acquired with 35 kHz B_1 field, 0.7 s recycle delay and 1172 scans). The total experimental time is 25.6 min in each spectrum(23)..... 12
- Figure 1.7 A peptide plane showing the peptide plane coordinate system, the orientation of which relative to the laboratory frame (the external magnetic field) is probed in oriented-sample solid-state NMR experiments. (1)..... 13

Figure 1.8	Pulse sequences for 2D SLF experiments. A. PISEMA pulse sequence with 180° phase shift between even and odd t_1 dwells. B. Magic-sandwich-based SAMPI4. C. Experimental PISEMA spectra of Pf1 coat protein reconstituted in flipped bicelles containing 5-DOXYL stearic acid radical and utilizing either single-contact CP-MOIST (black contours) or REP-CP (red contours) transmembrane helical region (G23-L43) are assigned. D. Experimental SAMPI4 spectrum of Pf1 coat protein in unflipped bicelles with transmembrane helical region (I26-M42) assigned. (1, 23).....	15
Figure 1.9	Diagram of the ideal helix tilt (τ) and rotational pitch (ρ) angle that are reflected in the PISA wheel. The vector (a) defines the cylindrical axis of the helix.....	16
Figure 1.10	Simulated ^1H - ^{15}N SLF spectra (left panels) and plots of the ^1H - ^{15}N dipolar coupling (right panels) showing dipolar waves for α -helical structures with different kinks or curvature. (1)	17
Figure 1.11	Confirmation of the previous spectroscopic assignment of the transmembrane helix of Pf1 coat protein in parallel bicelles obtained by a superposition of PISEMA spectrum (blue contours and NN exchange spectrum Red lines show connectivities between the main peaks in the PISEMA spectra and cross peaks in the NN exchange spectrum passing via the main diagonal peaks.	18
 CHAPTER 2 UTILIZING PARAMAGNETIC RELAXATION ENHANCEMENT IN ORIENTED BIOLOGICAL NMR SAMPLES		
Figure 2.1	Nanodiscs vs Macrodiscs, along with their ^{31}P alignments. Figure reproduced from source: (17).....	26
Figure 2.2	Schematic for synthesis of 15-mer peptoid, Chemical Formula $\text{C}_{127}\text{H}_{150}\text{N}_{16}\text{O}_{26}$, 2.3 kDa	30
Figure 2.3	Dynamic light scattering (DLS) particle size distribution by intensity. A. Sample measured at 40° C. B. sample measured at 25° C.....	33
Figure 2.4	^{31}P chemical shift NMR spectra of peptoid-Macrodisc's DMPC bilayer. Sample temperatures A-F (32 °C, 35 °C, 37 °C, 40 °C, 43 °C, 50 °C).	35
Figure 2.5	A. ^{31}P chemical shift NMR spectrum of Pf1 reconstituted in peptoid-macrodisc, sample temperature at 40 °C. B. ^{15}N chemical shift NMR spectrum of Pf1 coat protein reconstituted in peptoid-macrodisc at 40 °C	36
Figure 2.6	2D NMR spectra of Pf1 reconstituted in different membrane mimics; in blue (3.2 DMPC/DHPC bicelles), in red (belt peptide-DMPC macrodisc), and in green (15-mer peptoid-DMPC macrodisc).....	38

Figure 2.7 A. 2D NMR spectra of Pfl coat protein in peptoid-DMPC macrodisc with 20 transmembrane residues assigned. B. Dipolar wave profile of Pfl coat protein transmembrane domain with the expected periodicity of 3.6, which is indicative of the angular anisotropy of dipolar couplings for the alpha helix. 39

CHAPTER 3 MEMBRANE MIMETICS FOR MEMBRANE PROTEIN STRUCTURAL STUDIES VIA SOLID-STATE NMR

Figure 3.1 Inhomogeneous ^{15}N CSA linewidths in perpendicular bicelles calculated for an ideal alpha-helix tilted at 20° with respect to the axis of rotation at various values of the diffusion coefficient as indicated. At the value $D_{\parallel} = 5 \times 10^5 \text{ s}^{-1}$ theoretical rotational contribution to the ^{15}N CSA linewidths is less than 15 Hz (or about 0.3 ppm at ^1H 500 MHz NMR frequency). Slower rotational diffusion is manifested by larger anisotropy of linewidths at the perpendicular alignment of the bilayers 50

Figure 3.2 A modified SLF SAMPI4 pulse sequence incorporating a prelock of duration T for measuring individual $T_{1\rho}$ ' for the resolved peaks in the 2D SLF spectrum..... 57

Figure 3.3 A. SAMPI4 spectrum of Pfl coat protein obtained at 500 MHz ^1H frequency with assigned residue peaks for the transmembrane domain used for the fitting of anisotropic $T_{1\rho}$ relaxation times (assignment taken from ref. (48)). B. Six (6) representative ^{15}N relaxation profiles corresponding to the individual resonances L38, M42, V31, V35, G28, and I26 in the Pfl SAMPI4 spectra (normalized by the first-point intensity) as a function of spin lock time fitted to single-exponential decays. 59

Figure 3.4 A correlation plot of $R_{1\rho}$ and bond factor $\sin^4(\theta_B)$, where θ_B is the angle that an NH bond makes with the axis of rotation. The rotational diffusion coefficient $D_{\parallel} = 8.0 \times 10^5 \text{ s}^{-1}$ was deduced from linear regression using Eqs. 10 and 12 with the linear regression coefficient, $R^2=0.86$. Error bars correspond to a 95% confidence interval of relaxation rates determined by the exponential fits in the spin-locking experiments..... 60

Figure 3.5 A. Dipolar waves of Pfl coat protein transmembrane domain with the expected periodicity of 3.6, which is indicative of the angular anisotropy of dipolar couplings for the alpha helix. B. $R_{1\rho}$ relaxation profile for the assigned residue peaks for the TM region of Pfl. Wave-like behavior of the $R_{1\rho}$ relaxation rates allows one to extract the value of the diffusion coefficient of $7.7 \times 10^6 \text{ s}^{-1}$ when the helix tilt of 22.3° from part A is used in the fit. The error bars correspond to 95% confidence interval of relaxation rates determined by exponential fits from the spin-locking experiments (Fig. 2.3B and Table I)..... 61

CHAPTER 4 PROBING STRUCTURAL CONSTRAINTS IN LARGE MEMBRANE PROTEINS

- Figure 4.1 The developed pulse sequence for detecting $^1\text{H}\alpha$ - $^{13}\text{C}\alpha$ couplings at ^{15}N sites suitable for uniformly labeled (^{15}N , ^{13}C) aligned samples 76
- Figure 4.2 A. Simulation of the pulse sequences SAMPI4² (blue) and SAMPI4 (green) for an 8-spin system at B_1 rf field of 60 kHz with the dipolar couplings as indicated in the inset. B. Experimental SAMPI4² spectrum exhibits good dipolar resolution (ca. 200 Hz FWHH linewidths) when applied to ^{15}N labeled n-Acetyl Leucine single crystal. 76
- Figure 4.3 ^{13}C -detected 2D SAMPI4 spectra of Pfl coat protein reconstituted in magnetically aligned DMPC/DHPC bicelles correlating ^1H - ^{13}C dipolar couplings with ^{13}C chemical shifts (blue contours). Blank DMPC-DHPC bicelle SAMPI4 spectrum is shown as red contours for direct comparison. The identified ^{13}C resonances originating from the C_α carbons and the Carbonyl of Pfl coat protein is outlined in by the green boxes77
- Figure 4.4 A. Optimization of the triple MMHH conditions using ^{15}N -detected magnetization transfer from the ^{13}C spins. B. ^{15}N detected MMHH transfer spectra with proton channel power on (blue) and only the proton power off (green) and with only the carbon power off (red).....78
- Figure 4.5 A. Overlay of ^{15}N -detected SLF ^1H - ^{15}N (red contours) and $^1\text{H}\alpha$ - $^{13}\text{C}\alpha$ dipolar couplings (blue contours) measured for doubly labeled sample of Pfl coat protein reconstituted in magnetically aligned bicelles. Selectively labeled ($^{13}\text{C}_\alpha$, ^{15}N) Valine spectrum is shown in brown contours. Assignment of the $^1\text{H}\alpha$ - $^{13}\text{C}\alpha$ dipolar couplings is shown by the text in magenta color. B. Structural fitting of the digitized data (circles) showing the fitted frequency values (crosses)..... 80
- Figure 4.6 Linear-regression correlation plots for the simultaneously fitted ^{15}N CSA and ^1H - ^{15}N and $^1\text{H}\alpha$ - $^{13}\text{C}\alpha$ couplings for Pfl coat protein 82
- Figure 4.7 A. Final search values for torsion angles on the Ramachandran map for 2D vs 3D NMR data fit for 1000 calculated structures. A clustering near the α -helical torsion angles are apparent for the 3D fit. No restriction on the torsion angles were assumed a priori for the fitting. B. ROSETTA top-down filtering protocol. C. Consensus family of Pfl TM structures determined from NMR.....83

CHAPTER 1

Introduction

1.1 Membrane Proteins: Significance and Structure Determination.

Membrane proteins represent one of three main classes of proteins which either interact with or are embedded inside biological membranes. Membrane proteins are involved in many essential biological processes such as transport of ions, chemical signaling, and energy transduction (1). Membrane proteins make up about 20–30% proteins encoded by open reading frames (2,4,5). Diseases such as cancer and diabetes are often connected to malfunctioning and sometimes misfolding of membrane proteins (4,6). There is considerable commercial interest in membrane proteins because of their essential roles in cellular functions, and more than 50% of all human drugs target G-protein coupled receptors (GPCRs) and ion channels (3). The other two groups of proteins (fibrous and globular) make up the majority of the structures deposited in the protein data bank (PDB), since they are mostly water-soluble and, therefore, are relatively easy to crystalize for X-ray crystallography or solubilize for solution NMR spectroscopy. Membrane proteins, in contrast, reside in a hydrophobic bilayer, which makes it challenging to solubilize. As a consequence, membrane proteins make up only about 1-2% of the total 100,000 protein structures deposited in the Protein Data Bank. This has led to a boost in research efforts in order to elucidate the tertiary structure, dynamics, and functions of membrane proteins.

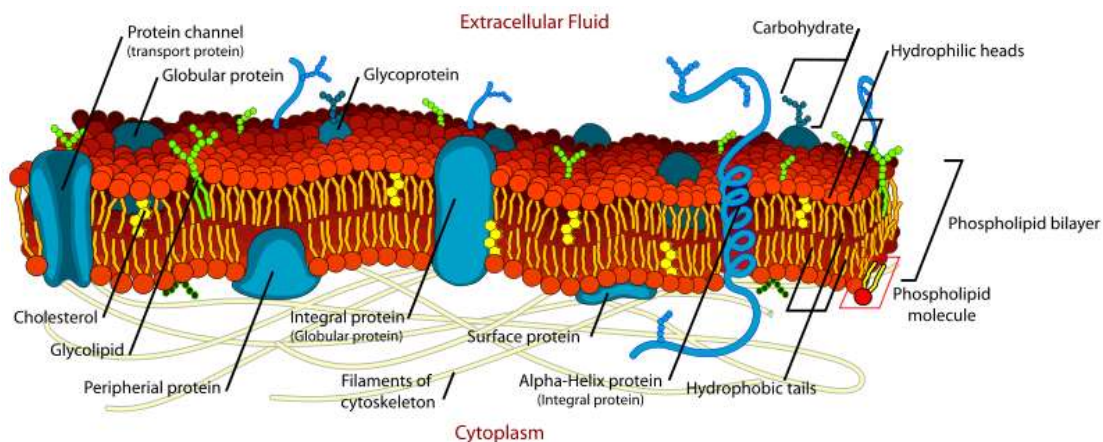


Figure 1.1. Representation of a cell membrane consisting of a phospholipid bilayer, glycolipids, cholesterol, and proteins. From the website:

https://teaching.ncl.ac.uk/bms/wiki/index.php/Membrane_protein

1.2 Current techniques for membrane protein structure determination

High-quality 3D crystals, which are needed for XRD studies, are difficult to grow for membrane proteins. The difficulties in attaining high-quality crystals stem from using detergents to solubilize the membrane protein for crystallization. Even in cases when crystallization is successful (17), the crystal lattice may alter the protein structure because it is not determined in the native lipid bilayer (1,18). Solution NMR spectroscopy can also be used to determine structures of membrane proteins that are solubilized in detergents such as lipid detergent micelles, isotropic bicelles, and lipid nanodisc (9). However, its general application for membrane protein structure determination may also be problematic due to solubilization by detergent. For instance, micelles have strong curvature on the surface, which may affect the orientation of transmembrane helices by causing significant strain in attached helical peptides (10,11,12). In addition, the membrane protein/lipid assemblies are often too large to possess the required short correlation time, thereby resulting in poorly resolved solution NMR spectra (1). Therefore, other techniques such as Solid-state NMR and Cryo-EM that do not require crystals

and fast molecular reorientation (1) are becoming more broadly used to solve membrane protein structures.

The conformations of membrane proteins are dependent on its environment as a stably folded membrane protein interacts with the lipid bilayer hydrocarbon core, the bilayer interface, and with water. The membrane proteins in lipid bilayer have dynamic and anisotropic mobility while immobilized in the bilayer, which is ideal for ssNMR (6,13). In solid-state NMR spectroscopy the nuclear spin interactions are not averaged to isotropic values by fast molecular motions as they are in solution NMR spectroscopy, which leads to informative orientation-dependent (anisotropic) dipolar interactions and chemical shift anisotropies. High-resolution atomic structure is solved by solid state NMR in two different approaches. The first is the magic-angle spinning (MAS) ssNMR, which requires fast spinning of the sample about an axis tilted with the magic angle ($\theta_{MA}=54.7^\circ$) relative to the external magnetic field B_0 . This method causes the anisotropic parts of the nuclear spin interactions to be averaged providing narrow lines. The desired parts of the anisotropic dipolar interactions may then be reintroduced by various recoupling techniques such as REDOR (1,7). The second approach is solid state NMR of aligned samples; this can be done mechanically by aligning the lipid membrane between glass plates (14) or in anodized aluminum oxide (AAO) nanopores (15) forming uniaxially oriented bilayers. Alternatively, membrane proteins can also be aligned spontaneously in a magnetic field due to the large anisotropic magnetic susceptibility of phospholipids in mixtures of small and long chain lipids, which form assemblies called bicelles (16). The newer membrane mimetic called “macrodiscs” can also align spontaneously in a magnetic field whether stabilized by either a belt-peptide or styrene maleic acid polymer (17,37).

1.3 Solid-state NMR of lipid-aligned proteins: Methods and Pulse Sequences

A fully hydrated lipid membrane is needed for determining structures of membrane proteins in their native-like environments. Magnetically aligned bicelles are widely used and advantageous due to the ease of preparation and use of a sealed sample tube, which enables placement inside a solenoid coil for optimal probe performance. The bicelles consist of long chain lipids that form the planar bilayers and are capped at the edges by short-chained lipids. Bicelles are uniaxially aligned with the bilayer normal perpendicular to the external magnetic field or can be flipped so that the bilayer normal would be parallel to the field with lanthanides. (Figure 1.2). Protein structures can be determined in both alignments.

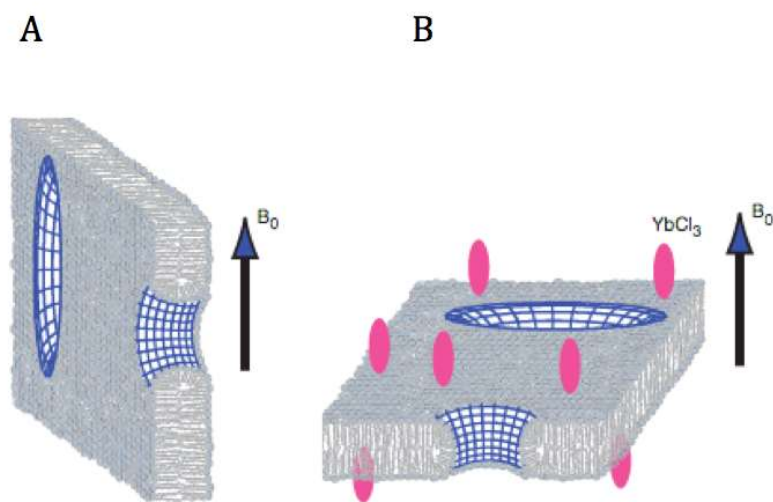


Figure 1.2. A. Schematic representation of perpendicular or ‘unflipped’ bicelles with the bilayer normal perpendicular to the direction of the external static magnetic field and B. Parallel or ‘flipped’ bicelles: in the presence of $YbCl_3$, the bilayer normal is parallel to the static magnetic field. (9)

Sample preparation is critical to obtaining alignment as shown in Figure 1.3 (1), the ratio of the long-to-short chain lipid referred as q value ~ 3 is preferred. The alignment is also temperature and concentration dependent. The alignment of the bicelle by strong magnetic field forms a liquid crystalline phase with order parameter 0.75-0.83 (9).

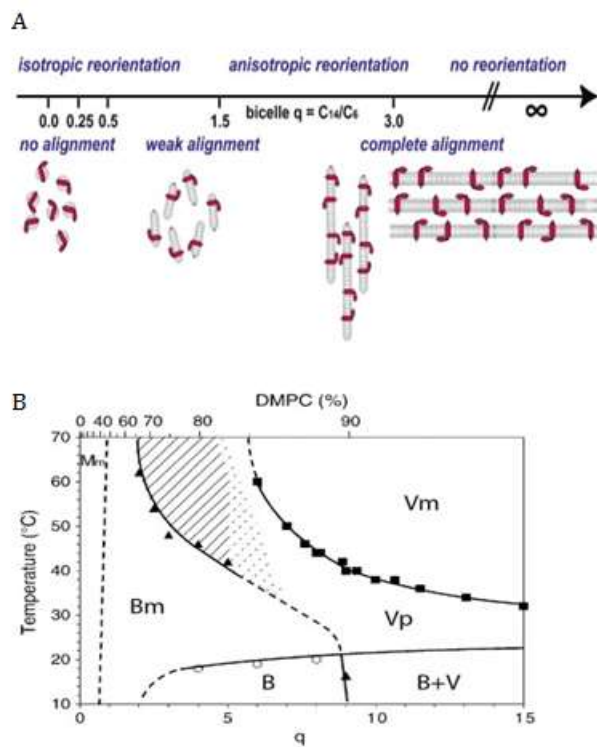


Figure 1.3. A. Characteristic features of membrane proteins in bicelles. From left to right are isotropic reorientation to immobile, and from no alignment to complete alignment. The samples are described by the lipid molar ratio q . B. Bicelle alignment temperature per percentage of DMPC at different q . (1)

Using oriented sample OS (oriented sample) solid-state NMR the conformations of membrane protein can be measured by the orientation dependence of the chemical shift and heteronuclear dipole-dipole interactions associated with ^1H , ^{13}C , and ^{15}N nuclei in labeled sites.

1.3.1 Theoretical Description for Solid State NMR Experiments.

The structural constraints yielded from ssNMR are done by the manipulation of interactions of nuclear spin magnetic moments with the static magnetic field and time-dependent radiofrequency irradiation. The following Hamiltonian in the laboratory frame can describe the total energy of the interactions of the system:

$$H = H_I^Z + H_S^Z + H_I^{rf} + H_S^{rf} + H_{II}^D + H_{SS}^D + H_{IS}^D \quad \text{Eq 1.1}$$

The H^Z , H^{rf} and H^D are Hamiltonians for the Zeeman, rf (radio frequency) and dipole-dipole interactions for the abundant I and dilute S spins. The spin magnetization before application of and rf pulse is described by normalized density matrix $\rho(0)$:

$$\rho(0) = \frac{I_x^{(initial)}}{2^{(N-2)}} \quad \text{Eq 1.2}$$

In the doubly rotating frame, the density matrix evolves in time under the simplified Hamiltonian that is governed by the strongest interactions. This is done in order to truncate the terms that do not commute with the high magnetic field interaction. The time dependent terms are eliminated by the use of average Hamiltonian theory leaving the terms that are time independent after the rotating frame transformation. The heteronuclear Hamiltonian in the simplest two-spin case can be written as:

$$\bar{H} = \omega_I I_x^{total} + \omega_S S_x^{total} + dI_z S_z \quad \text{Eq 1.3}$$

The density matrix evolved is under the exponential Hamiltonian operator to obtain observable S spin signal

$$\langle S_x^{(k)} \rangle = \text{Trace} \left(S_x^{(k)} e^{-iHt} \rho(0) e^{iHt} \right) \quad \text{Eq 1.4}$$

The real part of the observable $S_x(t)$ represents the dilute ^{15}N spin magnetization at any given time, t , during the pulse sequence.

1.3.2 Sensitivity Enhancement Pulse Sequences

The detection of dilute spins such as ^{15}N or ^{13}C by ssNMR suffers from low sensitivity. The pulse sequences stemming from the pioneering work of Pines and Waugh (18) increase the S/N in the spectra of dilute spin systems. The Cross Polarization (CP) experiments are accomplished by pulse sequences illustrated in Figure 1.4, these experiments take advantage of the long T_1 (spin-lattice relaxation) times in solid samples and uses ^1H spins as a polarization and relaxation reservoir to enhance the signal of the dilute spins, decoupling ^1H spins in order to decrease line broadening caused by the larger one-bond dipolar coupling of dilute spins to ^1H , and the short T_2 spin-spin relaxation in solid state.

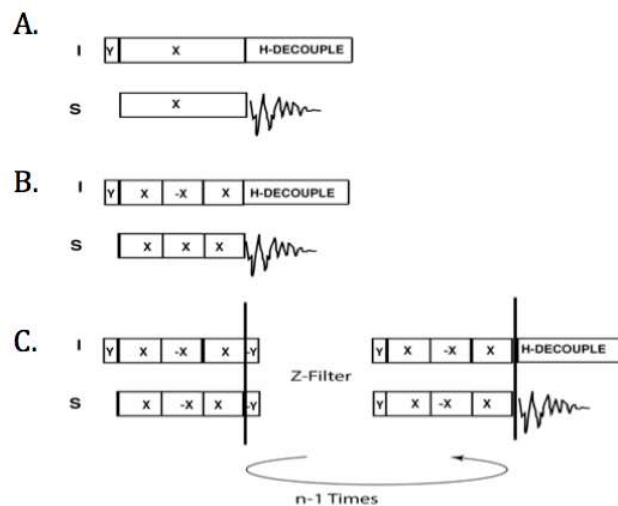


Figure 1.4. Cross-polarization pulse sequences: A) HHCP, B) CP-MOIST, and C) REP-CP. (21,22)

The pulse sequences start by an application of $\pi/2$ pulse to the abundant I spin system. This is followed by spin-locking (SL) RF field applied to both I and dilute S spin system, adjusting the frequency at which the I and S spin magnetization precesses in the doubly tilted rotating frame to facilitate thermal contacts between spin system and polarization transfer. The efficient transfer of polarization between large polarized ^1H spins and low polarized dilute spins occurs when the precessing frequencies in the doubly rotated frame are adjusted to reach the Hartmann-Hahn matching condition (19).

$$\gamma_I B_{1I} = \gamma_S B_{1S} \quad \text{Eq 1.5}$$

The dilute S spin signal enhancement due to the Cross-Polarization process can be examined through the spin temperature concept. The I spin system before the $\pi/2$ pulse has a population ratio given by the Boltzmann equilibrium distribution in the high-temperature approximation

$$\frac{N_-}{N_+} = \exp\left(\frac{-\hbar\omega_0}{kT_L}\right) \approx 1 - \frac{\hbar\omega}{kT_L} \quad \text{Eq 1.6}$$

T_L is the temperature of the lattice, using the conventions:

$$\beta_L = \hbar/kT_L; \Delta N = N_+ - N_-; N_+ \approx N_- \approx N/2 \quad \text{Eq 1.7}$$

N is the total number of spins. Therefore, before the $\pi/2$ pulse the magnetization of the I spin system can be represented by the population difference according to Boltzmann distribution:

$$\Delta N = \frac{N\omega_0\beta_L}{2}; \quad \text{Eq 1.8}$$

After the $\pi/2$ pulse and the application of the spin lock, the new equilibrium of the I spin system is reestablished quickly such that the population difference is:

$$\Delta N = \frac{N\omega_{1I}\beta_I}{2} \quad \text{Eq 1.9}$$

Given that the I spin system population difference, ΔN , is initially preserved, we get:

$$\omega_0\beta_L = \omega_{1I}\beta_I ; \quad \text{Eq 1.10}$$

The I spin system is now considered to be at a very cold temperature relative to that of the lattice based on the ratio of the strong external magnetic field to that of the I spin system spin lock field.

$$\frac{\beta_I}{\beta_L} = \frac{T_L}{T_I} = \frac{\omega_0}{\omega_{1I}} = \frac{B_0}{B_{1I}} \quad \text{Eq 1.11}$$

The S spin system is also spin locked by B_{1S} field and I and S spin systems are in good thermal contact when the Hartmann-Hahn condition is satisfied, the spin systems will equilibrate so that their spin temperatures are equal.

$$\beta'_S = \beta_I = (B_0\beta_L) / B_{1I} = (\gamma_I / \gamma_S)(B_0 / B_{1S})\beta_L \quad \text{Eq 1.12}$$

During the equilibrating thermal contact, the abundant I spin temperature is assumed to be

unchanged because the $N_I \gg N_S$. The S spin system temperature during CP thermal contact is

significantly decreased. This yields an increase in the population difference of the S spin states

and the sensitivity of the S spin is enhanced. The theoretical enhancement from the CP

experiment is, therefore, given by a ratio of the gyromagnetic ratios of the abundant spins to that

of the dilute spins $(\frac{\gamma_I}{\gamma_S})$.

The signal is thus expected theoretically to be enhanced by a factor of 10 if the dilute spins are

^{15}N or by 4 when the dilute spins are ^{13}C . The ideal enhancement is often difficult to attain due

to thermodynamic limits (i.e. the finite ratio of the high and low gamma spins) and spin lattice relaxation time in the rotating frame or $T_{1\rho}$ relaxation.

Several CP schemes such as CP with mismatch-optimized IS transfer (CP-MOIST) (20) and repetitive CP (REP-CP) (21) have been developed in order to optimize the CP experiment and overcome thermodynamic limits and experimental problems such as sample heating. REP-CP provides multiple polarization contacts to allow for an efficient transfer of polarization and overcome the thermodynamic limits. Optimizing the contact time and using low RF power can give significant signal increase when compared to single contact CP-MOIST in ^{15}N spectra (22). As seen in Fig 1.5, the combination of optimized REP-CP contact time, low power RF, and the paramagnetic relaxer 5-doxyl stearic acid radical embedded in the bicelle lead up to three-fold enhancement in signal-noise-ratio (23). The rate at which the nuclear magnetization reapproaches thermal equilibrium upon the spin-lock and the ultimate signal enhancement depends on the spin lattice relaxation time ($T_{1\rho}$). In parallel (flipped bicelles) which have larger dipolar coupling in comparison to unflipped perpendicular bicelles, using too low RF power leads to loss of spin-lock and decrease in cross polarization efficiency. The decrease in cross polarization efficiency yields the lower signal-noise ratio shown in Fig 1.6 (23). Moreover, measuring this value can provide important dynamic information about the bilayer viscosity and will be discussed in greater detail in the following chapter.

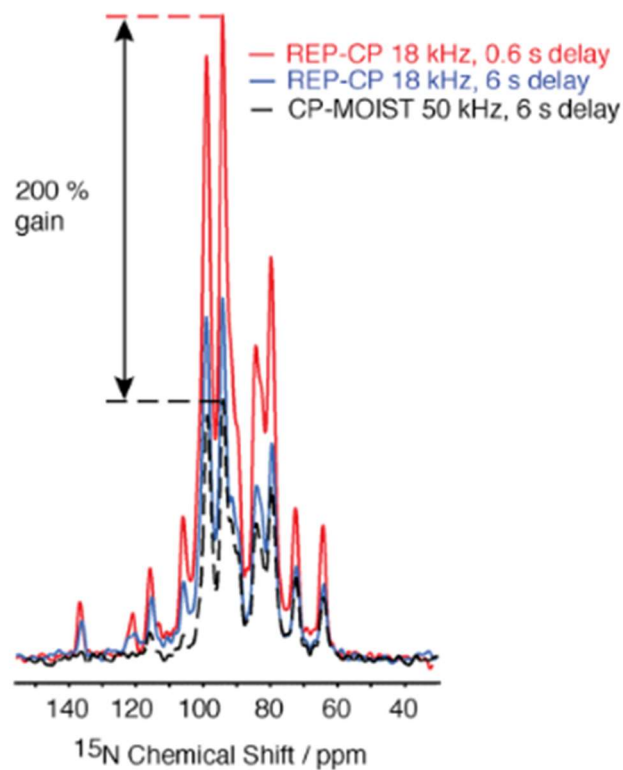


Figure 1.5. Constant-time 1D spectra of Pf1 in unflipped bicelles containing 5-DOXYL stearic acid radical: CP-MOIST (black; acquired with 50 kHz rf B 1 fields, 6 s recycle delay and 140 scans); low-power REP-CP (blue; acquired with 18 kHz rf B 1 fields, 6 s recycle delay and 128 scans); low-power REP-CP (red; acquired with 18 kHz rf B 1 fields, 0.6 s recycle delay and 698 scans). The total experimental time is ~14 min in each spectrum. (23)

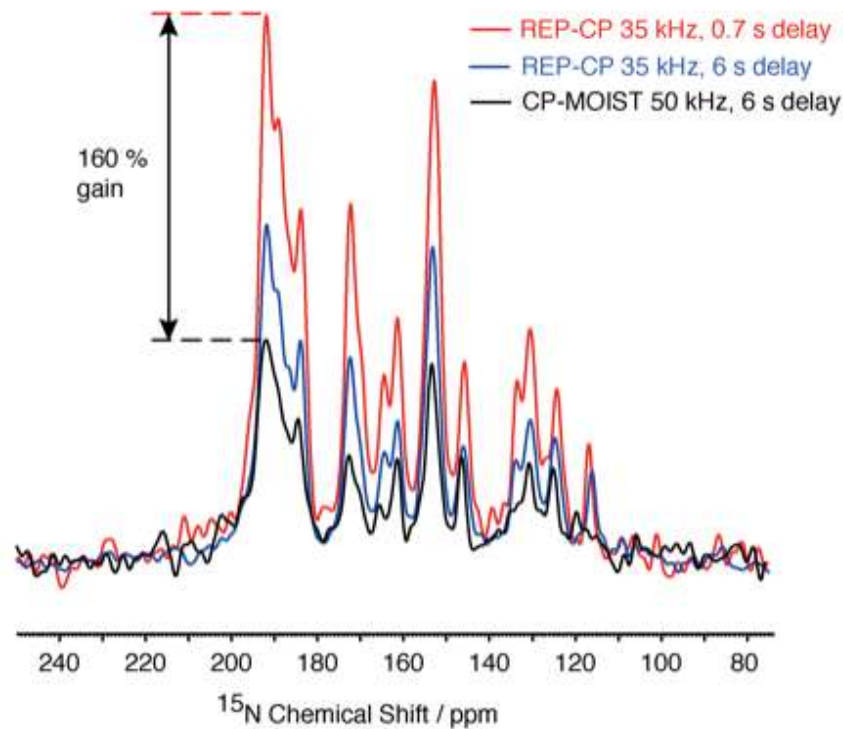


Figure 1.6. Constant-time 1D spectra of Pf1 in Yb³⁺-flipped bicelles containing 5-DOXYL stearic acid radical: CP-MOIST (black; acquired with 50 kHz B_1 field, 6 s recycle delay and 256 scans); low-power REP-CP (blue; acquired with 35 kHz B_1 field, 6 s recycle delay and 256 scans); low-power REP-CP (red; acquired with 35 kHz B_1 field, 0.7 s recycle delay and 1172 scans). The total experimental time is 25.6 min in each spectrum. (23)

1.3.3. Separated Local Field Pulse Sequences

Multidimensional Separated Local Field (SLF) (24) experiments such as PISEMA sequence (Polarization Inversion Spin Exchange at the Magic Angle) and SAMPI4 (“Sandwich-Assisted Magnetic Microscopy” or SAMMY with a $\pi/4$ pulse corrections for the finite $\pi/2$ pulses) can directly measure the ^1H - ^{15}N dipolar coupling of the protein amide site. The ^1H - ^{15}N dipolar coupling of the protein amide sites gives information about distance between coupled nuclei and the orientation of the internuclear vector (Figure 1.7) with respect to the applied field.

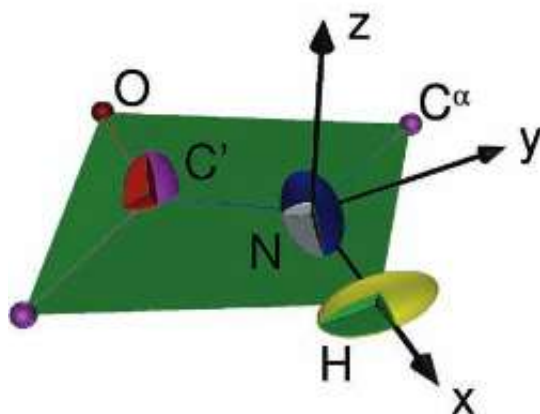


Figure 1.7. A peptide plane showing the peptide plane coordinate system, the orientation of which relative to the laboratory frame (the external magnetic field) is probed in oriented-sample solid-state NMR experiments. (1)

SLF sequences as shown in Figure 1. 8 allow for correlating the ^1H - ^{15}N dipolar couplings with ^{15}N chemical shifts. Developed by Wu et al, PISEMA (25) pulse sequence uses spin exchange at the magic angle during t_1 period. By using the frequency-switched (flip-flop) Lee–Goldburg (FSLG) spin lock (26), the ^1H - ^1H homonuclear dipole–dipole couplings are decoupled during the t_1 period and a Hartmann–Hahn-matched spin lock on the ^{15}N removes the chemical shift evolution. The ^1H - ^{15}N heteronuclear dipole–dipole coupling is retained in the indirect

dimension, and the ^{15}N chemical shift is detected in the direct dimension (1). While it is widely utilized for membrane protein determination (27), PISEMA is challenging to set up due to its high sensitivity to the RF field strengths and the ^1H carrier offsets during the off-resonance Lee–Goldburg irradiation for homonuclear decoupling of the abundant ^1H spins (1,28). The PISEMA spectra can have some resonances that are narrower and more intense than others. To overcome the sensitivity to carrier offsets, SAMPI4 implements the ‘magic sandwich’ pulse that utilizes on-resonance rather than off-resonance irradiation as in frequency-switched Lee–Goldburg to achieve homonuclear ^1H decoupling. SAMPI4 (28) pulse yields linewidths similar to those of PISEMA (<200 Hz in the heteronuclear dipolar coupling frequency dimension) with the advantage of covering the broad ranges of frequencies encountered in aligned samples of proteins at high fields (28). The typical two-dimensional experiment can take several days to complete, the induction of paramagnetic relaxation enhancement (PRE) by adding 5-doxyl stearic acid shortens the recycle delay times and allows acquisition of more signal per time (23). Spin correlations can be established by adding the proton mediated polarization transfer under 90-95% mismatched Hartmann-Hahn (MMHH) conditions. This effect relies on the strong ^1H - ^1H dipolar couplings to transfer magnetization from a ^{15}N site to its ^{15}N neighbors and can perform up to 6.7 Å (29). Briefly, this is achieved by converting the Zeeman order of energy for the ^{15}N spins to the dipolar order of the proton bath and then back to the Zeeman order of the distant ^{15}N spin.

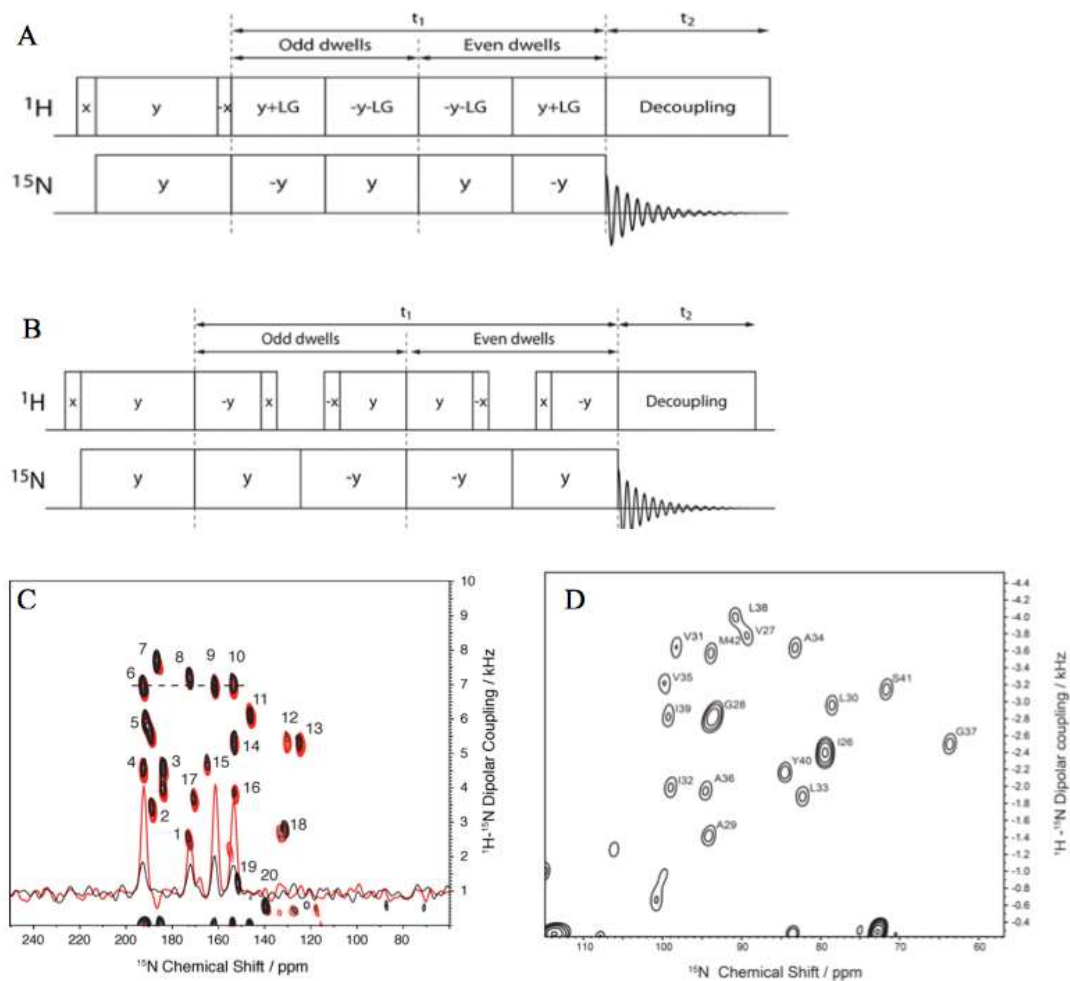


Figure 1.8. Pulse sequences for 2D SLF experiments. A. PISEMA pulse sequence with 180° phase shift between even and odd t_1 dwells. B. Magic-sandwich-based SAMPI4. C. Experimental PISEMA spectra of Pf1 coat protein reconstituted in flipped bicelles containing 5-DOXYL stearic acid radical and utilizing either single-contact CP-MOIST (black contours) or REP-CP (red contours) transmembrane helical region (G23-L43) are assigned. D. Experimental SAMPI4 spectrum of Pf1 coat protein in unflipped bicelles with transmembrane helical region (I26-M42) assigned. (1, 23)

1.3.4 Data Analysis

A wheel-like spectral pattern representing the projections of the amino acid residues in uniformly labeled samples according to the angle of the transmembrane helical axis with respect to the magnetic field can be deduced from the 2D spectra such as PISEMA and SAMPI4. These patterns are called PISA (Polarity Index Slant Angle) wheel (31,32). The wheel pattern reflects the tilt (slant angle) of the helix and the assignment of the resonances in the 2D spectra reflects the rotation (polarity index) of the helix. The ^1H - ^{15}N dipolar coupling for a particular N-H bond in the helix is calculated as a function of the angle τ , i.e. the angle the long axis helix makes with respect to the applied field (Figure 1.9) (1,33).

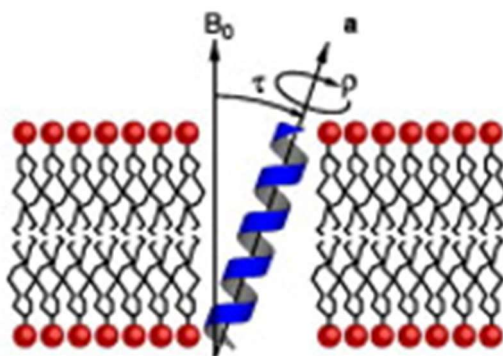


Figure 1.9. Diagram of the ideal helix tilt (τ) and rotational pitch (ρ) angle that are reflected in the PISA wheel. The vector (\mathbf{a}) defines the cylindrical axis of the helix. (27)

Plotting the residue number for a α -helix protein against ^1H - ^{15}N dipolar coupling shows a periodic wave-like oscillation with the expected periodicity of 3.6 amino acids of an α -helix (1,32,32). These dipolar waves profile and the PISA wheel can be used to interpret deviations from an ideal helix (such as kinks in the helix) as shown in Figure 1.10 (1). There are

applications of the PISA patterns to β -sheet structures but the resulting patterns are not easily recognizable (1).

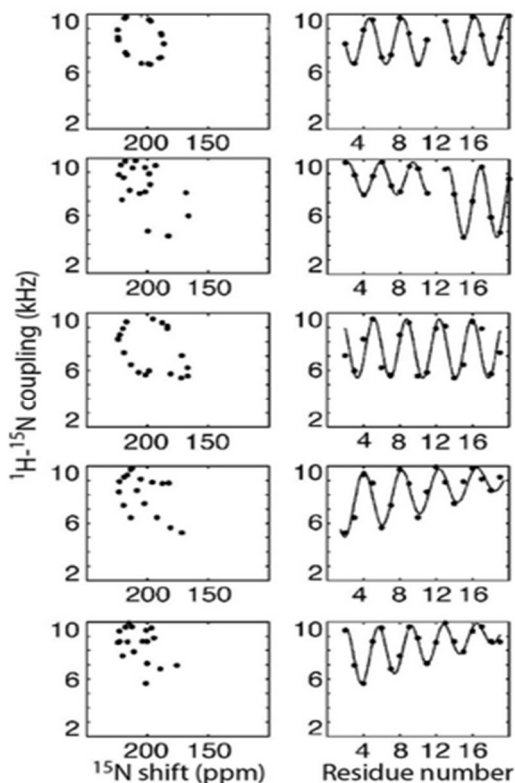


Figure 1.10. Simulated ^1H - ^{15}N SLF spectra (left panels) and plots of the ^1H - ^{15}N dipolar coupling (right panels) showing dipolar waves for α -helical structures with different kinks or curvature. (1)

Combining NN spin exchange experiment which generates crosspeaks in the 2D SLF spectrum between ^{15}N sites close in space with ^1H - ^{15}N SLF experiments allows for sequence assignment by walk down the protein backbone and connecting the generated crosspeaks. As seen in Fig. 1.11, this sequence assignment technique has been applied to Pfl coat protein reconstituted in DMPC/DHPC bicelles (21,23).

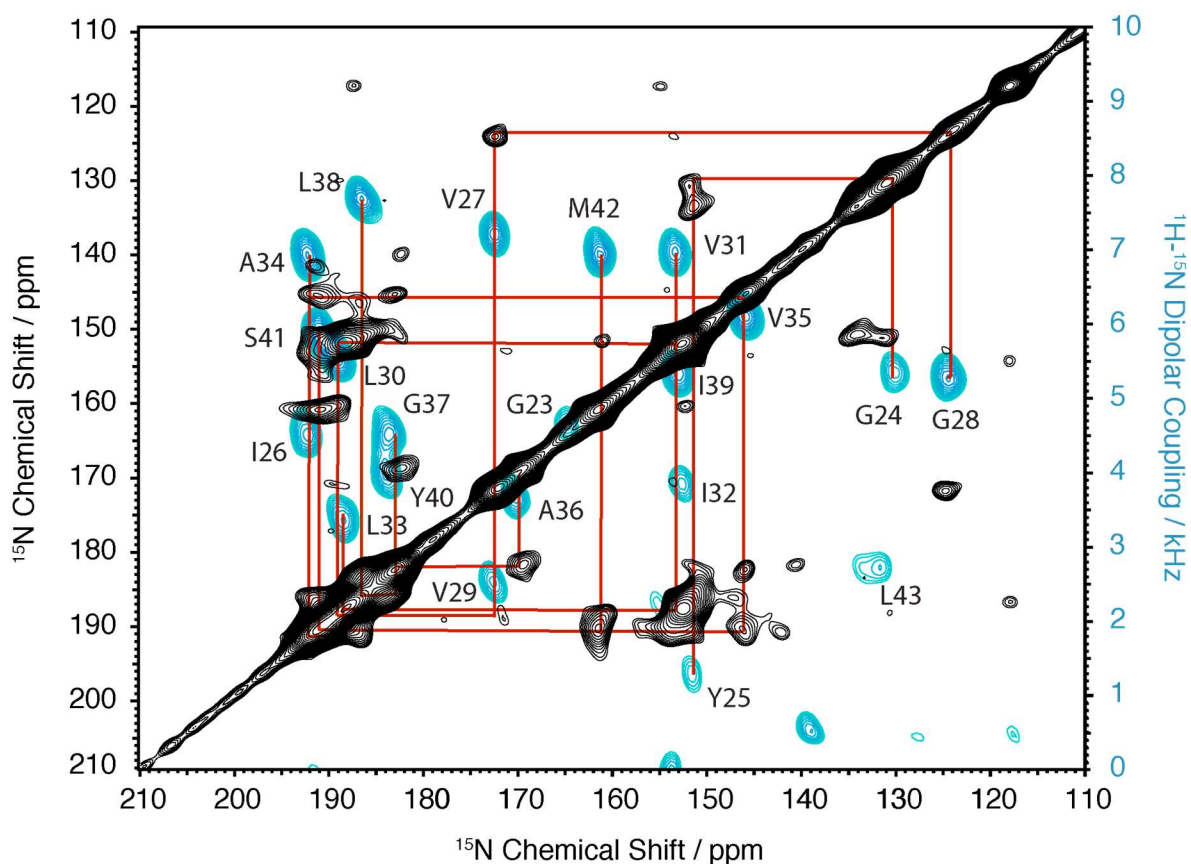


Figure 1.11. Confirmation of the previous spectroscopic assignment of the transmembrane helix of Pfl coat protein in parallel bicelles obtained by a superposition of PISEMA spectrum (blue contours and NN exchange spectrum Red lines show connectivities between the main peaks in the PISEMA spectra and cross peaks in the NN exchange spectrum passing via the main diagonal peaks.

Beyond the simplistic PISA wheels and dipolar waves, there is a need for calculating the overall fold of a membrane protein without knowing the secondary structure *a priori*. In order to obtain the membrane protein fold, the observed experimental frequencies are used to define the backbone ϕ / ψ torsional angles, which can then be used for membrane protein structure refinement (34). The aforementioned 2D SLF NMR experiments of aligned samples provide correlation of two frequencies, usually ^1H - ^{15}N dipolar couplings and ^{15}N chemical shifts.

However, the measurement of additional frequencies, particularly $^1\text{H}\alpha$ - $^{13}\text{C}\alpha$ dipolar couplings, is needed to improve resolution and reduce degeneracies of structural calculations (35,36).

1.4 Summary of present Research

The overall focus of this Dissertation is the development of new techniques to advance the application of OS-NMR for elucidating structure and dynamics of membrane proteins. The second Chapter focuses on the development of a new alignable membrane mimetic. A 15-mer peptoid polymer is used to stabilize DMPC lipids, forming a Peptoid-Macrodisc. In the third Chapter, the discussion will focus on measuring spin lattice relaxation time ($T_{1\rho}$) and probing protein rotational dynamics by using the anisotropic relaxation rates. Lastly, the development of a new triple resonance pulse sequence that detects $^1\text{H}\alpha$ - $^{13}\text{C}\alpha$ dipolar coupling at ^{15}N amide sites will be discussed in Chapter 4. The pulse sequence gives an important additional angular constraint for *de novo* elucidation of membrane protein backbone folds.

REFERENCES

1. Hansen, S. K., Bertelsen, K., Paaske, B., Nielsen, N. C., & Vosegaard, T. (2015). Solid-state NMR methods for oriented membrane proteins. *Progress in Nuclear Magnetic Resonance Spectroscopy*, *88*, 48-85.
2. Wallin, E., & Heijne, G. V. (1998). Genome-wide analysis of integral membrane proteins from eubacterial, archaean, and eukaryotic organisms. *Protein Science*, *7*(4), 1029-1038.
3. Russell, R. B., & Eggleston, D. S. (2000). New roles for structure in biology and drug discovery. *Nature Structural & Molecular Biology*, *7*, 928-930.
4. White, S. H., & Wimley, W. C. (1999). Membrane protein folding and stability: physical principles. *Annual Review of Biophysics and Biomolecular Structure*, *28*(1), 319-365.
5. Radoicic, J., Lu, G.J. & Opella, S.J. (2014). NMR structures of membrane proteins in phospholipid bilayers. *Quarterly Reviews of Biophysics*, (*47*), 249-283.
6. Hong, M., Zhang, Y., & Hu, F. (2012). Membrane protein structure and dynamics from NMR spectroscopy. *Annual Review of Physical Chemistry*, *63*, 1-24.
7. Liang, B., & Tamm, L. (2016). NMR as a tool to investigate the structure, dynamics, and function of membrane proteins. *Nature Structural & Molecular Biology*, *23*(6), 468-474.
8. Faham, S., & Bowie, J. U. (2002). Bicelle crystallization: a new method for crystallizing membrane proteins yields a monomeric bacteriorhodopsin structure. *Journal of Molecular Biology*, *316*(1), 1-6.
9. Warschawski, D. E., Arnold, A. A., Beaugrand, M., Gravel, A., Chartrand, E., & Marcotte, I. (2011). Choosing membrane mimetics for NMR structural studies of transmembrane proteins. *Biochimica et Biophysica Acta*, *1808*(8), 1957-1974.
10. Zhou, H. X., & Cross, T. A. (2013). Influences of Membrane Mimetic Environments on Membrane Protein Structures. *Annual Review of Biophysics*, *42*, 361-392.
11. Chou, J. J., Kaufman, J. D., Stahl, S. J., Wingfield, P. T., & Bax, A. (2002). Micelle-induced curvature in a water-insoluble HIV-1 Env peptide revealed by NMR dipolar coupling measurement in stretched polyacrylamide gel. *Journal of the American Chemical Society*, *124*(11), 2450-2451.
12. Marcotte, I., & Auger, M. (2005). Bicelles as model membranes for solid- and solution-state NMR studies of membrane peptides and proteins. *Concepts in Magnetic Resonance Part A*, *24A*, 17-37.
13. Opella, S. J. (2013). Structure determination of membrane protein Nuclear Magnetic Resonance spectroscopy. *Annual Review of Analytical Chemistry*, *6*, 305-328.

14. Opella, S. J., Ma, C., & Marassi, F. M. (2001). Nuclear magnetic resonance of membrane-associated peptides and proteins. *Methods in Enzymology*, 339, 285-313.
15. Smirnov, A. I., & Poluektov, O. G. (2003). Substrate-supported lipid nanotube arrays. *Journal of the American Chemical Society*, 125(28), 8434-8435.
16. De Angelis, A. A., & Opella, S. J. (2007). Bicelle samples for solid-state NMR of membrane proteins. *Nature protocols*, 2(10), 2332-2338.
17. Park, S. H., Berkamp, S., Cook, G. A., Chan, M. K., Viadiu, H., & Opella, S. J. (2011). Nanodiscs versus Macrodiscs for NMR of Membrane Proteins. *Biochemistry*, 50(42), 8983-8985.
18. Pines, A., Gibby M. G., & Waugh, J. S. (1973). Proton-enhanced NMR of dilute spins in solids. *The Journal of Chemical Physics*, 59(2), 569-90.
19. Hartmann, S. R. & Hahn, E. L. (1962). Nuclear Double Resonance in The Rotating Frame. *Physical Review*, 128(5), 2042-2053.
20. Levitt, M. H., Suter, D., & Ernst, R. R. (1986). Spin dynamics and thermodynamics in solid-state NMR cross polarization. *The Journal of Chemical Physics*, 84, 4243-4255.
21. Tang, W., & Nevzorov, A. A. (2011). Repetitive cross-polarization contacts via equilibration-re-equilibration of the proton bath: Sensitivity enhancement for NMR of membrane proteins reconstituted in magnetically aligned bicelles. *Journal of Magnetic Resonance*, 212(1), 245-248.
22. Koroloff, S. N., & Nevzorov, A. A. (2015). Optimization of cross-polarization at low radiofrequency fields for sensitivity enhancement in solid-state NMR of membrane proteins reconstituted in magnetically aligned bicelles. *Journal of Magnetic Resonance*, 256, 14-22.
23. Koroloff, S. N., Tesch, D. M., Awosanya, E. O., & Nevzorov, A. A. (2017). Sensitivity enhancement for membrane proteins reconstituted in parallel and perpendicular oriented bicelles obtained by using repetitive cross-polarization and membrane-incorporated free radicals. *Journal of Biomolecular NMR*, 67(2), 135-144.
24. Hester, R. K., Ackerman, J. L., Neff, B. L., & Waugh, J. S. (1976). Separated Local Field Spectra in NMR: Determination of Structure of Solids. *Physical Review Letters*, 36(18), 1081-1083.
25. Wu, C. H., Ramamoorthy, A., & Opella, S. J. (1994). High-resolution heteronuclear dipolar solid-state NMR spectroscopy. *Journal of Magnetic Resonance, Series A*, 109(2), 270-272.

26. Bielecki, A. K. A. C., Kolbert, A. C., De Groot, H. J. M., Griffin, R. G., & Levitt, M. H. (1990). Frequency-Switched Lee-Goldburg Sequences in Solids. *Advances in Magnetic and Optical Resonance*, *14*, 111-124.
27. Kamihira, M., Vosegaard, T., Mason, A. J., Straus, S. K., Nielsen, N. C., & Watts, A. (2005). Structural and orientational constraints of bacteriorhodopsin in purple membranes determined by oriented-sample solid-state NMR spectroscopy. *Journal of Structural Biology*, *149*(1), 7-16.
28. Nevzorov, A. A., & Opella, S. J. (2007). Selective averaging for high-resolution solid-state NMR spectroscopy of aligned samples. *Journal of Magnetic Resonance*, *185*(1), 59-70.
29. Nevzorov, A. A. (2008). Mismatched Hartmann-Hahn conditions cause proton-mediated intermolecular magnetization transfer between dilute low-spin nuclei in NMR of static solids. *Journal of the American Chemical Society*, *130*(34), 11282-11283.
30. Tang, W., Knox, R. W., & Nevzorov, A. A. (2012). A spectroscopic assignment technique for membrane proteins reconstituted in magnetically aligned bicelles. *Journal of Biomolecular NMR*, *54*(3), 307-316.
31. Marassi, F. M., & Opella, S. J. (2000). A solid-state NMR index of helical membrane protein structure and topology. *Journal of Magnetic Resonance*, *144*(1), 150-155.
32. Wang, J., Denny, J., Tian, C., Kim, S., Mo, Y., Kovacs, F. & Quine, J. R. (2000). Imaging membrane protein helical wheels. *Journal of Magnetic Resonance*, *144*(1), 162-167.
33. Pochapsky, T. C., & Pochapsky, S. (2008). *NMR for physical and biological scientists*. Garland Science.
34. Lapin, J., & Nevzorov, A. A. (2019). Validation of protein backbone structures calculated from NMR angular restraints using Rosetta. *Journal of Biomolecular NMR*, *73*(5), 229-244.
35. Bertram, B., Asbury, F., Fabiola, F., Quine, J. R., Cross, T. A., & Chapman, M. S. (2003). Atomic refinement with correlated solid-state NMR restraints. *Journal of Magnetic Resonance*, *163*(2), 300-309.
36. Yin Y. Y. & Nevzorov, A. A. (2011). Structure Determination in “Shiftless” Solid State NMR of Oriented Protein Samples. *Journal of Magnetic Resonance*, *212*(1), 64-73.
37. Radoicic, J., Park, S. H., & Opella, S. J. (2018) Macrodisc Comprising SMALPs for Oriented Sample Solid-State NMR Spectroscopy of Membrane Proteins. *Biophysical Journal*, *115*(1), 22-25.

CHAPTER 2

Peptoid-Membrane mimetic For Oriented Sample NMR Studies

2.1. ABSTRACT

A peptoid oligomer is used to stabilize DMPC lipid for formation of magnetically alignable macrodisc. Peptoid-based macrodiscs provided a detergent free phospholipid bilayer environment for reconstitution of membrane protein. The discs were shown to have an increased bilayer alignment and a more planar membrane environment when compared with oriented bicelles. The Pfl coat protein was successfully reconstituted in a stable Peptoid macrodisc. The narrow linewidth observed from Pfl coat protein demonstrates the potential of peptoid-stabilized macrodiscs for structure determination by oriented sample solid-state NMR spectroscopy.

2.2. INTRODUCTION

Biological membrane is composed of a lipid bilayer and the membrane-embedded proteins and is essential for cellular viability and function. The numerous functions of the membrane proteins include transport of ions across the cell membrane, signal receptors, and these proteins constitute about 30% of encoded genes (1). Thus, membrane proteins are targets for structure determination using X-ray crystallography, Cryo-EM and solution and solid-state NMR spectroscopies (2-7). The limitations of lipid crystallization and long reorientation times on the solution NMR scale place oriented-sample solid state NMR (OS-NMR) in an ideal position to study membrane proteins under their native-like conditions (8). Structure determination of membrane proteins by OS-NMR or any other analytical technique depends on the environment of the sample under study. The factors affected by the environment include spectral and structural resolution of the protein sample under investigation, and whether the determined structure is a true representation of the native protein in its active conformation (2,9-10). Hence, developing a suitable membrane model that adequately mimics the biological membrane is key to successful structure determination. The membrane mimics that have been used for NMR structure determination include liposomes, micelles, bicelles, and lipid nanodiscs (11-12).

Liposomes are spherical lipid vesicles, either small unilamellar vesicles (SUV) with one lipid bilayer or multilamellar (MLV) with multiple lipid bilayers surrounding an aqueous core (11). Liposomes have been shown to be inadequate models for solution NMR studies due to long reorientation time on the NMR time scale, although spectral resolution is increased by the use of MAS-NMR (12). Micelles can be formed by dissolving hydrophobic lipids in aqueous solutions. Micelles are easy to prepare and rapidly reorient, which is needed for high-resolution solution

NMR studies. Micelles however are not an ideal membrane model because they have a monolayer structure with high curvature, a loose packing of the lipid head groups, and tighter chain entanglement in the center (2). Bicelles or 'binary bilayered mixed micelles' were introduced by Sanders et al (13) and are composed of long chain lipid 1,2-dimyristoyl-sn-glycero-3-phosphocholine (DMPC), which are capped by a short chain 1,2-dihexanoyl-sn-glycero-3-phosphocholine (DHPC). Bicelles orient spontaneously in magnetic fields (B_0) with the bilayer normal either perpendicular to the B_0 field direction or parallel, with the addition of some Lanthanides (44). The orientation occurs above the DMPC gel-to-fluid transition temperature which is typically between 30° and 50°C (2). Bicelles provide a planar stable bilayer of phospholipids and have local morphology similar to biomembranes (2). A variety of oriented bicelles have been useful as a membrane mimetic for structural determination by OS-NMR (14). However, the main limitation is that bicelle formation is restricted to specific types of membrane components and do not represent the diversity of composition in biological membranes (14). There is tremendous interest in developing membrane mimetics that can accommodate for a broad range of lipid constituents and environmental conditions. Nanodiscs are becoming widely utilized in the investigations of membrane protein and lipid-protein interactions. Nanodiscs are discoidal nanoparticles composed of lipid bilayer encircled by proteins, peptides, or polymers on the edge of the lipid acyl chain (15). Inspired by the human ApoA1 protein or the high-density lipoprotein, Sligar and co-workers expressed recombinant 'membrane scaffold proteins' that can self-assemble into discoidal phospholipid bilayer (15-16). While MSP-nanodiscs are excellent membrane mimics, there is still a requirement of using detergents for reconstitution of membrane proteins. The large size of the MSP-nanodisc also limited its use to solution NMR. One strategy to make the mimetic suitable for OS-NMR was to increase the size of the lipid particle and make

it alignable in the main magnetic field. The macrodisc is synthetic model membrane systems with diameter of ~ 30 nm (Figure 2.1), consist of long-chain phospholipid bilayer surrounded by an amphipathic 14-residue α -helical peptide 14-Mer (Ac-DYLKAFYDKLKEAF-NH₂) (17). By contrast, the smaller nanodisc (~ 10 nm) can be formed when the ratio of the phospholipids to the peptide is decreased.

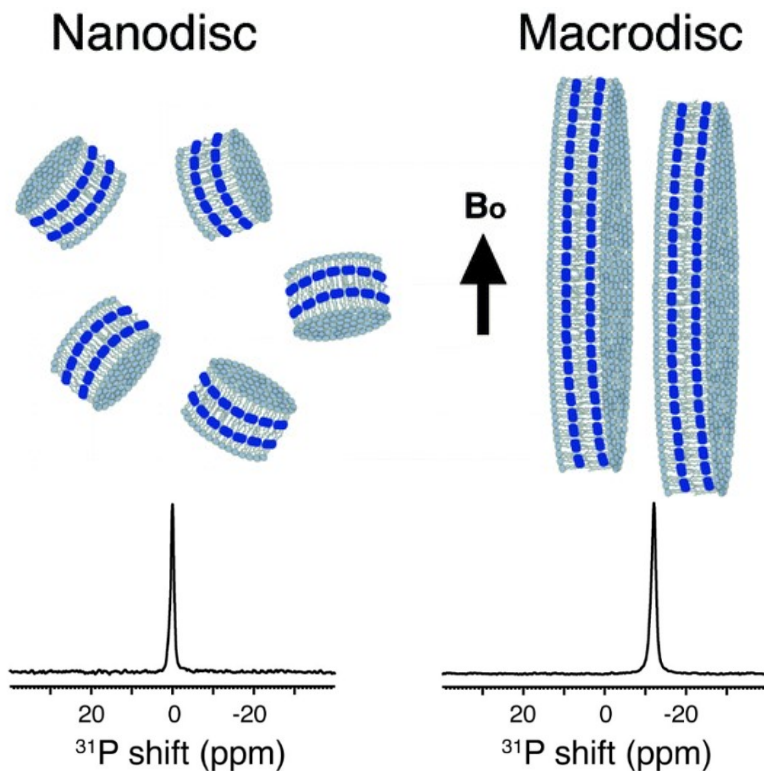


Figure 2.1. Nanodiscs vs Macrodiscs, along with their ³¹P alignments. Figure reproduced from ref. (17).

The size of the bilayer disc determines the behavior of the membrane model system. Membrane proteins reconstituted in the nanodiscs undergo isotropic reorientation and are commonly used in solution NMR. By contrast, proteins stabilized in macrodisc bilayers are magnetically alignable at temperatures above the gel-to-liquid crystalline transition temperature of the phospholipids.

Another promising approach to membrane mimetics is the use of styrene-maleic acid (SMA) copolymers to stabilize the lipid to make SMA-lipid particle (SMALP). The SMA copolymer is the hydrolyzed form of styrene and maleic anhydride copolymerization (18-21). It has been shown that SMA can directly extract membrane proteins and lipids from cell, making it a unique polymer for creating membrane models (18). The SMA copolymer like the 14-residue α -helical peptide is amphipathic and can produce magnetically alignable macrodiscs based on the lipid- to-polymer ratio. The recent experimental linewidth ~ 0.3 ppm for Pf1 membrane protein reconstituted in SMA-macrodisc demonstrates its promise as a mimetic for OS-NMR (19). SMA-macrodisc offers a monodisperse mimetic when used at a pH between 7 and 8 for optimal interactions with lipid membranes. However, there tends to be precipitation under low pH (<6). Functionalization of the SMA polymer and the development of similar polymers have led to greater pH stability (20-22). Here, we present the formation of macrodiscs constructed with DMPC lipids and a peptoid polymer. Using Pf1 coat protein, we demonstrate the utility of a peptoid macrodisc model for investigation of membrane protein with OS-NMR.

2.3. PEPTOID-MACRODISC

Peptoids are oligomers of *N*-substituted glycines that have side-chains appended to the nitrogen atoms rather than the alpha carbons. Therefore, there is a loss of main chain chirality

and removal of the backbone hydrogen-bond donor (NH) (23-25). Peptoid is a unique class of peptidomimetics that is dominated by side-chain chemistry and monomer sequence while maintaining the backbone amide of peptides. NMR and X-ray studies have demonstrated that peptoid oligomers form secondary helical conformations with the inclusion of alpha-chiral and aromatic side chain groups (26-31). The helical ordering investigated by molecular modeling and Circular Dichroism (CD) are proposed to be induced by steric clash avoidance and electrostatic repulsion between backbone carbonyls and pi clouds of side chains with aromatic rings (26,32-33). Peptoids can be easily synthesized to have diverse structures by using solid-phase submonomer synthesis method (23,34). Due to the similarities to polypeptides and the resistance to proteolytic degradation, peptoid polymer exhibits high biocompatibility. Peptoids effectiveness for biological activities has motivated development for several applications, including antimicrobial agents and vectors for gene and drug delivery (24,35). An important consideration for making peptoid-macrodisc is the peptoid lipid interaction. Similar to SMA, amphipathic peptoid polymer can also be inserted into the lipid membrane leading to the formation of peptoid-lipid fragments (36-37). This interaction with lipid membrane is driven by the peptoid's degree of hydrophobicity and dependent on the length of the amphipathic peptoid polymer (38-40). Recent work by Najafi et al, incorporated peptoids at the edge of bicelles and demonstrated that the peptoid functionalized bicelle did not significantly alter the bicelle morphology (41). Based on the insertion of amphipathic peptoid into lipid, we have designed a 15-mer peptoid oligomer similar to SMA (2:1) co-polymer. The 15-mer peptoid is synthesized with 2:1 phenyl:carboxyl monomer ratio. The designed peptoid shown in Figure 2.2 allows for incorporation into DMPC lipid for formation of alignable peptoid-DMPC macrodisc.

2.4. MATERIALS AND METHODS

Peptoid Synthesis

The peptoid was synthesized on a robotic synthesizer using the submonomer solid-phase method (34). The synthesis was started with the activation of the rink amide resin was activated with dimethylformamide (DMF). The first step of the submonomer cycle starts with acylation by addition of 0.6 M bromoacetic acid in DMF and 86 μ L of N, N'-diisopropylcarbodiimide (DIC). The acylation is followed by addition of 1.5M primary amine side chain DMF. The cycle was repeated until completion of the 15-mer Peptoid. The peptoid was cleaved from the resin and deprotected using a solution of 95% trifluoroacetic acid (TFA) and 5% water. The design and synthesis of peptoid was done in collaboration with Ms. Quibria Guthrie and the Proulx lab (Chemistry, NCSU).

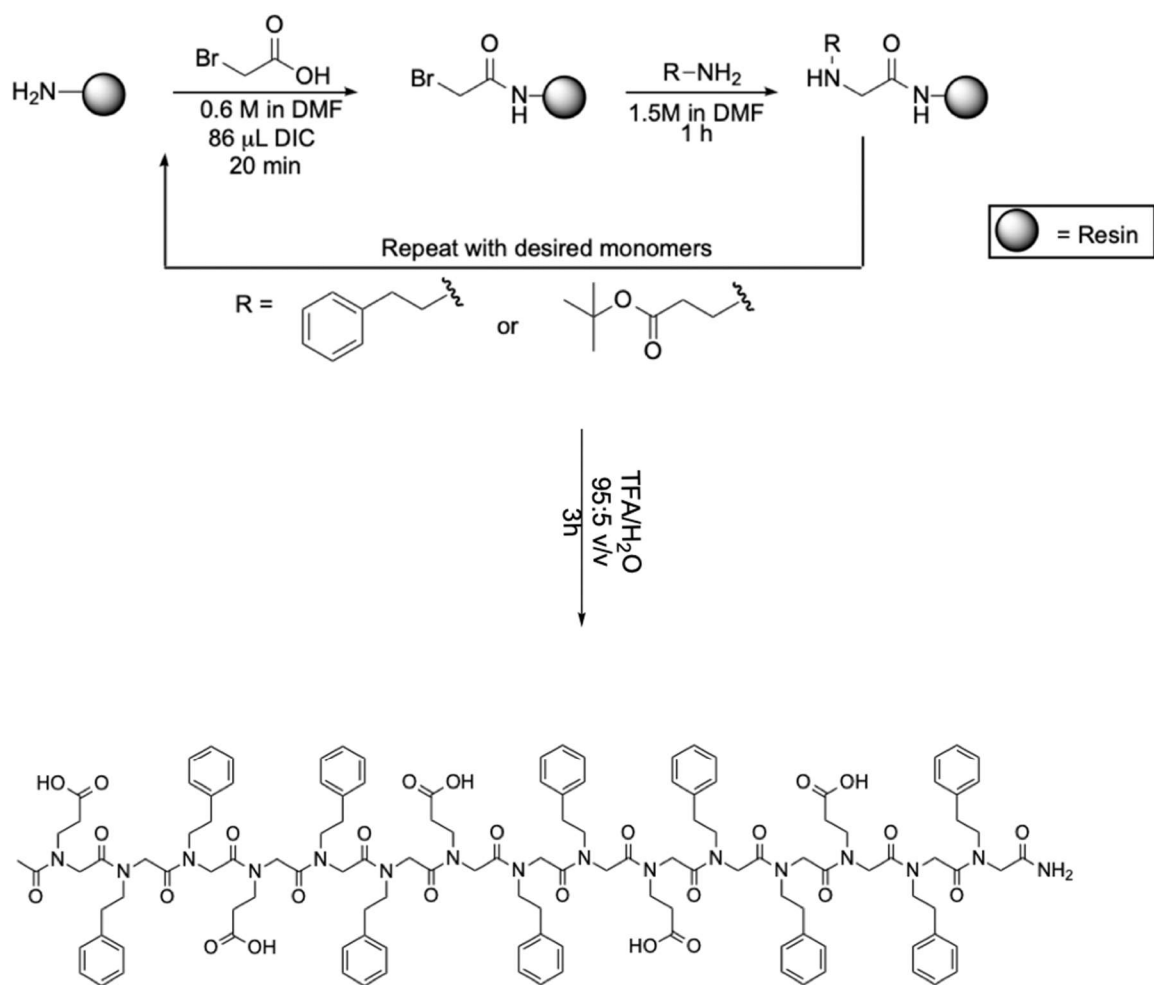


Figure 2.2. Schematic for synthesis of 15-mer peptoid, Chemical Formula $\text{C}_{127}\text{H}_{150}\text{N}_{16}\text{O}_{26}$, 2.3 kDa

Dynamic Light Scattering (DLS)

The peptoid-macrodisc DLS measurements were performed on a Zetasizer nano series (Malvern Instruments). The experiments were measured in a disposable 40 μl micro cuvette at 25 $^{\circ}\text{C}$ and at 40 $^{\circ}\text{C}$. All DLS measurements were collected for 30s using 10 scans.

NMR measurements

All NMR experiments were acquired on an Avance II spectrometer (Bruker) operating at ^1H NMR frequency of 500 MHz and data were acquired using the Topspin 2.0 software. ^{31}P NMR spectra were acquired using 20 μs 90-degree pulse with ^1H decoupling. The ^{15}N spectra was acquired using a 5 μs 90-degree pulse or 50 kHz B_1 field. The NMR samples were sealed in a 5 mm glass tube and placed in a static triple resonance $^1\text{H}/^{15}\text{N}/^{31}\text{P}$ Bruker 5 mm E-freeTM probe. The 2D experiment was acquired using the SAMPi4 sequence (42) with 1024 scans for each of the 80 t_1 points and NMR data were processed and analyzed with NMRPipe (43).

Sample Preparation

Lipids used were purchased from Avanti Polar Lipids. The Proulx Lab (NCSU) provided the Peptoid. Blank peptoid-DMPC macrodisc was prepared with a $\sim 1:22$ molar ratio and made with a 10% (w/v) lipid in a 200 μL sample (20 mM HEPES buffer, pH 8). Pfl in peptoid macrodisc were made by mixing $\sim 3\text{mg}$ of Pfl coat protein with DMPC lipid in chloroform and drying to a thin film under nitrogen gas. The protein/lipid was lyophilized overnight and rehydrated with the peptoid in 20 mM HEPES buffer. The blank and protein samples were subjected to several temperature cycles (ice/40 $^{\circ}\text{C}$).

2.5. RESULTS AND DISCUSSION

The size of the peptoid-DMPC disc determines its feasibility for OS-NMR application. Using DLS the size distribution of the peptoid macrodisc particle can be characterized as it diffuses in the sample solution. Shown in Table 1, the size (z-average or intensity averaged particle diameter) of the macrodisc particle measured at 25 °C is 26.90 and at 40 °C 28.68. The sample was measured at 25 °C and 40 °C to account for the viscosity difference in the gel-liquid transition. The z-average is extracted from the normalized time correlation of the scattered light intensity depending on the Brownian motion.

Table 2.1

DLS size distribution Report

Sample Temperature	25 °C	40 °C
Z-average	26.90	28.68
Polydispersity Index (PDI)	0.513	0.620

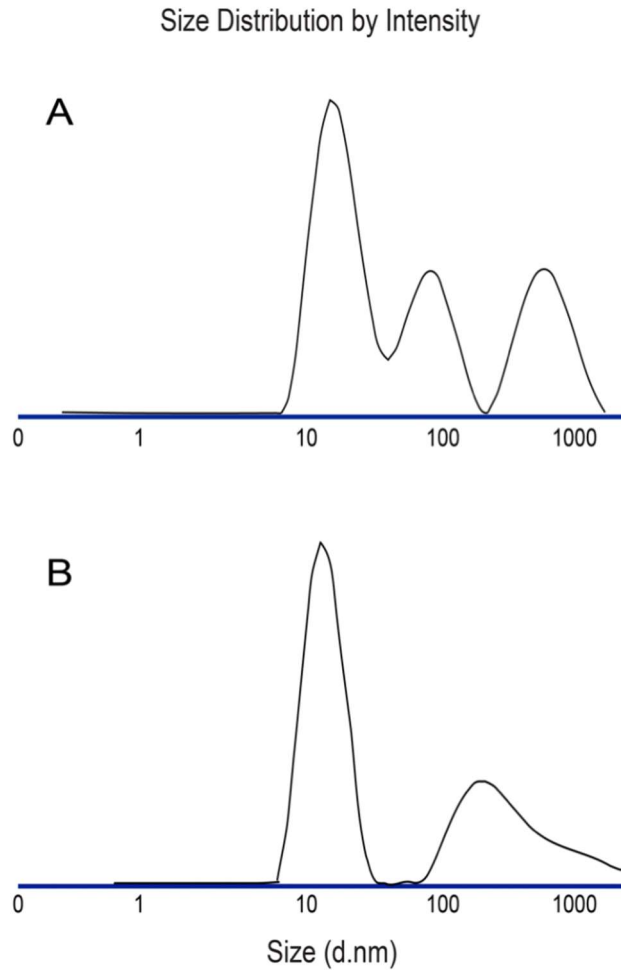


Figure 2.3. Dynamic light scattering (DLS) particle size distribution by intensity. A. Sample measured at 40° C. B. Sample measured at 25° C.

Assuming that the particle is spherical with a monomodal distribution the particles diameter can be computed from the translational diffusion coefficient D . For spherical particles, D is given by the Stokes-Einstein relation

$$D = \frac{k_B T}{3\pi \eta d_H}$$

Where $k_B T$ is thermal energy, η is the viscosity of the solvent and d_H is the particle's hydrodynamic diameter. The other parameter shown in Table 1 is polydispersity Index (PDI), this is a representation of the variance of size distribution. At 25 °C the PDI is 0.5 and 0.6 at 40 °C. The high polydispersity is indicated by the different peaks of size intensity distribution as shown in Figure 2.3. The larger size distributions are likely due to aggregation. The polydispersity of the sample complicates the size analysis. Therefore, the size and shape of peptoid-DMPC macrodisc requires further investigation.

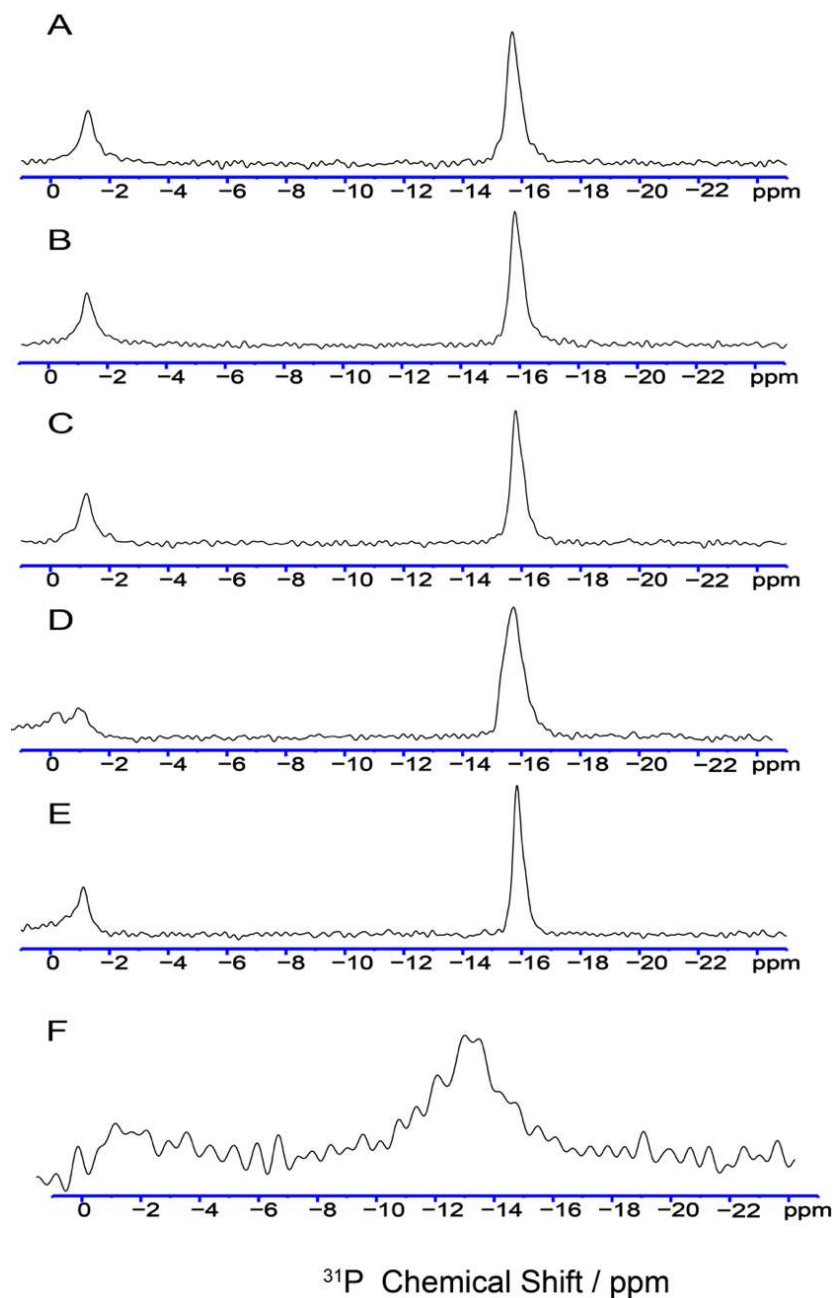


Figure 2.4. ^{31}P chemical shift NMR spectra of peptoid-Macrodisc's DMPC bilayer. Sample temperatures A-F (32 °C, 35 °C, 37 °C, 40 °C, 43 °C, 50 °C).

The alignment of the peptoid macrodiscs in the DMPC gel-to liquid crystalline phase transition temperature was investigated by ^{31}P NMR. The ^{31}P NMR spectra shown in Figure 2.4 A-F with chemical shift of -15.5 ± 1 ppm demonstrates that the DMPC bilayer is aligned with the normal

perpendicular to the direction of the applied magnetic field and provides a stable alignment over the gel-to-liquid crystalline phase temperature range. The average DMPC ^{31}P chemical shift linewidth at temperature 32-43 °C (Figure 2.4 A-F) was $\sim 80\text{Hz}(0.4\text{ppm})$, this is a narrower linewidth when compared with linewidth of 3.2 DMPC/DHPC bicelle. The chemical shift and narrow line width indicate a high degree of alignment and a higher order parameter when compared with the bicelle with its DMPC chemical shift $\sim 14\text{ ppm}$ (45-46).

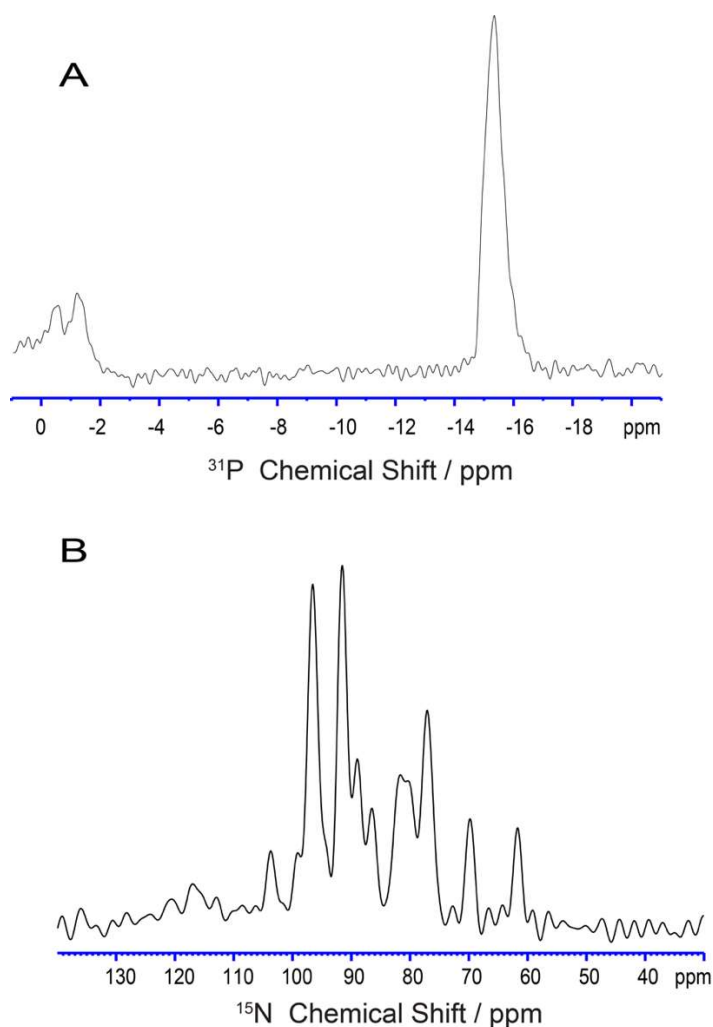


Figure 2.5. A. ^{31}P chemical shift NMR spectrum of Pf1 reconstituted in peptoid-macrodisc, sample temperature at 40 °C. B. ^{15}N chemical shift NMR spectrum of Pf1 coat protein reconstituted in peptoid-macrodisc at 40 °C.

The ^{31}P NMR spectrum of 3mg Pfl coat protein reconstituted in Peptoid macrodisc (Figure 2.5 A) also shows chemical shift at -15.5 ppm and 80 Hz linewidth. Figure 2.5B shows one-dimensional ^{15}N chemical shift spectrum of uniformly labelled Pfl coat protein in the Peptoid-macrodisc. The spectrum shows the resolved resonances from residues in the transmembrane helix (60 ppm-100 ppm). The 2D NMR data in Figure 2.6 shows a slight increase in order parameter when the range of dipolar coupling to that of DMPC/DHPC bicelles is compared ($S_0 = 0.83$ vs. 0.80). But a decreased order parameter is seen when compared with 14mer belt peptide macrodisc ($S_0 = 0.83$ vs. 0.85). Figure 2.7A shows two-dimensional (2D) SLF SAMPI4 spectrum of uniformly ^{15}N labeled Pfl in peptoid stabilized macrodisc, the spectrum shows ~ 280 Hz linewidth in the indirect dimension. The resolved resonance in the 2D NMR peptoid spectrum reflects fast uniaxial motional averaging. The 20 residues of the Pfl transmembrane helix are resolved and assigned in Figure 2.7A. The pattern of the assigned resonances indicates the classic PISA wheel seen in the transmembrane helix aligned $\sim 20^\circ$ to the direction of the magnetic field. The Dipolar wave shown in Figure 2.7B demonstrates the 3.6 residue periodicity of the Pfl coat protein transmembrane alpha helix.

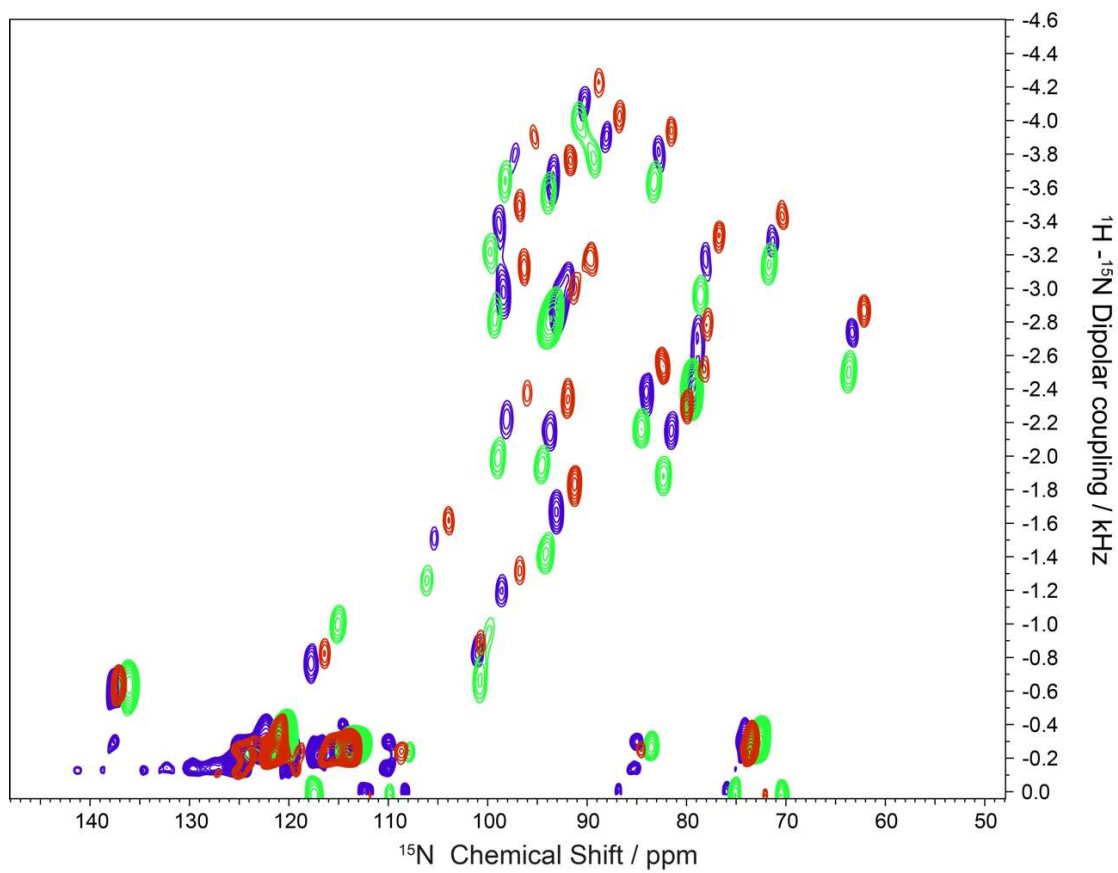


Figure 2.6. 2D NMR spectra of Pfl reconstituted in different membrane mimics; in green (3.2 DMPC/DHPC bicelles), in red (belt peptide-DMPC macrodisc), and in blue (15-mer peptoid-DMPC macrodisc).

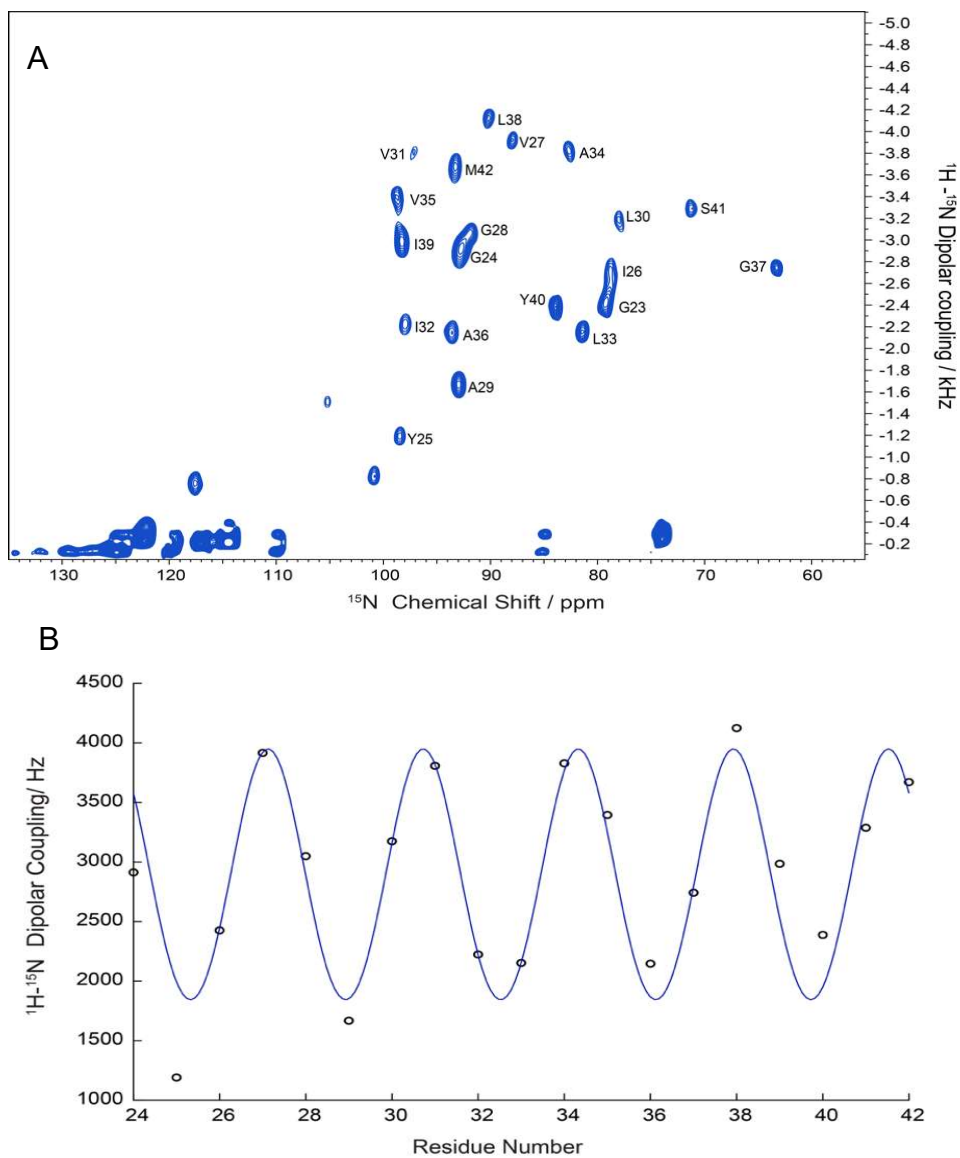


Figure 2.7. A. 2D NMR spectra of Pf1 coat protein in peptoid-DMPC macrodisc with 20 transmembrane residues assigned. B. Dipolar wave profile of Pf1 coat protein transmembrane domain with the expected periodicity of 3.6, which is indicative of the angular anisotropy of dipolar couplings for the alpha helix.

2.6. CONCLUSION AND PERSPECTIVES

Oriented sample solid state NMR is a tool for structural investigation of membrane proteins which requires a membrane mimic environment preserving their folding and functionality. Like bicelles and macrodisc stabilized with belt peptide or SMA polymer, Peptoid-macrodisc have been shown here to be a promising alternative membrane mimics for OS-NMR studies. The peptoid macrodisc is able to immobilize and align membrane proteins to obtain well resolved resonances as seen with imbedded Pfl coat protein. Both ^{31}P and ^{15}N NMR experiments show the peptoid-macrodisc with an increased alignment when compared to bicelles.

The formation of a stable membrane mimic with a 15-mer peptoid has been demonstrated in this chapter. However, the size and morphology of the peptoid-macrodisc needs further investigations. The DLS data show the peptoid-macrodisc with an approximated diameter of ~ 30 nm. However, due to the sample high polydispersity the true size of the mimic is yet to be determined. Hopefully, a longer peptoid oligomer might provide smaller and faster rotating disc that would allow for better resolution in the two-dimensional SAMPi4 spectra. Accordingly, this faster rotating disc would better suited for structural studies of larger membrane proteins which exhibit insufficient uniaxial rotational averaging by themselves.

REFERENCES

1. Wallin, E., & Heijne, G. V. (1998). Genome-wide analysis of integral membrane proteins from eubacterial, archaean, and eukaryotic organisms. *Protein Science*, 7(4), 1029-1038.
2. Marcotte, I., & Auger, M. (2005). Bicelles as model membranes for solid- and solution-state NMR studies of membrane peptides and proteins. *Concepts in Magnetic Resonance Part A*, 24A(1), 17-37.
3. Newby, Z. E. R., O'Connell, J. D., Gruswitz, F., Hays, F. A., Harries, W. E. C., Harwood, I. M., Ho, J. D., Lee, J. K., Savage, D. F., Miercke, L. J. W., & Stroud, R. M. (2009). A general protocol for the crystallization of membrane proteins for X-ray structural investigation. *Nature Protocols*, 4, 619-637.
4. Bartesaghi, A., & Subramaniam, S. (2009). Membrane protein structure determination using cryo-electron tomography and 3D image averaging. *Current Opinion in Structural Biology*, 19(4), 402-407.
5. Nietlispach, D., & Gautier, A. (2011). Solution NMR studies of polytopic α -helical membrane proteins. *Current Opinion in Structural Biology*, 21(4), 497-508.
6. Park, S. H., Das, B. B., Casagrande, F., Tian, Y., Nothnagel, H. J., Chu, M., Kiefer, H., Maier, K., De Angelis, A. A., Marassi, F. M., & Opella, S. J. (2012). Structure of the chemokine receptor CXCR1 in phospholipid bilayers. *Nature*, 491, 779-783.
7. Sharma, M., Yi, M., Dong, H., Qin, H., Peterson, E., Busath, D. D., Zhou, H. X., & Cross, T. A. (2010). Insight into the mechanism of the influenza A proton channel from a structure in a lipid bilayer. *Science*, 330(6003), 509-512.
8. Radoicic, J., Lu, G. J., & Opella, S. J. (2014). NMR structures of membrane proteins in phospholipid bilayers. *Quarterly Reviews of Biophysics*, 47(3), 249-283.
9. Page, R. C., Li, C., Hu, J., Gao, F. P., & Cross, T. A. (2007). Lipid bilayers: an essential environment for the understanding of membrane proteins. *Magnetic Resonance in Chemistry*, 45, S2-S11.
10. Zhou, H. X., & Cross, T. A. (2013). Modeling the membrane environment has implications for membrane protein structure and function: influenza A M2 protein. *Protein Science*, 22(4), 381-394.
11. Sebaaly, C., Greige-Gerges, H., & Charcosset, C. (2019). 'Lipid membrane models for biomembrane properties' investigation', In Basile, A. & Charcosset, C. (Ed.) *Current Trends and Future Developments on (Bio-) Membranes, Membrane Processes in the Pharmaceutical and Biotechnological Field*, Elsevier, 311-340.

12. Warschawski, D.E., Arnold, A.A., Beaugrand, M., Gravel, A., Chartrand, E., & Marcotte, I. (2011). Choosing membrane mimetics for NMR structural studies of transmembrane proteins. *Biochimica et Biophysica Acta*, *1808*(8), 1957–1974.
13. Sanders, C. R., & Schwonek, J. P. (1992). Characterization of magnetically orientable bilayers in mixtures of dihexanoylphosphatidylcholine and dimyristoylphosphatidylcholine by solid-state NMR. *Biochemistry*, *31*(37), 8898-8905.
14. Durr U. H. N., Gildenberg, M., & Ramamoorthy, A. (2012). The Magic of Bicelles Lights Up Membrane Protein Structure. *Chemical Reviews*, *112*(11), 6054-6074.
15. Denisov, I. G., & Sligar, S. G. (2017). Nanodiscs in membrane biochemistry and biophysics. *Chemical Reviews*, *117*(6), 4669-4713.
16. Bayburt, T. H., & Sligar, S. G. (2002). Single-molecule height measurements on microsomal cytochrome P450 in nanometer-scale phospholipid bilayer disks. *Proceedings of the National Academy of Sciences*, *99*(10), 6725-6730.
17. Park, S.H., Berkamp, S., Cook, G. A., Chan, M. K., Viadiu, H., & Opella, S. J. (2011). Nanodiscs versus Macrodiscs for NMR of Membrane Proteins *Biochemistry*, *50*(42), 8983-8985.
18. Dörr, J. M., Scheidelaar, S., Koorengel, M. C., Dominguez, J. J., Schäfer, M., van Walree, C. A., & Killian, J. A. (2016). The styrene–maleic acid copolymer: a versatile tool in membrane research. *European Biophysics Journal*, *45*, 3–21.
19. Radoicic, J., Park, S. H., & Opella, S. J. (2018). Macrodiscs Comprising SMALPs for Oriented Sample Solid-State NMR Spectroscopy of Membrane Proteins. *Biophysical Journal*, *115*(1), 22– 25.
20. Ravula, T., Ramadugu, S. K., Di Mauro, G., & Ramamoorthy, A. (2017). Bioinspired, size-tunable self-assembly of polymer-lipid bilayer nanodiscs *Angewandte Chemie International Edition*, *56*(38), 11466-11470.
21. Ravula, T., Hardin, N. Z., & Ramamoorthy, A. (2019). Polymer nanodiscs: Advantages and limitations. *Chemistry and Physics of Lipids*, *219*, 45– 49.
22. Ravula, T., Kim, J., Lee, D., & Ramamoorthy, A. (2020). Magnetic Alignment of Polymer Nanodiscs Probed by Solid-State NMR Spectroscopy *Langmuir*, *36*(5), 1258-1265.
23. Sun, J., & Zukermann, R. N. (2013). Peptoid Polymers: A highly designable bioinspired material. *ACS Nano*, *7*(6), 4715-4732.

24. Sun, J., & Li, Z. (2018). 'Peptoid applications in biomedicine and nanotechnology'. In Koutsopoulos, S. (Ed) *Peptide applications in biomedicine, biotechnology and bioengineering*. Woodhead Publishing, Sawston, 183–213.
25. Zuckermann, R. N., & Kodadek, T. (2009). Peptoids as potential therapeutics. *Current Opinion in Molecular Therapeutics*, 11(3), 299–307.
26. Wu, C. W., Kirshenbaum, K., Sanborn, T. J., Patch, J. A., Huang, K., Dill, K. A., Zuckermann, R. N., & Barron, A. E. (2003). Structure and Spectroscopic Studies of Peptoid Oligomers with α -Chiral Aliphatic Side Chains. *Journal of the American Chemical Society*, 125(44), 13525.
27. Wu, C.W., Sanborn, T. J., Huang, K., Zuckermann, R. N., & Barron, A. E. (2001). Peptoid oligomers with α -chiral, aromatic side chains: sequence requirements for the formation of stable peptoid helices. *Journal of the American Chemical Society*, 123(28), 6778-6784.
28. Wu, C.W., Sanborn, T. J., Zuckermann, R. N., & Barron, A. E. (2001). Peptoid oligomers with α -chiral, aromatic side chains: effects of chain length on secondary structure. *Journal of the American Chemical Society*, 123(13), 2958-2963.
29. Armand, P., Kirshenbaum, K., Goldsmith, R. A., Farr-Jones, S., Barron, A. E., Truong, K. T., Dill, K. A., Mierke, D. F., Cohen, F. E., Zuckermann, R. N., & Bradley, E. K. (1998). NMR determination of the major solution conformation of a peptoid pentamer with chiral side chains. *Proceedings of the National Academy of Sciences*, 95(8), 4309-4314.
30. Stringer, J. R., Crapster, J. A., Guzei, I. A., & Blackwell, H. E. (2011). Extraordinary robust polyproline type I peptoid helices generated via the incorporation of α -chiral aromatic N-1-Naphthylethyl side chains. *Journal of the American Chemical Society*, 133(39), 15559-15567.
31. Laursen, J. S., Harris, P., Fristrup, P., & Olsen, C. A. (2015). Triangular prism-shaped β -peptoid helices as unique biomimetic scaffolds. *Nature Communications*, 6, 7013.
32. Armand, P., Kirshenbaum, K., Falicov, A., Dunbrack, R. L., Dill, K. A., Zuckermann, R. N., & Cohen, F. E. (1997). Chiral N-substituted glycines can form stable helical conformations. *Folding and Design*, 2(6), 369-375.
33. Gorske, B. C., Stringer, J. R., Bastian, B. L., Fowler, S. A., & Blackwell, H. E. (2009). New strategies for the design of folded peptoids revealed by a survey of noncovalent interactions in model systems. *Journal of the American Chemical Society*, 131(45), 16555- 16567.

34. Zuckermann, R. N., Kerr, J. M., Kent, S. B. H., & Moos, W. H. (1992). Efficient method for the preparation of peptoids [oligo (N-substituted glycines)] by submonomer solid-phase synthesis. *Journal of the American Chemical Society*, 114(26), 10646–10647.
35. Fowler, S. A., & Blackwell, H. E. (2009). Structure–Function Relationships in Peptoids: Recent Advances toward Deciphering the Structural Requirements for Biological Function *Organic & Biomolecular Chemistry*, 7(8), 1508–1524.
36. Zhang, Y., Xuan, S., Owoseni, O., Omarova, M., Li, X., Saito, M. E., He, J., McPherson, G. L., Raghavan, S. R., Zhang, D., & John, V. T. (2017). Amphiphilic Polypeptoids Serve as the Connective Glue to Transform Liposomes into Multilamellar Structures with Closely Spaced Bilayers. *Langmuir*, 33(11), 2780–2789.
37. Zhang, Y., Heidari, Z, Su, Y. Yu, T., Xuan, S., Omarova, M., Aydin, Y., Dash, S., Zhang, D., Vijay, J. (2019). Amphiphilic Polypeptoids Rupture Vesicle Bilayers to Form Peptoid-Lipid Fragments Effective in Enhancing Hydrophobic Drug Delivery. *Langmuir*, 35(47), 15335-15343.
38. Jing, X., Kasimova, M. R., Simonsen, A. H., Jorgensen, L., Malmsten, M., Franzyk, H., Foged, C., & Nielsen, H. M. (2012). Interaction of peptidomimetics with bilayer membranes: biophysical characterization and cellular uptake. *Langmuir*, 28(11), 5167-5175.
39. Landry, M. R., Rangel, J. L., Dao, V. P., MacKenzie, M. A., Gutierrez, F. L., Dowell, K. M., Calkins, A. L., Fuller, A. A., & Stokes, G. Y. (2019). Length and Charge of Water-Soluble Peptoids Impact Binding to Phospholipid Membranes. *The Journal of Physical Chemistry B*, 123(27), 5822-5831.
40. Andreev, K., Martynowycz, M. W., Huang, M. L., Kuzmenko, I., Bu, W., Kirshenbaum, K., & Gidalevitz, D. (2018). Hydrophobic interactions modulate antimicrobial peptoid selectivity towards anionic lipid membranes. *Biochimica et Biophysica acta. Biomembranes*, 1860(6), 1414-1423.
41. Najafi, H., & Servoss, S. L. (2018). Altering the edge chemistry of bicelles with peptoids. *Chemistry and Physics of Lipids*, 217, 43– 50.
42. Nevzorov, A. A., & Opella, S. J. (2007). Selective averaging for high-resolution solid-state NMR spectroscopy of aligned samples. *Journal of Magnetic Resonance*, 185(1), 59-70.
43. Delaglio F., S. Grzesiek, G. W. Vuister, G. Zhu, J. Pfeifer, & A. Bax. (1995). NMRPipe: a multidimensional spectral processing system based on UNIX pipes. *Journal of Biomolecular NMR*, 6(3), 277-293.
44. De Angelis, A. A., & Opella, S. J. (2007). Bicelle samples for solid-state NMR of membrane proteins. *Nature Protocols*, 2(10), 2332-2338.

45. Triba, M. N., Warschawski, D. E., & Devaux, P. F. (2005). Reinvestigation by phosphorus NMR of lipid distribution in bicelles. *Biophysical Journal*, 88(3), 1887-1901.
46. Triba, M. N., Devaux, P. F., & Warschawski, D. E. (2006). Effects of lipid chain length and unsaturation on bicelle stability. A phosphorus NMR study. *Biophysical Journal*, 91(4), 1357–1367.

CHAPTER 3

Membrane Protein Rotational Dynamics Probed by Anisotropic NMR Relaxation

*This chapter is based on the publication “Protein Rotational Dynamics in Aligned Lipid Membranes Probed by Anisotropic $T_{1\rho}$ NMR Relaxation” by Emmanuel Awosanya, Alex Nevzorov, published in the Biophysical Journal (2018)

3.1. Abstract

Membrane-bound form of Pfl coat protein reconstituted in magnetically aligned DMPC/DHPC bicelles was used as a molecular probe to quantify for the viscosity of the lipid membrane interior via measuring the rotational diffusion coefficient of the protein. We have determined orientationally dependent ^{15}N solid-state NMR relaxation times in the rotating frame, or $T_{1\rho}$. This was accomplished by fitting individually the decay of resolved spectral peaks corresponding to the transmembrane helix of Pfl coat protein as a function of spin-lock time incorporated into the two-dimensional SAMPI4 pulse sequence. The $T_{1\rho}$ relaxation was modeled as uniaxial rotational diffusion on a cone, which yields a linear correlation with respect to the bond factor $\sin^4\theta_B$, where θ_B is the angle that NH bond forms with respect to the axis of rotation. Importantly, the bond factors can be independently measured from the dipolar couplings in the separated local-field SAMPI4 spectra. From this dependence, the value of the diffusion coefficient of $D_{\parallel} = 8.0 \times 10^5 \text{ s}^{-1}$ was inferred from the linear regression of the experimental $T_{1\rho}$ data even without any spectroscopic assignment. Alternatively, a close value of $D_{\parallel} = 7.7 \times 10^5 \text{ s}^{-1}$ was obtained by fitting the $T_{1\rho}$ relaxation data of assigned peaks for the transmembrane helical domain of Pfl to a wave-like pattern as a function of residue number. The obtained diffusion coefficients are remarkably close to the simple estimate obtained from the Stokes-Einstein equation if the protein is modeled as a cylinder with the radius of gyration of 10 Å with the local

bilayer viscosity of about 1 Poise, i.e. similar to the classical value reported by Saffman and Delbruck decades ago. The method illustrates the use of single-helix transmembrane peptides as molecular probes to assess the dynamic parameters of lipid bilayers by NMR relaxation in oriented lipid bilayers.

3.2. Introduction

Membrane proteins (MPs) perform a plethora of biological functions, including ion transport, signal transduction, and energy conversion in the living cells. The bilayer milieu, where membrane proteins reside in, profoundly modulates their structure and dynamics. It is well established that membrane proteins undergo relatively fast (on the microsecond time scale) rotational diffusion about the membrane normal (1-9). However, there is currently a controversy regarding the exact values of the local bilayer viscosity surrounding membrane proteins. The classical Saffman-Delbruck work predicts the viscosity values of about $\eta=1$ Poise, (or about 100 times that of pure water), for which the rotational diffusion coefficient can be estimated from the Stokes-Einstein relation as: $D_{\parallel} = k_B T / 4\pi\eta R^2 h = 8.5 \times 10^5 \text{ s}^{-1}$ (for a small single-helical protein having the radius of gyration of about $R=10 \text{ \AA}$ and height $h=40 \text{ \AA}$). By contrast, recent FT-IR studies (9) have reported much faster values of the rotational diffusion coefficient for GPCR's of about $5 \times 10^6 \text{ s}^{-1}$, or nearly an order of magnitude difference despite their larger size. Therefore, it would appear that the rotational diffusion coefficient and the local bilayer viscosity would greatly depend on the protein structure itself and the interactions of the protein side chains with the lipid hydrocarbon interior and head groups. An accurate quantification of these important biophysical parameters, therefore, requires a robust experimental method that would be suitable

for the determination of these values in each particular case (i.e. a particular membrane protein and type of lipid under study).

Solid-state Nuclear Magnetic Resonance, (NMR) is a widely used technique, which allows one to obtain structural and dynamic information of membrane proteins at atomic-resolution level. Magnetically aligned lipid bilayers or bicelles (10-14) represent an attractive native-like membrane mimetic for the structure-function studies of membrane proteins embedded in planar, lipid-rich environment by solid-state NMR. The natural magnetic alignment state for bicelles is that their membrane normal is perpendicular to the main magnetic field owing to the negative sign of the magnetic susceptibility anisotropy of the prevailing DMPC hydrocarbon interior (15). A parallel alignment of bicelles as in glass plates can also be achieved by either adding lanthanide ions (16-18) or by replacing DMPC lipids with the non-natural biphenyl lipids (19). The bicelles at higher $q=[\text{DMPC}]/[\text{DHPC}]$ ratios ($q>3$) could behave as perforated multilamellae (20, 21), thus precluding the rotation of the bicelle as a whole. The perpendicular bicelle orientation represents a hybrid situation between solution NMR and solid-state magic-angle spinning (MAS) NMR in the sense that the rotational diffusion of the protein molecules about the membrane normal is anisotropic while being stochastic in nature, thus providing the predominant line narrowing mechanism.

Perhaps the first example of such narrowing by “rotational alignment” for obtaining high-resolution 2D NMR spectra of uniformly labeled membrane proteins was demonstrated in magnetically aligned bicelles at the perpendicular orientation (22). Instead of cylindrical powder NMR patterns, that would have been expected in the purely static case, “rotationally aligned” highly resolved spectra are obtained for smaller proteins undergoing fast uniaxial diffusion within the liquid-like bilayer interior with the diffusion coefficient being on the order of $D_{\parallel} \sim$

10^5 - 10^6 s⁻¹ and possibly even faster (9). These diffusional rates are sufficient to average out the dipolar and chemical shift azimuthal anisotropies that are on the order of several kHz. Recently, the idea of “rotational alignment” has been employed under the magic-angle spinning conditions (23, 24) to extract heteronuclear dipolar couplings under recoupling conditions for membrane protein structure determination.

As a rule, the faster is the anisotropic uniaxial diffusion, the narrower NMR lines are obtainable at the perpendicular orientation. Yet at the same time, the *longitudinal* chemical shift anisotropy (CSA) and dipolar couplings are preserved by the macroscopic orientation of the sample. The latter is highly beneficial in terms of both improving spectral resolution (by increasing the measurable spectroscopic range) and obtaining structural information from the orientationally dependent chemical shifts and dipolar couplings. In this paper, we demonstrate how the longitudinal anisotropy of NMR relaxation can be used to extract quantitative information regarding the protein rotational dynamics in aligned bilayers.

3.3. The diffusion-on-a-cone model for $T_{1\rho}$ relaxation.

A simple quantitative model has been previously created (25) which allows one to estimate inhomogeneous (i.e. angular-dependent) contribution to NMR relaxation as a function of the uniaxial rotational diffusion coefficient under static (25) and spinning conditions (26). Briefly, it is based on the numerical and analytical solutions for NMR spectra of uniaxially diffusing proteins under the conditions of ¹H decoupling. The diffusion-on-a-cone model (27) simulates not only the positions of the NMR peaks but also, more importantly, their inhomogeneous lineshapes reflecting microscopic molecular order, macroscopic disorder, and uniaxial molecular rotation. As an illustration of the model, Figure 3.1 shows ¹⁵N CSA

linewidths simulated for the individual backbone ^{15}N sites with an ideal alpha-helix tilted at 20° with respect to the axis of rotation in perpendicular bilayers as a function of residue number at various values of the uniaxial rotational diffusion coefficient, D_{\parallel}

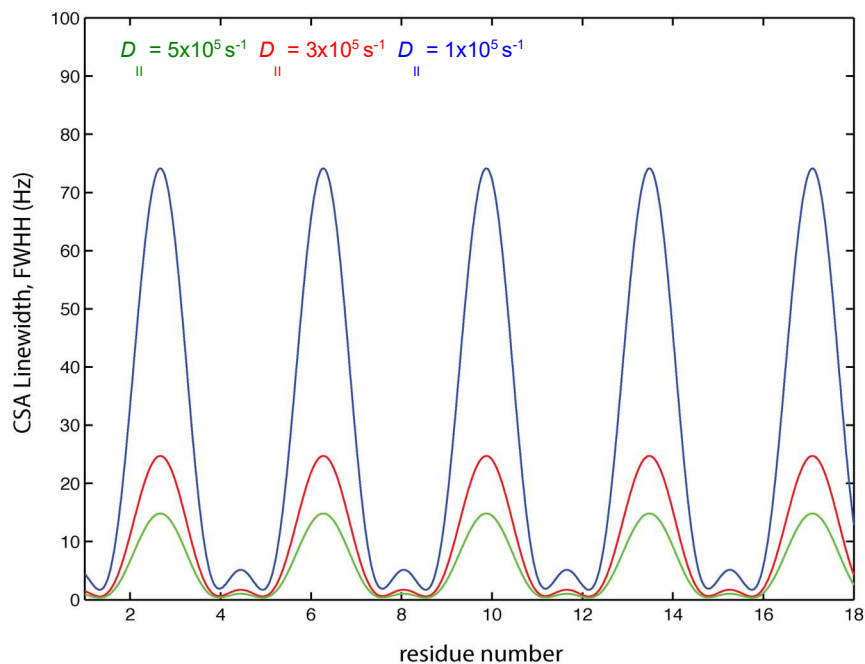


Figure 3.1. Inhomogeneous ^{15}N CSA linewidths in perpendicular bicelles calculated for an ideal alpha-helix tilted at 20° with respect to the axis of rotation at various values of the diffusion coefficient as indicated. At the value $D_{\parallel} = 5 \times 10^5 \text{ s}^{-1}$ theoretical rotational contribution to the ^{15}N CSA linewidths is less than 15 Hz (or about 0.3 ppm at ^1H 500 MHz NMR frequency). Slower rotational diffusion is manifested by larger anisotropy of linewidths at the perpendicular alignment of the bilayers.

It can be seen from Fig. 3.1 that at the rotational diffusion coefficient of $D_{\parallel} = 5 \times 10^5 \text{ s}^{-1}$, an appreciable motional narrowing is achieved yielding inhomogeneous contribution to linewidths of the maximum amplitude of 15 Hz. It should be noted that the inhomogeneity of the linewidths arises here due to the angular dependence of the CSA azimuthal anisotropies relative to the axis of rotation since the CSA tensor is tilted differently for each peptide plane orientation within the helix.

However, accurate experimental measurement and characterization of the diffusion rate D_{\parallel} solely from the CSA linewidths in the spectrum is challenging. In addition to requiring a high signal-to-noise ratio, this is due to the fact that there are many contributors to the CSA linewidths besides uniaxial rotational diffusion: contribution to relaxation from other motions (such as local and/or fast), magnetic field inhomogeneity, incomplete ^1H dipolar decoupling, etc. As a result, typical experimental linewidths observed in aligned membrane proteins are 1-2 ppm (or 50-100 Hz for ^{15}N nuclei at 500 MHz ^1H frequency, for example), which makes it difficult to accurately extract the anisotropic rotational contribution. Therefore, here we present a quantitative method for measuring uniaxial diffusion rates based on anisotropic relaxation in the rotating frame, or $T_{1\rho}$. As the T_2 relaxation rates, $T_{1\rho}$'s are expected to be inhomogeneous for each peak in the SLF spectrum (due to the angular dependence for the magnitudes of the local dipolar couplings) while being especially sensitive to the μs - ms motional time scales (28-30). Moreover, $T_{1\rho}$ relaxation mostly depends on the dipolar contribution, which is easier to model theoretically than the transverse relaxation arising from the many contributing factors mentioned above.

Let us consider an S spin (^{15}N or ^{13}C) coupled to its nearest neighbor I spin (^1H). Under the spin-locking conditions with radiofrequency ω_1 applied only on the S spin, the IS spin pair evolves under the Hamiltonian, which can be transformed to the singly tilted rotating frame as:

$$H = \omega_1 S_x + a(t) I_z S_z \xrightarrow{90_y} \omega_1 S_z - \frac{a(t)}{2} I_z (S_+ + S_-) \quad \text{Eq 2.1}$$

Here the function $a(t) = \chi[3\cos^2\beta(t) - 1]$ contains both the orientation- and time-dependent part of the heteronuclear dipolar coupling, which can be transformed as the spherical harmonics of rank 2:

$$3 \cos^2 \beta(t) - 1 = \sqrt{\frac{16\pi}{5}} Y_{2,0}(\beta(t), 0) = \sqrt{\frac{16\pi}{5}} \sum_{m=-2}^2 Y_{2,m}(\theta, 0) D_{m,0}^{(2)}(\varphi(t), \theta_B, 0) \quad \text{Eq 2.2}$$

Here the angle θ is the sample alignment angle, $\theta = \pi/2$ in the present case, $\varphi(t)$ is the time-dependent azimuthal rotation angle of the *IS* bond, θ_B is the angle that the bond forms with respect to the rotation axis, and the symbols $D_{m,0}^{(2)}$ designate the elements of the rank-2 Wigner rotation matrix. In order to treat the time-dependent effects due to the motions, the superoperator representation \mathbf{L} of the Hamiltonian H can be used, which is defined by: $\mathbf{L} \equiv H \otimes E - E \otimes H^T$, where E is the unity operator in the spin space. In this representation, the vectorized density matrix evolves under the action of the Liouvillian superoperator as given by the stochastic Liouville equation (31). The latter has been used extensively in EPR (32) but recently gained attention in NMR (26, 33, 34). The following general quadratic-form expression (35) has been used to solve for the decay of the ^{15}N magnetization in the rotating frame, $G(T)$ as a function of spin-lock time, T :

$$G(T) = \text{vec}^\dagger(S_x) \left\langle \exp_o \left\{ i \int_0^T \mathbf{L}(t) dt \right\} \right\rangle \text{vec}(S_x) \quad \text{Eq 2.3}$$

Here $\mathbf{L}(t)$ is the time-dependent Liouvillian superoperator, which includes radiofrequency irradiation and dipole-dipole terms as given by the Hamiltonian of Eq. (1), S_x is the spin momentum operator corresponding to ^{15}N spins, O stands for Dyson time-ordering, and the angular brackets indicate ensemble averaging over the rotational coordinates. The symbol “vec” denotes the vectorization operation for the matrix operator S_x (36), and “ \dagger ” stands for the Hermitian conjugate. In the tilted rotating frame Eq. (3) becomes:

$$G(T) = \text{vec}^\dagger(S_z) \left\langle \exp_o \left\{ -\frac{i}{2} \int_0^T a(t) [\mathbf{C}_{\pm z} e^{-i\omega t} + h.c.] dt \right\} \right\rangle \text{vec}(S_z) \quad \text{Eq 2.4}$$

here “*h.c.*” stands for the additional Hermitian-conjugate terms and the spin-space superoperator

$C_{\pm z}$ is defined by:

$$C_{\pm z} \equiv S_+ I_z \otimes E - E \otimes S_- I_z \quad \text{Eq 2.5}$$

In order to obtain the $T_{1\rho}$ dependence on the uniaxial diffusion on a tilted cone, similarly to T_2 (25), the formal time-dependent solution for the stochastic Liouville equation is expanded to the second-order cumulant (37) (denoted here by the triangular brackets with subscript “*c*”) in the limit of fast motions (which corresponds to the microsecond and faster time scale relative to the magnitude of dipolar couplings between the spins, ca. 10 kHz), viz.:

$$G(T) = \text{vec}^\dagger(S_z) \exp_0 \left\{ -\frac{1}{4} \int_0^T \int_0^t \left\langle a(t)a(t') [C_{\pm z} e^{-i\omega_1 t} + h.c.] [C_{\pm z} e^{-i\omega_1 t'} + h.c.] \right\rangle_c dt dt' \right\} \text{vec}(S_z) \quad \text{Eq 2.6}$$

It can be directly verified that the following properties hold:

$$\begin{aligned} C_{\pm z} C_{\pm z}^\dagger \text{vec}(S_z) &= C_{\pm z}^\dagger C_{\pm z} \text{vec}(S_z) = \frac{1}{2} \text{vec}(S_z) \\ C_{\pm z} C_{\pm z} \text{vec}(S_z) &= 0 \end{aligned} \quad \text{Eq 2.7}$$

These eigenvalue properties of the starting vector, $\text{vec}(S_z)$, allow one to easily factorize the final expression in the limit of fast motions as a simple single-exponential decay as:

$$G(T) = \exp \left\{ -\frac{T}{4} \int_0^\infty d\tau \left[\langle a(\tau)a(0) \rangle - \langle a(\tau) \rangle \langle a(0) \rangle \right] \cos(\omega_1 \tau) \right\} \quad \text{Eq 2.8}$$

Higher-order cumulants are expected to yield negligible contribution in the limit of fast motions by analogy with the Redfield limit in solution NMR (38). Contributions from higher-order non-secular terms in the dipolar Hamiltonian can also be neglected since in the high-field and microsecond motional regime the product of the nuclear Larmor frequencies Ω and the rotational correlation times τ is: $\Omega\tau \gg 1$. In passing, we should note that Equations 3-6 allow one to

formulate spin relaxation by means of a compact expression, making most of the assumptions (namely, (a-c), p. 276 in ref. (38)) of the solution-NMR Bloembergen-Purcell-Pound theory unnecessary, and, more importantly, is extendable to many-spin case.

For uniaxially rotating proteins, the correlation function can be modeled as diffusion on a cone having a 90° axis tilt (25), and is given by:

$$\langle a(\tau)a(0) \rangle - \langle a(\tau) \rangle \langle a(0) \rangle = \frac{9\chi^2}{8} \sin^4 \theta_B e^{-4D_1\tau} \quad \text{Eq 2.9}$$

If additional fast motions of the membrane director are involved, the correlation function should further be multiplied by the square of the order parameter S_0 (39). As a closed-form result, the dipolar contribution to the $T_{1\rho}$ relaxation in the case of uniaxial diffusion on a cone tilted by 90° with respect to the main magnetic field is given by:

$$\frac{1}{T_{1\rho}} \equiv R_{1\rho} = \frac{9S_0^2}{128D_{\parallel}[1 + (\omega_1 / 4D_{\parallel})^2]} \left(\frac{\mu_0\gamma_H\gamma_N\hbar}{4\pi r_{NH}^3} \right)^2 \sin^4 \theta_B \quad \text{Eq 2.10}$$

Where θ_B is the angle that an NH bond sweeps around the rotation axis (or the cone semiangle), S_0 is the bilayer order parameter, r_{NH} is the interspin distance between the ^{15}N and ^1H atoms, and γ_N , and γ_H are their respective gyromagnetic ratios. For an ideal alpha-helical TM domain having the periodicity 3.6, the cone semiangle θ_B for the n 'th NH bond of the helix can in turn be calculated using the following relation (40):

$$\cos \theta_B = \cos \theta_{ilt} \cos \delta - \sin \theta_{ilt} \sin \delta \cos\left(\frac{2\pi n}{3.6} + \varphi_0\right) \quad \text{Eq 2.11}$$

Here θ_{ilt} is the helix tilt, $\delta=15.8^\circ$ is the fixed angle that each NH bond forms with respect to the helix axis, and φ_0 is the rotation angle of the helix around its axis (or the “helix phase”).

Thus, the anisotropic $T_{1\rho}$ relaxation, similarly to the T_2 relaxation, can be used for the determination of diffusional rates. A principal distinction from the T_2 relaxation is that an

additional dependence on the spin-lock rf amplitude, ω_{rf} , enters the final expression for $T_{1\rho}$ in the form of a spectral density, $J(\omega_{rf})$ (41, 42). This additional term, however, becomes less important when the rotation is sufficiently fast, or $\omega_{rf} / D_{\parallel} \ll 1$. Note from Eq. (10) that the $\sin^4\theta_B$ angular anisotropy factor is independently obtainable in an SLF experiment from the directly measurable dipolar splittings, Δ (in Hz), by using simple trigonometry since the latter behave as $(3 \cos^2\theta_B - 1)$ scaled by the order parameter, S_o (~ 0.8). This fact not only greatly reduces the number of fitting parameters, but also allows one to fit the relaxation data directly without any spectroscopic assignment by using the following relation (when $\Delta > 0$ or $\theta_B < 54.7^\circ$):

$$\sin^4 \theta_B = \frac{4}{9} \left(1 - \frac{4\pi\Delta}{\chi S_o} \right)^2 \quad \text{Eq 2.12}$$

The case $\Delta < 0$ requires the overall tilt of the transmembrane helix be greater than 38.9° , and will not be considered here. An additional important advantage of using $T_{1\rho}$ relaxation times over T_2 is that the heteronuclear dipolar couplings are here the primary contribution and that they are independent of the B_0 field inhomogeneity and the many-spin ^1H - ^1H dipolar relaxation when relatively high rf spin-lock field are utilized. This allows for a more accurate assessment of the value for the rotational diffusion coefficient using small proteins (such as Pfl) as molecular probes in various membrane mimetics.

3.4. Materials and Methods

Sample Preparation

The Pfl coat protein reconstituted in DMPC/DHPC bicelle was expressed using Pfl bacteriophage purchased from Cedarlane (Burlington, NC) and *Pseudomonas aeruginosa* bacterial cell (ATCC, 25102) purchased from American Type Culture Collection (Manassas, VA). The Pfl phage was expressed following the previously described protocol (43). The Pfl

coat protein was purified using TFE (50%)/TFA (0.1%) for phage precipitation and lyophilized and followed by several washing steps for further purification. About 4 mg of the purified Pfl coat protein was reconstituted in a DMPC/DHPC bicelle, the lipids used were purchased from Avanti Polar Lipids (Alabaster, AL). The sample was reconstituted in a 200 μ l solution of 20 mM Hepes buffer at pH = 8.0 according to the protocol described in ref. (44). The bicelle sample had a lipid w/v ratio of 28%, a DMPC/DHPC molar ratio of $q=3.2$, and about a 4.1 mM concentration of Pfl coat protein.

NMR measurements and data analysis.

Experimentally the $T_{1\rho}$ measurements have been accomplished by inserting a spin-lock period before detection in a modified SAMPI4 sequence as shown in Fig 3.2. The cross-polarization transfer was enhanced by the REP-CP sequence (45). During the ^{15}N prelock time, the protons are decoupled to first order while contributing to the relaxation in the second order via heteronuclear dipolar couplings to the nitrogen spins. This sequence allows one to measure anisotropic $T_{1\rho}$'s separately for each peak and then fit the model simultaneously to the site-specific relaxation profiles using the dipolar couplings for each ^1H - ^{15}N spin pair which are directly measurable in the SAMPI4 experiment. Moreover, the wave-like behavior of periodicity 3.6 for the $R_{1\rho}$ relaxation rates for an alpha-helix allows one to fit the relaxation data for the assigned residues to a wave-like profile (cf. Eqs. 10-11) in order to extract the diffusion coefficients and the helix tilt relative to the axis of rotation (bilayer normal or director) similar to the T_2 profiles (25, 46). The data were acquired in a pseudo-3D fashion as a function of T , and the relaxation curves are subsequently fitted for each resolved peak. NMR data were processed

and analyzed using nmrPipe (47) and the parameter fitting was performed using scripts written in MATLAB (Mathworks, Inc).

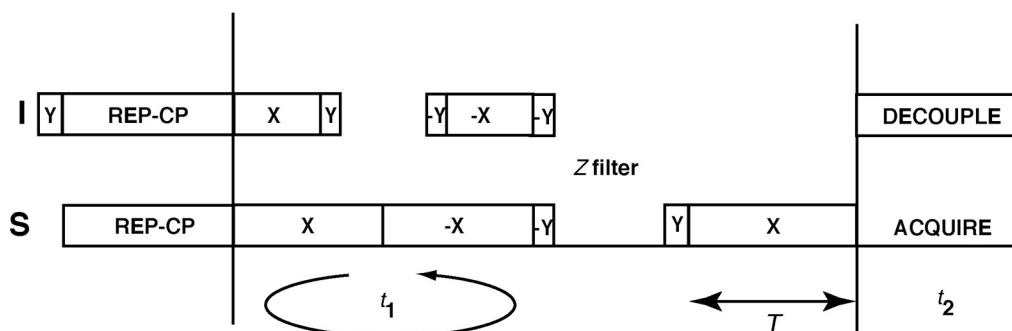


Figure 3.2. A modified SLF SAMPI4 pulse sequence incorporating a prelock of duration T for measuring individual $T_{1\rho}$ ' for the resolved peaks in the 2D SLF spectrum.

3.5. Results and Discussion.

Two-dimensional SLF SAMPI4 spectrum of the TM domain of Pfl (Figure 3.3A) serves as the basis for estimating the uniaxial diffusion coefficient by fitting the inhomogeneous $T_{1\rho}$ NMR relaxation profiles for each of the resolved 17 (seventeen) ^{15}N sites. Spin-lock periods of 0, 5ms, 10ms, 15ms, 20ms, and 25ms were inserted before detection in the SAMPI4 sequence. Figure 3.3B shows the ^{15}N relaxation profiles for the representative individual resonances normalized by their corresponding first-point intensity in the Pfl SAMPI4 spectra as a function of spin-lock periods. Note that the peak corresponding to the residue L38 (having the largest dipolar coupling, and thus, smallest factor $\sin^4\theta_B$) exhibits the slowest decay. The relaxation profiles were fitted to single exponential decays using a Matlab script (Mathworks Inc). The anisotropic $T_{1\rho}$'s ranging from 17 ms to 71 ms were determined according to the exponential function fit for each relaxation profiles, cf. Table 3.1. The relative errors for the peak intensities

ranging within 1.5%-3% were estimated from calculating signal to noise ratios using nmrPipe
(47)

Table 3.1

Anisotropic rotating-frame relaxation times and rates for Pfl coat protein residues (26-42)

Resi- due	I 26	V 27	G 28	A 29	L 30	V 31	I 32	L 33	A 34	V 35	A 36	G 37	L 38	I 39	Y 40	S 41	M 42
$T_{1\rho}$ (ms)	21 ± 2	40 ± 9	25 ± 2	17 ± 2	30 ± 2	42 ± 9	19 ± 2	22 ± 1	44 ± 1	35 ± 7	19 ± 3	26 ± 5	71 ± 1	29 ± 5	23 ± 2	44 ± 7	49 ± 11
$R_{1\rho}$ (s^{-1})	47 ± 4	25 ± 7	40 ± 4	57 ± 8	33 ± 2	24 ± 6	54 ± 7	46 ± 2	23 ± 7	29 ± 7	52 ± 8	39 ± 8	14 ± 5	34 ± 7	44 ± 5	23 ± 4	20 ± 6

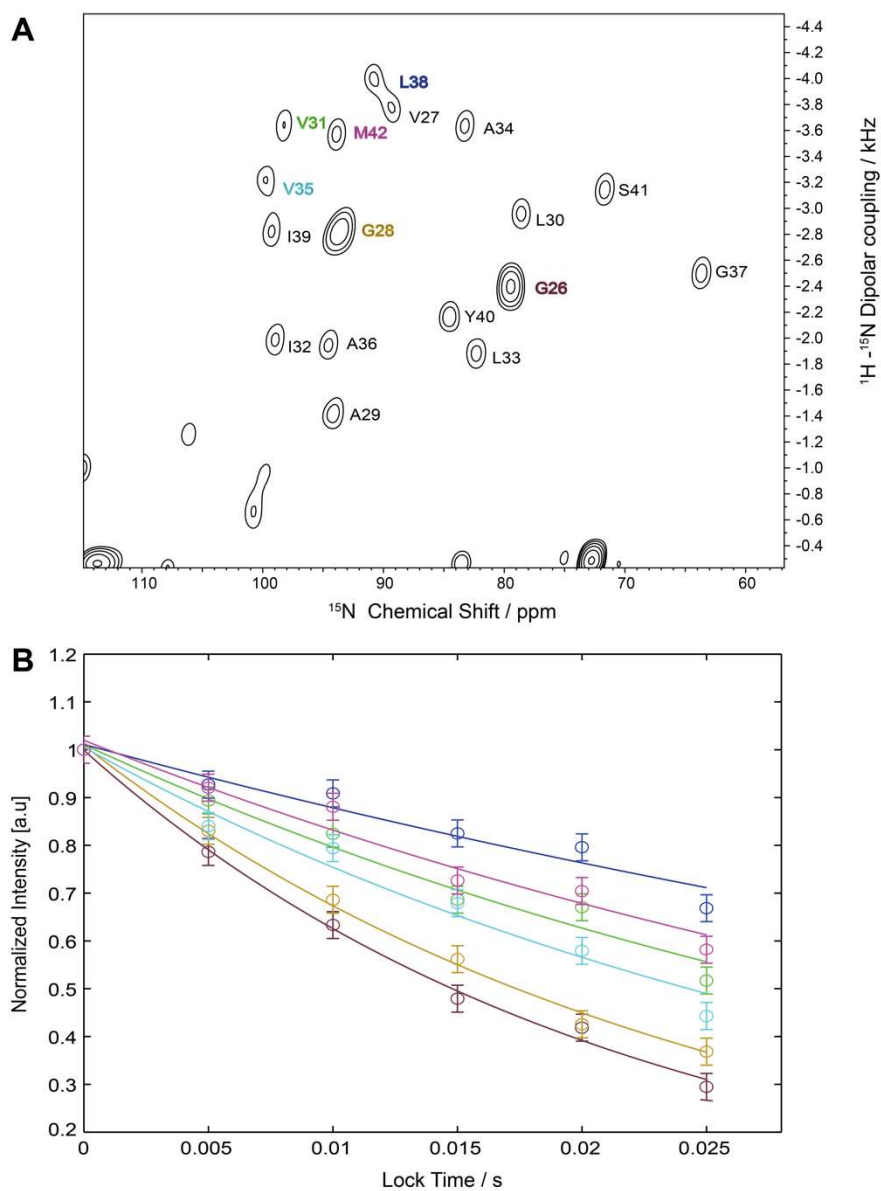


Figure 3.3. A. SAMPI4 spectrum of Pf1 coat protein obtained at 500 MHz ^1H frequency with assigned residue peaks for the transmembrane domain used for the fitting of anisotropic $T_{1\rho}$ relaxation times (assignment taken from ref. (48)). B. Six (6) representative ^{15}N relaxation profiles corresponding to the individual resonances L38, M42, V31, V35, G28, and I26 in the Pf1 SAMPI4 spectra (normalized by the first-point intensity) as a function of spin lock time fitted to single-exponential decays.

As seen from Eq. 10, anisotropic $T_{1\rho}$ relaxation times are expected to exhibit a simple linear dependence on the NH bond angular anisotropy factor, $\sin^4\theta_B$. The latter can be independently determined from the NH dipolar couplings in the SAMPI4 spectrum using Eq. 12. Figure 3.4 confirms the linear correlation of the relaxation rates $R_{1\rho} = T_{1\rho}^{-1}$ with respect to the bond factor $\sin^4\theta_B$. An offset parameter has added to account for the intrinsic (i.e. homogeneous contribution to $R_{1\rho}$). Based on this dependence, the uniaxial rotational diffusion coefficient value of $D_{\parallel} = 8.0 \times 10^5 \text{s}^{-1}$ was determined from the linear regression fit.

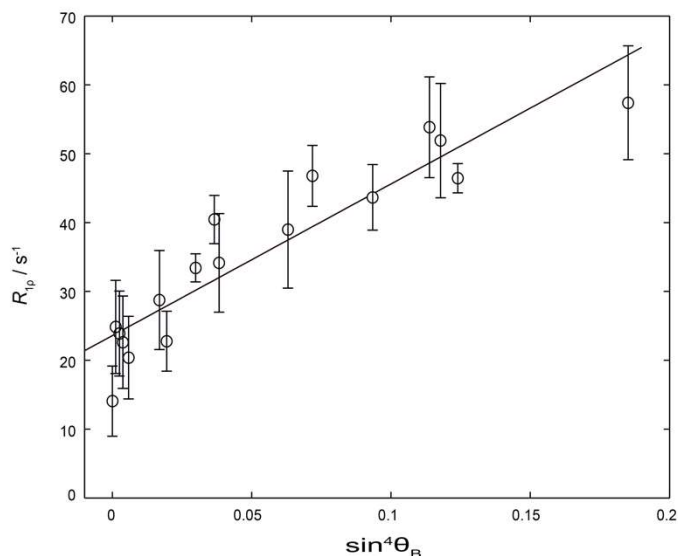


Figure 3.4. A correlation plot of $R_{1\rho}$ and bond factor $\sin^4(\theta_B)$, where θ_B is the angle that an NH bond makes with the axis of rotation. The rotational diffusion coefficient $D_{\parallel} = 8.0 \times 10^5 \text{s}^{-1}$ was deduced from linear regression using Eqs. 10 and 12 with the linear regression coefficient, $R^2=0.86$. Error bars correspond to a 95% confidence interval of relaxation rates determined by the exponential fits in the spin-locking experiments (Fig. 3.3B and Table 3.1).

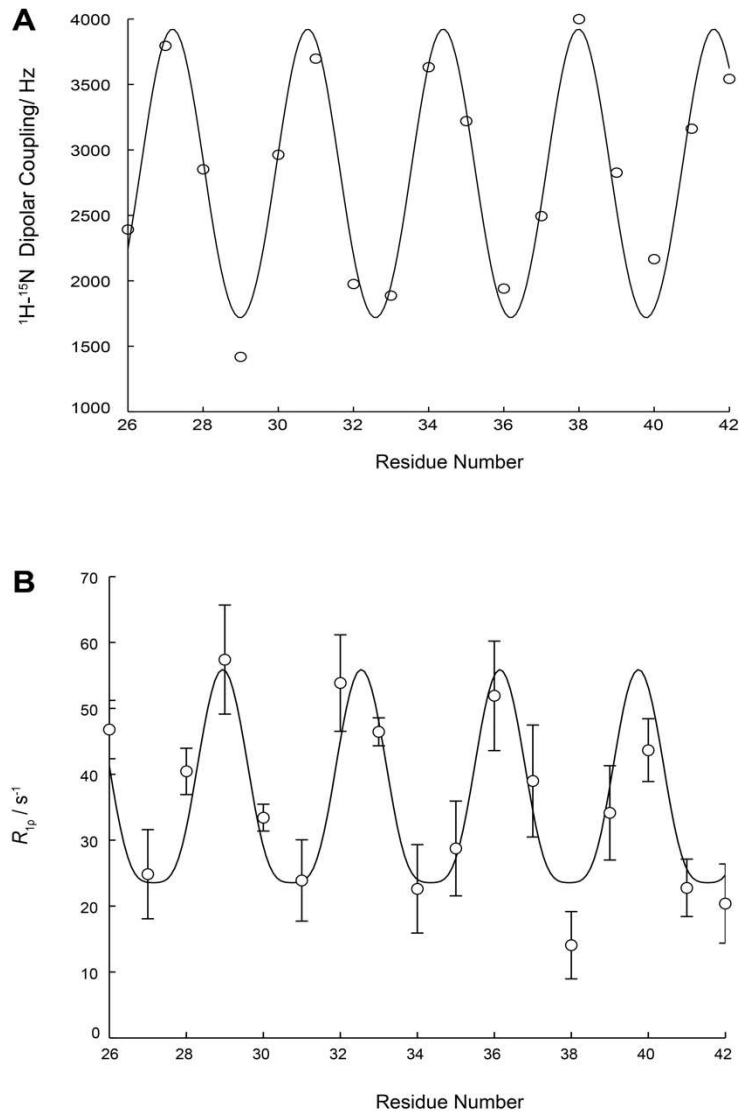


Figure 3.5. A. Dipolar waves of Pf1 coat protein transmembrane domain with the expected periodicity of 3.6, which is indicative of the angular anisotropy of dipolar couplings for the alpha helix. B. $R_{1\rho}$ relaxation profile for the assigned residue peaks for the TM region of Pf1. Wave-like behavior of the $R_{1\rho}$ relaxation rates allows one to extract the value of the diffusion coefficient of $7.7 \times 10^6 \text{ s}^{-1}$ when the helix tilt of 22.3° from part A is used in the fit. The error bars correspond to 95% confidence interval of relaxation rates determined by exponential fits from the spin-locking experiments (Fig. 3.3B and Table 3.I).

Figure 3.5A shows the “dipolar waves” of Pfl’s transmembrane alpha-helix (49), i.e. a plot of the dipolar couplings as a function of Pfl residue number. A helix tilt angle of 22.3° was obtained by fitting the experimentally measured dipolar coupling to a sinusoid function with a periodicity of 3.6 residues per turn (49), cf. also Eq. (11).

The uniaxial rotational diffusion coefficient can also be independently extracted from fitting the $R_{1\rho}$ relaxation rates for a series of consecutive assigned resonances in the Pfl transmembrane domain. Figure 3.5B shows the anisotropic $T_{1\rho}$ relaxation rates as a function of residue number. As can be seen, the anisotropic $T_{1\rho}$ relaxation for Pfl coat protein exhibits a wave-like pattern, similarly to the dipolar waves. A periodicity of 3.6 is also apparent, which is indicative of the alpha-helical angular anisotropy expected for the Pfl transmembrane domain. A diffusion coefficient value of $D_{\parallel} = 7.7 \times 10^5 \text{ s}^{-1}$ was obtained from fitting Eqs. (10-11) by restricting the helix tilt angle to $\theta_{\text{tilt}} = 22.3^\circ$, which is more accurately determined from the dipolar wave in Fig. 3.5A. The obtained diffusion coefficient is in a good agreement with the value of $D_{\parallel} = 8.0 \times 10^5 \text{ s}^{-1}$ independently obtained from the linear regression of relaxation rates vs. the bond factor, cf. Fig 3.4. Note that the $R_{1\rho}$ data have been fitted to the relaxation model with only 3 (three) free parameters - the diffusion coefficient D_{\parallel} , the homogeneous $R_{1\rho}$ offset parameter, and the helix phase. It should also be noted that fitting the data by unrestricting the range for θ_{tilt} has yielded two degenerate solutions with $D_{\parallel} = 1.2 \times 10^6 \text{ s}^{-1}$ $\theta_{\text{tilt}} = 27.8^\circ$, and $D_{\parallel} = 1.8 \times 10^6$ and $\theta_{\text{tilt}} = 33.8^\circ$. The parameters of the first solution are reasonably close to the diffusion coefficient from the fit of Fig. 3.4 and the helix tilt of Fig 3.5A. By contrast, the second solution is neither in accordance with the diffusion coefficient obtained from the bond factor correlation plot (cf. Fig. 3.4), nor with the helix tilt angle obtained from the dipolar wave (cf. Fig. 3.5A); therefore, it has been discarded. Such degenerate solutions are due to the fact that the amplitude

of the “ $R_{1\rho}$ wave” is simultaneously affected by both D_{\parallel} and θ_{tilt} (cf. Eqs. 10-11). The “consensus solution” between the fits of Figs. 3.4 and 3.5B (at the fixed helix tilt angle) yields the diffusional rate of ca. $D_{\parallel} = 8 \times 10^5 \text{ s}^{-1}$, which corresponds to the local bilayer viscosity value of 1 Poise assuming the radius of gyration of 10 Å for the Pfl coat protein when modeled as a rigid rotating cylinder. This value is consistent with the classical value of Saffman and Delbruck (2).

Table 3.2

Parameters obtained from diffusion on cone model determined by $T_{1\rho}$ relaxation

Parameter/ Model	Helix degree	Tilt, radians	Helix phase, radians	Diffusion coefficient, s^{-1}	$R_{1\rho}$ Offset, s^{-1}
Dipolar Wave	22.3°		-0.68	N/A	N/A
$R_{1\rho}$ Regression	N/A		N/A	8.0×10^5	23.6
$R_{1\rho}$ Wave	22.3° (fixed)		-0.60	7.7×10^5	23.5
$R_{1\rho}$ Wave	27.8°		-0.60	1.2×10^6	22.6
$R_{1\rho}$ Wave	33.8°		-0.60	1.8×10^6	21.1

3.6. Conclusions and Perspective

We have presented a quantitative method for characterizing the rotational diffusion coefficients of macroscopically aligned membrane proteins by solid-state NMR. Anisotropic rotating-frame ^{15}N NMR relaxation rates, or $R_{1\rho}$'s, provide a straightforward means for determining this important dynamic parameter. When the global rotation of the membrane is suppressed, as in perforated bicellar multilamellae, the value of the determined diffusion coefficient is directly related to the viscosity of the bilayer interior surrounding the protein. Using the membrane-bound form of Pfl coat protein as a molecular probe is advantageous in the sense that the rotational diffusion coefficient is directly relevant to its rotational dynamics as

compared to using spin labels (50) that themselves may undergo rotational isomerization, thus potentially interfering with data interpretation.

The developed model has allowed for a quantification of the diffusion coefficient of the Pfl coat protein yielding the value $D_{\parallel} = 8 \times 10^5 \text{ s}^{-1}$. Good quality of fits for the diffusion-on-a-cone model to the experimental data may also indicate that the backbone of the protein is fairly rigid and/or the local motions for the backbone atoms are highly restricted, thus making it possible to effectively model the overall rotation of the protein as a rigid body. The presented NMR method may also serve as a tool for differentiating the local bilayer viscosity surrounding the membrane-embedded proteins from the bulk bilayer viscosity by comparing the rotational diffusion coefficients and the derived viscosity values for smaller membrane-embedded rotating moieties (9, 50, 51) vs. membrane proteins and peptides reconstituted in oriented lipid media.

REFERENCES

1. Edidin, M. (1974). Rotational and translational diffusion in membranes. *Annual Review of Biophysics and Bioengineering*, 3, 179-201.
2. Saffman, P. G., & Delbruck, M. (1975). Brownian motion in biological membranes. *Proceedings of the National Academy of Sciences of the United States of America*, 72(8), 3111-3113.
3. Cherry, R. J., Muller, U., & Schneider, G. (1977). Rotational diffusion of bacteriorhodopsin in lipid-membranes. *Febs Letters*, 80(2), 465-469.
4. Lewis, B. A., Harbison, G. S., Herzfeld, J., & Griffin, R. G. (1985). NMR structural analysis of a membrane protein: bacteriorhodopsin peptide backbone orientation and motion. *Biochemistry*, 24(17), 4671-4679.
5. Valentine, K. G., Schneider, D. M., Leo, G. C., Colnago, L. A., & Opella, S. J. (1986). Structure and dynamics of fd-coat protein. *Biophysical Journal*, 49(1), 36-38.
6. Park, S. H., Mrse, A. A., Nevzorov, A. A., De Angelis, A. A., & Opella, S. J. (2006). Rotational diffusion of membrane proteins in aligned phospholipid bilayers by solid-state NMR spectroscopy. *Journal of Magnetic Resonance*, 178(1), 162-165.
7. Hong, M. & Doherty, T. (2006). Orientation determination of membrane-disruptive proteins using powder samples and rotational diffusion: A simple solid-state NMR approach. *Chemical Physical Letters*, 432(1-3), 296-300.
8. Cady, S. D., Goodman, C., Tatko, C. D., DeGrado, W. F., & Hong, M. (2007). Determining the orientation of uniaxially rotating membrane proteins using unoriented samples: A (2)H, (13)C, and (15)N solid-state NMR investigation of the dynamics and orientation of a transmembrane helical bundle. *Journal of the American Chemical Society*, 129(17), 5719-5729.
9. Spille, J. H., Zurn, A., Hoffmann, C., Lohse, M. J., & Harms, G. S. (2011). Rotational diffusion of the alpha(2a) adrenergic receptor revealed by FIAsH labeling in living cells. *Biophysical Journal*, 100(4), 1139-1148.
10. Sanders, C. R., & Prestegard, J. H. (1990). Magnetically orientable phospholipid bilayers containing small amounts of a bile salt analogue, CHAPSO. *Biophysical Journal*, 58(2), 447-460.
11. Sanders, C. R., & Schwonek, J. P. (1992). Characterization of magnetically orientable bilayers in mixtures of DHPC and DMPC by solid state NMR. *Biochemistry*, 31(37), 8898-8905.

12. Vold, R. R. & Prosser, R. S. (1996). Magnetically oriented phospholipid bilayered micelles for structural studies of polypeptides. Does the ideal bicelle exist? *Journal of Magnetic Resonance Series B*, 113(3), 267-271.
13. Glover, K. J., Whiles, J. A., Wu, G., Yu, N. J., Deems, R., Struppe, J. O., Stark, R. E., Komives, E. A., & Vold, R. R. (2001). Structural evaluation of phospholipid bicelles for solution-state studies of membrane-associated biomolecules. *Biophysical Journal*, 81(4), 2163-2171.
14. Durr, U. H. N., Gildenberg, M., & Ramamoorthy, A. (2012). The Magic of Bicelles Lights Up Membrane Protein Structure. *Chemical Reviews*, 112(11), 6054-6074.
15. Scholz, F., Boroske, E., & Helfrich, W. (1984). Magnetic anisotropy of lecithin membranes. A new anisotropy susceptometer. *Biophysical Journal*, 45(3), 589-592.
16. Prosser, R. S., Hwang, J. S., & Vold, R. R. (1998). Magnetically Aligned Phospholipid Bilayers with Positive Ordering: A New Model Membrane System. *Biophysical Journal*, 74(5), 2405-2418.
17. Verardi, R., Traaseth, N. J., Shi, L., Porcelli, F., Monfregola, L., De Luca, S., Amodeo, P., Veglia, G., & Scaloni, A. (2011). Probing membrane topology of the antimicrobial peptide distinctin by solid-state NMR spectroscopy in zwitterionic and charged lipid bilayers. *Biochimica Et Biophysica Acta-Biomembranes*, 1808(1), 34-40.
18. Gayen, A., Banigan, J. R., & Traaseth, N. J. (2013). Ligand-Induced Conformational Changes of the Multidrug Resistance Transporter EmrE Probed by Oriented Solid-State NMR Spectroscopy. *Angewandte Chemie (International Ed. in English)*, 52(39), 10321-10324.
19. Park, S. H., Loudet, C., Marassi, F. M., Dufourc, E. J., & Opella, S. J. (2008). Solid-state NMR spectroscopy of a membrane protein in biphenyl phospholipid bicelles with the bilayer normal parallel to the magnetic field. *Journal of Magnetic Resonance*, 193(1), 133-138.
20. Katsaras J., Harroun, T. A., Pencer, J., & Nieh, M. P. (2005). "Bicellar" lipid mixtures as used in biochemical and biophysical studies. *Die Naturwissenschaften*, 92(8), 355-366.
21. Soong, R., & Macdonald, P. M. (2009). Water Diffusion in Bicelles and the Mixed Bicelle Model. *Langmuir*, 25(1), 380-390.
22. De Angelis, A. A., Nevzorov, A. A., Park, S. H., Howell, S. C., Mrse, A. A., & Opella, S. J. (2004). High-resolution NMR spectroscopy of membrane proteins in "unflipped" bicelles. *Journal of the American Chemical Society*, 126(47), 15340-15341.

23. Das, B. B., Nothnagel, H. J., Lu, G. J., Son, W. S., Tian, Y., Marassi, F. M., & Opella, S. J. (2012). Structure Determination of a Membrane Protein in Proteoliposomes. *Journal of the American Chemical Society*, 134(4), 2047-2056.
24. Park, S. H., Das, B. B., Casagrande, F., Tian, Y., Nothnagel, H. J., Chu, M. N., Kiefer, H., Maier, K., De Angelis, A. A., Marassi, F. M., & Opella, S. J. (2012). Structure of the chemokine receptor CXCR1 in phospholipid bilayers. *Nature*, 491(7426), 779-783.
25. Nevzorov, A. A. (2011). Orientational and Motional Narrowing of Solid-State NMR Lineshapes of Uniaxially Aligned Membrane Proteins. *The Journal of Physical Chemistry B*, 115(51), 15406-15414.
26. Nevzorov, A. A. (2014). Coherent and stochastic averaging in solid-state NMR. *Journal of Magnetic Resonance*, 249, 9-15.
27. Lipari, G., & Szabo, A. (1981). Nuclear magnetic resonance relaxation in nucleic acid fragments: models for internal motion. *Biochemistry*, 20(21), 6250-6256.
28. Lewandowski, J. R., Sass, H. J., Grzesiek, S., Blackledge, M., & Emsley, L. (2011). Site-specific measurement of slow motions in proteins. *Journal of the American Chemical Society*, 133(42), 16762-16765.
29. Kurbanov, R., Zinkevich, T., & Krushelnitsky, A. (2011). The nuclear magnetic resonance relaxation data analysis in solids: general R1/R1(rho) equations and the model-free approach. *The Journal of Chemical Physics*, 135(18):184104.
30. Krushelnitsky, A., Zinkevich, T., Reif, B., & Saalwachter, K. (2014). Slow motions in microcrystalline proteins as observed by MAS-dependent ¹⁵N rotating-frame NMR relaxation. *Journal of Magnetic Resonance*, 248, 8-12.
31. Kubo, R. (1963). Stochastic Liouville Equations. *Journal of Mathematical Physics*, 4(2), 174-183.
32. Schneider, D. J., & Freed, J. H. (1989). Spin relaxation and motional dynamics. *Advances in Chemical Physics*, 73, 387-527.
33. Abergel, D., & Palmer, A. G. (2003). On the use of the stochastic Liouville equation in nuclear magnetic resonance: Application to R-1 rho relaxation in the presence of exchange. *Concepts in Magnetic Resonance Part A*, 19A(2), 134-148.
34. Edwards, L. J., Savostyanov, D. V., Nevzorov, A. A., Concistrè, M., Pileio, G., & Kuprov, I. (2013). Grid-free powder averages: On the applications of the Fokker–Planck equation to solid state NMR. *Journal of Magnetic Resonance*, 235:121-129.

35. Nevzorov, A. A., & Freed, J. H. (2000). Dipolar relaxation in a many-body system of spins of 1/2. *The Journal of Chemical Physics*, 112(3), 1425-1443.
36. Steeb, W. H. (1997). Matrix Calculus and Kronecker Product with Applications and C++ Programs. (World Scientific, Singapore) p 254.
37. Kubo, R. (1962). Generalized cumulant expansion method. *Journal of the Physical Society of Japan*, 17(7), 1100-1120.
38. Abragam, A. (1961). The Principles of Nuclear Magnetism (Oxford University Press, London) p 599.
39. Lipari, G., & Szabo, A. (1982). Model-Free Approach to the Interpretation of Nuclear Magnetic Resonance Relaxation in Macromolecules. I. Theory and Range of Validity. *Journal of the American Chemical Society*, 104, 4546-4559.
40. Ulrich, A. S., & Watts, A. (1993). 2H NMR lineshapes of immobilized uniaxially oriented membrane proteins. *Solid State Nuclear Magnetic Resonance*, 2(1-2), 21-36.
41. Look, D. C., & Lowe, I. J. (1966). Nuclear magnetic dipole-dipole relaxation along static and rotating magnetic fields - application to gypsum. *The Journal of Chemical Physics*, 44(8), 2995-3000.
42. Wolf, D. (1977). NMR determination of proton diffusion mechanisms in transition-metal hydrides. *Journal of Physics C-Solid State Physics*, 10(18), 3545-3557.
43. Thiriot, D. S., Nevzorov, A. A., Zagayanskiy, L., Wu, C. H., & Opella, S. J. (2004). Structure of the coat protein in Pfl bacteriophage determined by solid-state NMR spectroscopy. *Journal of Molecular Biology*, 341(3), 869-879.
44. De Angelis, A. A., & Opella, S. J. (2007). Bicelle samples for solid-state NMR of membrane proteins. *Nature Protocols*, 2(10), 2332-2338.
45. Tang, W. X., & Nevzorov, A. A. (2011). Repetitive cross-polarization contacts via equilibration-re-equilibration of the proton bath: Sensitivity enhancement for NMR of membrane proteins reconstituted in magnetically aligned bicelles. *Journal of Magnetic Resonance*, 212(1), 245-248.
46. Nevzorov, A. A. (2011). Ergodicity and efficiency in cross-polarization of NMR of static solids. *Journal of Magnetic Resonance*, 209(2), 161-166.
47. Delaglio, F., Grzesiek, S., Vuister, G. W., Zhu, G., Pfeifer, J., & Bax, A. (1995). NMRPipe: a multidimensional spectral processing system based on UNIX pipes. *Journal of Biomolecular NMR*, 6(3), 277-293.

48. Park, S. H., Marassi, F. M., Black, D., & Opella, S. J. (2010). Structure and Dynamics of the Membrane-Bound Form of Pfl Coat Protein: Implications of Structural Rearrangement for Virus Assembly. *Biophysical Journal*, 99(5), 1465-1474.
49. Mesleh, M. F., & Opella, S. J. (2003). Dipolar Waves as NMR maps of helices in proteins. *Journal of Magnetic Resonance*, 163(2), 288-299.
50. Nesmelov, Y. E., Karim, C. B., Song, L., Fajer, P. G., & Thomas, D. D. (2007). Rotational Dynamics of Phospholamban Determined by Multifrequency Electron Paramagnetic Resonance. *Biophysical Journal*, 93:2805-2812.
51. Nipper, M. E., Majd, S., Mayer, M., Lee, J. C. M., Theodorakis, E. A., & Haidekker, M. A. (2008). Characterization of changes in the viscosity of lipid membranes with the molecular rotor FCVJ. *Biochimica Et Biophysica Acta-Biomembranes*, 1778(4), 1148-1153.

CHAPTER 4

Chiral $^{13}\text{C}_\alpha$ - $^1\text{H}_\alpha$ Couplings Detection for Membrane Protein Structure Determination by Solid State NMR

*This chapter is based on the publication “NMR “Crystallography” for Uniformly (^{13}C , ^{15}N) Labeled Oriented Membrane Proteins” by Emmanuel Awosanya, Joel Lapin, and Alex Nevzorov. published in *Angewandte Chemie* (2019)

4.1 Abstract

Oriented-sample (OS) solid-state NMR has emerged as a powerful spectroscopic tool for determining structures of membrane proteins without the use of crystallization and cryogenic temperatures. In OS NMR, the orientationally dependent dipolar couplings and chemical shifts provide direct input for structure calculations. However, so far only the ^1H - ^{15}N dipolar couplings and ^{15}N chemical shifts have been routinely assessed in ^{15}N labeled protein samples. While efficient for determining tilt angles of short α -helical peptides, these two measurements alone are likely insufficient for determining protein structures of arbitrary topology. The main stumbling block for the determination of tertiary structures for membrane proteins by OS NMR has remained in the lack of additional experimental restraints. Here we have developed a new experimental triple-resonance NMR technique, which was applied to uniformly doubly (^{15}N , ^{13}C) labeled Pf1 coat protein reconstituted in magnetically aligned DMPC/DHPC bicelles. The previously inaccessible $^1\text{H}_\alpha$ - $^{13}\text{C}_\alpha$ dipolar couplings, which represent powerful chiral angular restraints, have been measured for the transmembrane domain of Pf1. Notably, the inclusion of the third restraint makes it possible to determine the torsion angles Φ and Ψ between the adjacent peptide planes without assuming an α -helical structure *a priori*. Using our recently developed structure calculation algorithm, fitting simultaneously three restraints per peptide plane have

resulted in families of structures which have subsequently been filtered using several Rosetta scoring functions determining the structure energetics within the membrane environment, hydrogen bonding, and Ramachandran preferences. This final filtering and validation step have led to a consensus α -helical transmembrane structure for Pfl coat protein, obtained in a *de novo* fashion. Our new approach greatly enhances utility of OS NMR as a structural tool for performing “NMR crystallography” in near-native membrane environments.

4.2 Introduction

Structure elucidation of membrane proteins (MPs) in planar, lipid-rich native-like bilayers remains a central topic in modern structural biology as the lipid environment itself may play a role in the modulation of the function and regulation of MPs. While being the undeniable leaders in structure determination of membrane proteins, both X-ray crystallography and cryo-EM employ cryogenic temperatures that may trap the proteins in biased structural conformations. These trapped conformations may be different from those encountered under the native conditions. Moreover, the fluid-like lipid bilayer environment has been shown to affect structure and function of membrane proteins (1-5). Solid-state NMR is a powerful spectroscopic tool that provides atomic resolution information about MPs under nearly physiological conditions (6-13). In particular, the method of oriented-sample (OS) solid-state NMR involves the measurements of the orientationally dependent dipolar couplings, which provide angular restraints for structure calculations. These restraints are highly complementary to the distance restraints obtainable in solid-state Magic Angle Spinning (MAS) NMR, where no preferred sample orientation is present and the angular information is, therefore, inaccessible. So far, only the ^1H - ^{15}N dipolar couplings and ^{15}N chemical shift anisotropy (CSA) have been routinely assessed in singly labeled protein samples by the high-resolution separated local field (SLF) techniques (14-21). Using the two-dimensional Os- NMR spectra, many MP structures have been determined (6, 9, 22-30). However, while being efficient for determining the tilts of short alpha-helical peptides within the membrane, the ^1H - ^{15}N dipolar and ^{15}N CSA frequencies by themselves are insufficient for determining protein structures of arbitrary topology. Structure determination of membrane proteins by Os-NMR will likely require measurements of additional angular restraints, for which doubly (^{15}N , ^{13}C) labeled protein samples would need to be employed. Computer simulations of

fitting synthetic multidimensional Os-NMR data (31, 32) have identified the $^1\text{H}_\alpha$ - $^{13}\text{C}_\alpha$ dipolar couplings as a critical third spectroscopic dimension, which can enable elucidation of the backbone folds of MPs without assuming any secondary structure elements *a priori*. The chiral nature of the $^1\text{H}_\alpha$ - $^{13}\text{C}_\alpha$ dipolar couplings in the predominantly L-amino acids largely removes the orientational degeneracy associated with the second-rank ^1H - ^{15}N dipolar and ^{15}N chemical shift interactions. However, for the uniformly doubly labeled samples the presence of the abundant ^{13}C spins represents an essential complication arising from the ^{13}C - ^{13}C homonuclear couplings, which broaden NMR linewidths and, thus, negatively affect spectroscopic resolution. Previous attempts of accessing the $^1\text{H}_\alpha$ - $^{13}\text{C}_\alpha$ couplings in oriented membrane proteins involved either natural abundance crystal samples (33) or selective incorporation of ($^{13}\text{C}_\alpha$, ^{15}N) labeled amino acids (34), which can be prohibitively expensive for larger proteins. Moreover, not all ($^{13}\text{C}_\alpha$, ^{15}N) isotopically labeled amino acids are available commercially. Therefore, in order to measure $^1\text{H}_\alpha$ - $^{13}\text{C}_\alpha$ couplings, radically new pulse sequences need to be developed that would be generally applicable to uniformly doubly labeled membrane proteins.

Here we present a triple-resonance pulse sequence that enables detection of the $^1\text{H}_\alpha$ - $^{13}\text{C}_\alpha$ couplings at the ^{15}N amide sites for a uniaxially aligned protein NMR sample. The performance of the pulse sequence has been tested numerically and by using a uniformly (^{15}N , ^{13}C) doubly labeled Pf1 phage coat protein reconstituted in magnetically aligned bicelles. Pf1 coat protein, the major coat protein of Pf1 bacteriophage, represents an ideal test system for methods development in Os-NMR as its transmembrane domain has a well-characterized α -helix conformation, and its Os-NMR spectra have been unambiguously assigned using both selective labeling and the α -helical peak patterns (25) and spectroscopic techniques (35, 36). Moreover, recently the Pf1 spectroscopic assignment was confirmed by an automated assignment algorithm

(37). For such a short transmembrane domain (22 residues), by matching the ^{15}N chemical shifts in the ^1H - ^{15}N and $^1\text{H}_\alpha$ - $^{13}\text{C}_\alpha$ experiments, the latter dipolar couplings can be directly assigned. All the three measurements per peptide plane have been fitted simultaneously to a consensus α -helical transmembrane structure for Pfl coat protein, without assuming the fold *a priori*. The $^1\text{H}_\alpha$ - $^{13}\text{C}_\alpha$ dipolar couplings represent powerful chiral restraints for structure determination of membrane proteins in oriented lipid bilayers, thus greatly enhancing the utility of the OS NMR as a structural characterization method for membrane proteins in native-like lipid environments.

4.3 Methods

Simulations and Structure Calculations

Numerical simulations of pulse sequence on many-spin systems were performed using an in-house MATLAB script (Mathworks, Inc.). Structural calculations were carried out using the python scripts (see Appendix C)

Sample Preparation

Uniformly ^{13}C , ^{15}N labeled Pfl coat protein was reconstituted in a lipid bilayer (*Pfl in bicelles*). About 4.0 mg of doubly-labelled Pfl coat protein was obtained from the phage sample following the previous protocol (38) using Pfl minimal media containing ^{13}C D-Glucose and $^{15}\text{NH}_4\text{Cl}$ for uniform labeling. The uniformly doubly labeled Pfl was reconstituted in 170 μL of DMPC/DHPC bicelle formed in 0.2 molar HEPES buffer at pH = 8.0. 0.05 % w/v of NaN_3 was added to the bicelle sample to prevent bacteria growth. The total w/v ratio was 28% for the lipids, the lipid molar ratio q was 3.2 and the lipid-to-protein ratio was about 80:1.

NMR spectroscopy

The NMR experiments were performed on a Bruker Avance II spectrometer operating at the ^1H NMR frequency of 500 MHz and the data were acquired using the TopspinTM 2.0 software. The 90-degree pulse was calibrated at $B_1=50$ kHz for all three channels. The ^{13}C decoupling frequency was set at 100 ppm, and the ^1H frequency was set to 10 ppm. The NMR samples were sealed in a 5 mm New EraTM glass tube and placed inside 5 mm inner round coil of a static triple resonance $^1\text{H}/^{15}\text{N}/^{31}\text{P}$ Bruker 5 mm E-freeTM probe. The temperature was set at 37°C for the sample of Pfl in bicelles, yielding optimal bicelle alignment as monitored by ^{31}P NMR linewidths.

4.4 Results

Our developed pulse sequence, recoupling the $^1\text{H}_\alpha\text{-}^{13}\text{C}_\alpha$ dipolar interactions while eliminating the $^{13}\text{C}\text{-}^{13}\text{C}$ and $^1\text{H}\text{-}^1\text{H}$ dipolar couplings, is shown in Fig. 4.1. The pulse sequence consists of three blocks: (i) Evolution of $^1\text{H}_\alpha\text{-}^{13}\text{C}_\alpha$ couplings under both $^1\text{H}\text{-}^1\text{H}$ and $^{13}\text{C}\text{-}^{13}\text{C}$ homonuclear decoupling; (ii) Proton-mediated magnetization transfer of ^{13}C dipolar evolution to the proximal ^{15}N sites; (iii) Detection at the ^{15}N spin sites. The first part is achieved by essentially applying two SAMPI4 blocks (18) on both channels, hence the pulse sequence was named SAMPI4². In order to refocus the ^{13}C shift evolution and the secular, i.e. $I_z S_z$, part of the $^1\text{H}\text{-}^{13}\text{C}$ dipolar Hamiltonian, an additional refocusing π_y pulse has been inserted on the ^{13}C channel. The proton-mediated transfer under mismatched Hartmann-Hahn (MMHH) conditions (39) provides selective magnetization transfer from the nearest $^1\text{H}_\alpha\text{-}^{13}\text{C}_\alpha$ couplings to the amide ^{15}N sites, due to truncation of the dipolar interactions coming from more distant ^{13}C spins in the doubly tilted rotating frame approximation.

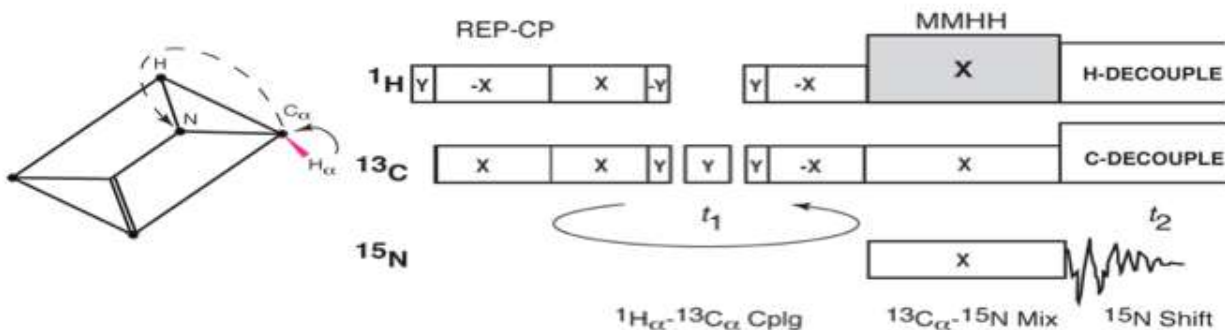


Figure 4.1. The developed pulse sequence for detecting $^1\text{H}\alpha$ - $^{13}\text{C}\alpha$ couplings at ^{15}N sites suitable for uniformly labeled (^{15}N , ^{13}C) aligned samples.

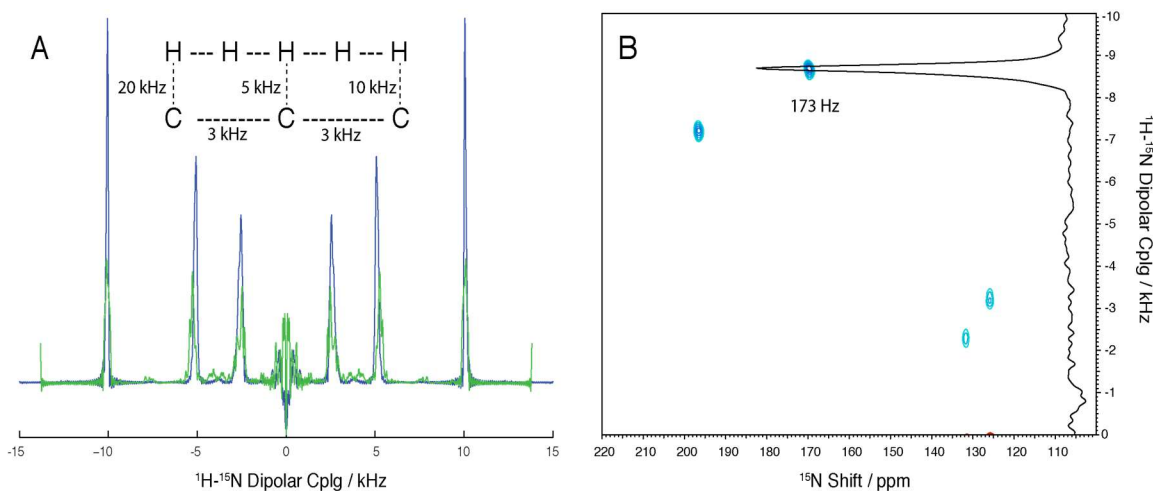


Figure 4.2. A. Simulation of the pulse sequences SAMPI4² (blue) and SAMPI4 (green) for an 8-spin system at B_1 rf field of 60 kHz with the dipolar couplings as indicated in the inset. B. Experimental SAMPI4² spectrum exhibits good dipolar resolution (ca. 200 Hz FWHH linewidths) when applied to ^{15}N labeled n-Acetyl Leucine single crystal.

Simulations of the SAMPI4² pulse sequence show superior resolution and intensity as compared to SAMPI4 when both the low- and high-spin homonuclear dipolar couplings are present, cf. Fig. 4.2A. The spin system with the relevant dipolar constants is outlined in the inset. As can be seen, the SAMPI4² pulse sequence correctly evolves simultaneously all three desired heteronuclear

couplings of 5, 10 and 20 kHz, which were pre-defined in the spin system. The individual subdwelt timings for SAMPI4² were set to the same timings as in SAMPI4. The effective dwell time for the SAMPI4² sequence was determined numerically to be near $8t_{90}$ (in terms of the 90-degree pulse). By contrast, SAMPI4 simulations for the same spin system show additional line-broadening and splittings of the main doublets due to the presence of the ¹³C-¹³C dipolar interactions. Figure 4.2.B illustrates that the new SAMPI4² pulse sequence provides good homonuclear decoupling when the low-spin homonuclear interactions are absent. Experimental SAMPI4² spectrum of ¹⁵N-labeled n-acetyl Leucine single crystal exhibits sharp dipolar linewidths, comparable to the SAMPI4 pulse sequence.

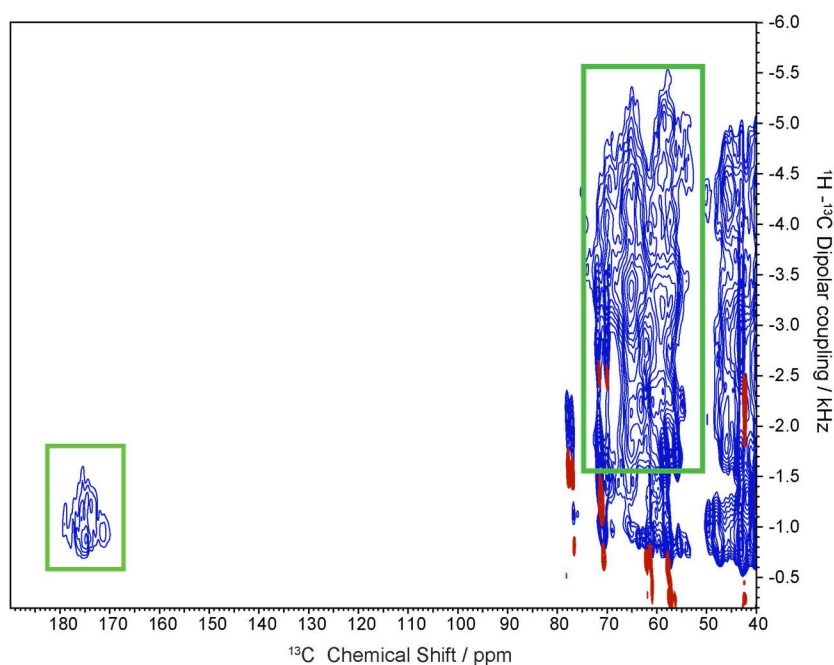


Figure 4.3. ¹³C-detected 2D SAMPI4 spectra of Pfl coat protein reconstituted in magnetically aligned DMPC/DHPC bicelles correlating ¹H-¹³C dipolar couplings with ¹³C chemical shifts (blue contours). Blank DMPC-DHPC bicelle SAMPI4 spectrum is shown as red contours for direct comparison. The identified ¹³C resonances originating from the C_α carbons and the Carbonyl of Pfl protein are outlined by the green boxes.

Carbon-detected Os-NMR spectra of uniformly ^{13}C -labeled samples typically exhibit insufficient resolution due to peak crowding and broad linewidths, but nevertheless can be used for identifying the expected range for the $^1\text{H}_\alpha$ - $^{13}\text{C}_\alpha$ couplings present in membrane proteins reconstituted in magnetically aligned bicelles. Shown in Fig. 4.3 is the SAMPI4 spectrum of the Pf1 coat protein sample in DMPC/DHPC bicelles. By directly comparing the blank bicelle spectrum arising from the natural-abundance ^{13}C spins (red) with the protein-containing sample (blue), the $^1\text{H}_\alpha$ - $^{13}\text{C}_\alpha$ dipolar resonances in the α -carbon aliphatic region (ca. 50-70 ppm) can be identified (shown by the green boxes), exhibiting the range for the expected values between ca. 1.5 and 5.5 kHz, in agreement with an earlier work (34)

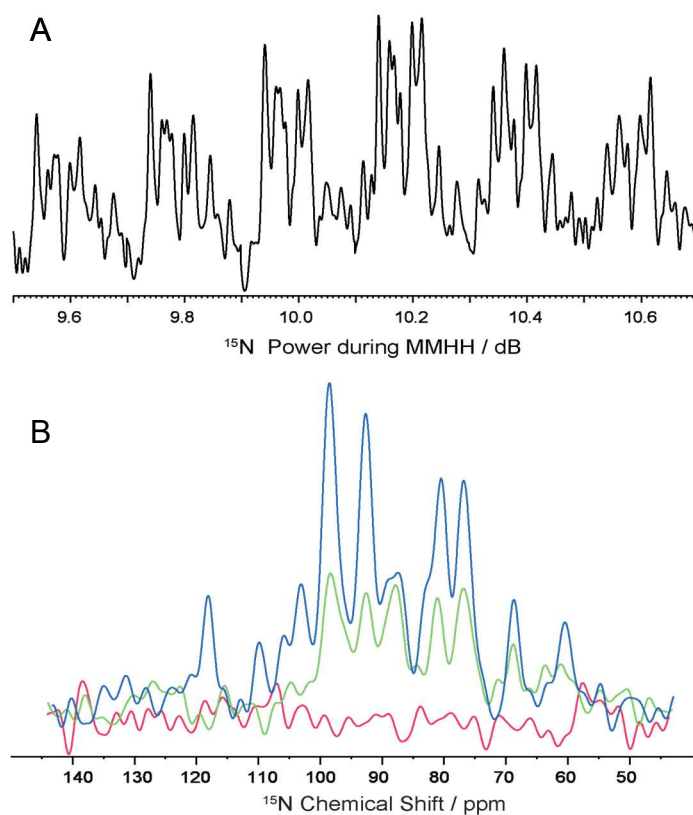


Figure 4.4. A. Optimization of the triple MMHH conditions using ^{15}N -detected magnetization transfer from the ^{13}C spins. B. ^{15}N detected MMHH transfer spectra with proton channel power on (blue) and only the proton power off (green) and with only the carbon power off (red).

The $^{13}\text{C}/^1\text{H}$ Hartmann-Hahn matching condition was determined using both ^{13}C and ^{15}N detected experiments; the latter method essentially corresponds to the first t_1 point of the two-dimensional SAMPI4² sequence, cf. Fig 4.1. To verify that all the ^{15}N -detected magnetization was originating from the ^{13}C spins, a series of control experiments have been performed. First, the rf amplitude on the ^{15}N channel was optimized to ensure the maximum ^{13}C - ^{15}N transfer efficiency using the first t_1 point of SAMPI4². During the optimization of the triple MMHH transfer, the rf amplitude on the ^{13}C channel was fixed while the proton rf power was kept constant, with the B_1 field being approximately 5 kHz above the $^{13}\text{C}/^1\text{H}$ Hartmann-Hahn matching condition (35). Owing to the relatively low efficiency of the MMHH transfer, 2048 scans were employed for the optimization. As can be seen from Fig 4.4A, a distinct intensity maximum emerges. The final optimal rf B_1 amplitudes calibrated for the triple MMHH transfer were ca. 28 kHz (^{13}C), 30 kHz (^{15}N), and 35 kHz (^1H). Furthermore, when the spin-lock rf field on the ^{13}C channel was removed, there was no signal observed from the ^{15}N spins, indicating that the magnetization detected at the ^{15}N channel was indeed originating from the ^{13}C spins. As the next step, the MMHH transfer efficiency was monitored with and without the rf power on the ^1H channel. As can be seen from Fig. 4.4B, adding the rf spin lock on the ^1H spin improves the magnetization transfer efficiency by at least two-fold, thus confirming the proton-mediated nature of the triple-resonance MMHH transfer.

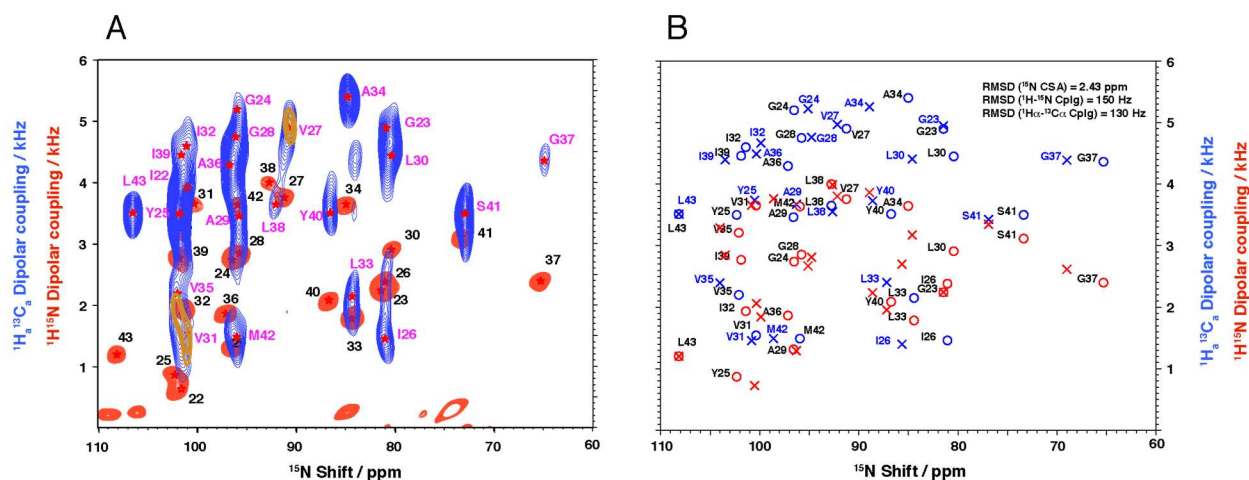


Figure 4.5. A. Overlay of ^{15}N -detected SLF $^1\text{H}-^{15}\text{N}$ (red contours) and $^1\text{H}\alpha-^{13}\text{C}\alpha$ dipolar couplings (blue contours) measured for doubly labeled sample of Pf1 coat protein reconstituted in magnetically aligned bicelles. Selectively labeled ($^{13}\text{C}_\alpha$, ^{15}N) Valine spectrum is shown in brown contours. Assignment of the $^1\text{H}\alpha-^{13}\text{C}\alpha$ dipolar couplings is shown by the text in magenta color. B. Structural fitting of the digitized data (circles) showing the fitted frequency values (crosses).

Figure 4.5A shows an overlay of two-dimensional ($^1\text{H}\alpha-^{13}\text{C}\alpha / ^{15}\text{N}$) SAMPI4² and ($^1\text{H}-^{15}\text{N}/^{15}\text{N}$) SAMPI4 spectra with ^{13}C SPINAL32 decoupling (40) added during the ^{15}N CSA acquisition. To enhance the signal intensity, four consecutively run SAMPI4² spectra were co-added with 40 t_1 points acquired at 1k scans each. As an additional control, SAMPI4² was run to evolve the $^1\text{H}-^{15}\text{N}$ dipolar couplings under ^{13}C decoupling and gave almost identical results with SAMPI4 for both a single crystal of n-acetyl Leucine and Pf1 (not shown). The ($^1\text{H}\alpha-^{13}\text{C}\alpha / ^{15}\text{N}$) SAMPI4² spectrum of Pf1 is shown in blue and the ($^1\text{H}-^{15}\text{N}/^{15}\text{N}$) SAMPI4 spectrum is shown in red. The assignments of ($^1\text{H}\alpha-^{13}\text{C}\alpha / ^{15}\text{N}$) peaks are shown in Fig. 4.5A by the text in magenta, denoting both the residue type and its number; the well-established ($^1\text{H}-^{15}\text{N}/^{15}\text{N}$) assignment is denoted here just by the residue numbers for brevity. Many of the SAMPI4² peaks can be immediately assigned from the ($^1\text{H}-^{15}\text{N}/^{15}\text{N}$) SAMPI4 spectra by relating their corresponding ^{15}N

chemical shifts. Assignments of some peaks required extra discernment. For instance, we have measured a selectively ($^{13}\text{C}_\alpha$, ^{15}N) Valine-labeled spectrum to delineate between the peaks in the crowded region at ca. 102 ppm (shown as brown contours in Fig. 4.5A). This allowed us to identify the Valine peaks and restrict the assignment possibilities for other residues. Other assignments can be resolved in a similar manner, i.e. by invoking selective labeling. Clearly, three-dimensional correlation NMR spectra would be required for the spectroscopic assignment in the general case, which will be deferred to subsequent publications. However, the current signal-to-noise ratio would likely preclude any three-dimensional NMR experiments for spectroscopic assignment, with the available field strength corresponding to 500 MHz ^1H frequency. Of special note are the Glycine $^1\text{H}_\alpha$ - $^{13}\text{C}_\alpha$ peaks as the α -carbon is bonded to both H_α and H_β protons. The dipolar frequencies for such a three-spin system follow the “hypotenuse” relation in the doubly tilted rotating frame (41), viz.:

$$v_{^1\text{H}-^{13}\text{C}}(\text{Gly}) = \sqrt{v_{^1\text{H}_\alpha-^{13}\text{C}_\alpha}^2 + v_{^1\text{H}_\beta-^{13}\text{C}_\alpha}^2} \quad \text{Eq 1}$$

As a consequence, the Glycine $^1\text{H}_\alpha$ - $^{13}\text{C}_\alpha$ dipolar couplings are much larger than their corresponding ^1H - ^{15}N interactions, which facilitates their assignment. The hypotenuse relation, Eq. (1), must also be taken into account during the structural fitting.

Figure 4.5B shows the structural fitting of the centers of the peaks identified in Fig. 4.5A and digitized by circles. The fitted frequencies are shown by crosses. The data were fitted for residues G23 through L43 corresponding to the transmembrane domain of Pfl coat protein. The structure fitting was performed using the algorithm developed in previous work (32). Briefly, the algorithm iteratively finds the values for *two* pairs of torsion angles (Φ and Ψ) that are consistent with *two* sets of NMR angular restraints (in this case ^{15}N CSA, ^1H - ^{15}N and, $^1\text{H}_\alpha$ - $^{13}\text{C}_\alpha$ dipolar

couplings) amongst *three* adjacent peptide planes. Fitting simultaneously the torsion angles for three adjacent planes, instead of two, alleviates the problem of overfitting some resonances at the expense of others and greatly reduces propagation of error. The frequencies ν_{\parallel} for the parallel orientation (i.e. used in the fitting) are related to the perpendicular values, ν_{\perp} (i.e. experimentally measured in bicelles) by the “Bicelle Equation” (42), viz.:

$$\nu_{\parallel} = \nu_{iso} + \frac{2}{S_O}(\nu_{iso} - \nu_{\perp}) \quad \text{Eq 2}$$

Here the order parameter was set to $S_O = 0.8$, and ν_{iso} is the corresponding isotropic frequency (which is zero for the dipolar couplings). The root-mean-square deviations of the fitted frequencies to the spectra are given as an inset. It can be seen that the rms deviations do not exceed 150 Hz in all three spectroscopic dimensions. It should also be noted that for the structural fitting we have used experimental isotropic ^{15}N chemical shifts for Pfl coat protein in isotropic micelles (36) and the linear regression plots for the individual tensor values σ_{11} , σ_{22} , and σ_{33} (43). Correcting the individual CSA values from their commonly used average values was found to improve the overall quality of the structural fit in the ^{15}N chemical shift dimension

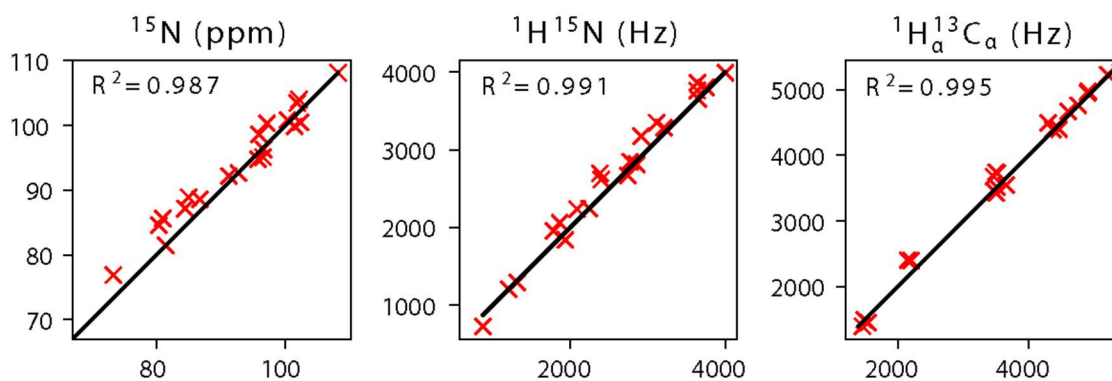


Figure 4.6. Linear-regression correlation plots for the simultaneously fitted ^{15}N CSA and $^1\text{H}-^{15}\text{N}$ and $^1\text{H}\alpha-^{13}\text{C}\alpha$ couplings for Pfl coat protein.

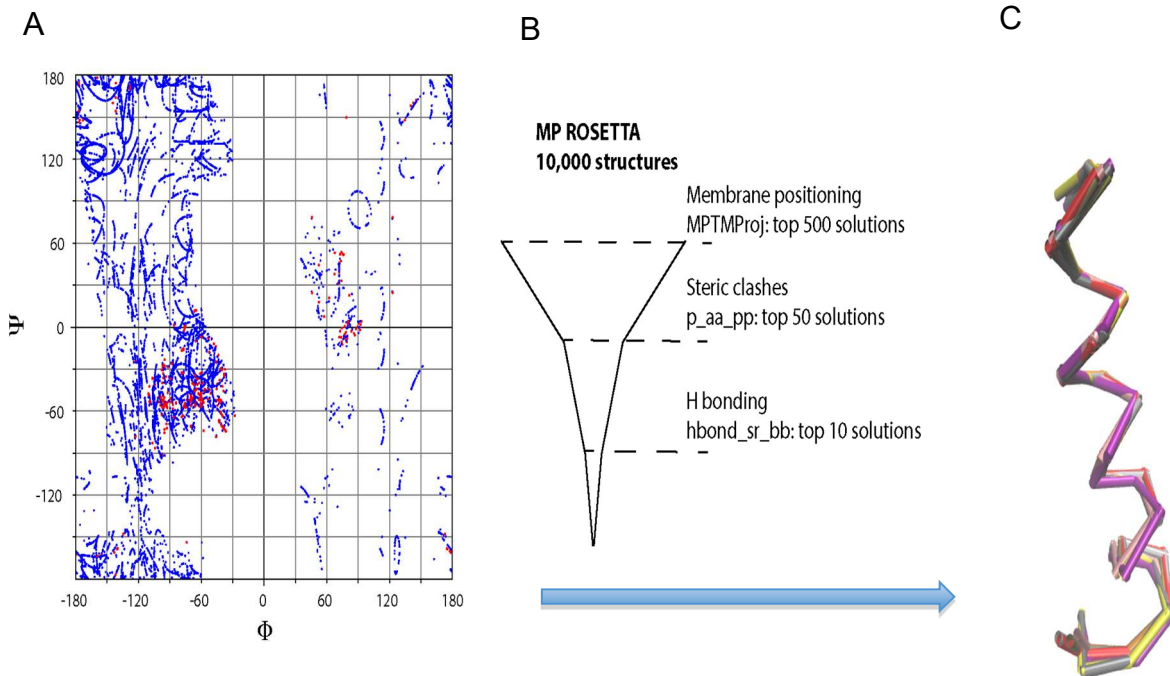


Figure 4.7 A. Final search values for torsion angles on the Ramachandran map for 2D vs 3D NMR data fit for 1000 calculated structures. A clustering near the α -helical torsion angles is apparent for the 3D fit. No restriction on the torsion angles was assumed a priori for the fitting. B. ROSETTA top-down filtering protocol. C. Consensus family of Pf1 TM structures determined from NMR.

Ten thousand (10,000) structural solutions satisfying the three experimental angular restraints have been calculated. Representative linear regression plots for the fitted vs. experimental data for the three spectroscopic dimensions are shown in Fig. 4.6 demonstrating good quality of the fit. It should be emphasized that during the fitting, instead of biasing the search to specific secondary structural preferences, the starting values for the torsion angles of Φ and Ψ were randomized between -180 and 180 degrees. Fig. 4.7A shows the distributions of the final (i.e. fitted) torsion angles over the Ramachandran map for 1,000 structures. Shown in red are the values obtained from fitting three angular constraints per plane (denoted as 3D). Shown

in blue for comparison are the fitted values from using just the two “traditional” ^1H - ^{15}N dipolar and ^{15}N CSA NMR dimensions (2D). As can be seen, the torsion angles from the 3D fit are predominantly clustered near the alpha-helical values, i.e. $\Phi=-61^\circ$; $\Psi=-45^\circ$, whereas the final angles from the 2D fit are scattered over a much broader range of the ramachandran map (while still producing good fits to the NMR data). The final step was to perform a top-down filtering of the calculated 10,000 structures using three MP Rosetta scoring terms, cf. Fig. 4.7B. The first step in the filtering procedure included the membrane positioning scoring function, MPTMProj, (44) from which the top 500 solutions were collected. The filtering procedure then followed by scoring the solution for sound backbone torsion preferences, p_aa_pp, (45) and choosing the top 50 solutions amongst the prior 500. Finally, the hydrogen bonding scoring function, hbond_sr_bb (46) was applied, which resulted in the final 10 solutions shown in Fig. 4.7C. The final structure indeed results in an α -helix with a slightly unstructured N-terminal part containing the G23 and G24 residues. In passing we note that a deliberate switching of some of the $^1\text{H}_\alpha$ - $^{13}\text{C}_\alpha$ dipolar assignments in Fig. 4.5A did not produce any meaningful, high-scoring structures. The slight unwinding of the helix at the N terminus is consistent with the pattern for the ^1H - ^{15}N dipolar couplings for Pfl reconstituted in perpendicularly aligned DMPC/DHPC bicelles, (cf. Fig. 6a of ref. (47)) which demonstrate that these residues do not line up well with the “dipolar wave” of periodicity 3.6 (48). Interestingly, the ideal alpha helical structure appears to be much more persistent in detergent DHPC micelles as evident from the solution NMR RDC dipolar waves for Pfl coat protein (25). A detailed discussion on the origin of this possible discrepancy is beyond the scope of the present paper.

4.5 Conclusions

We have demonstrated, for the first time, that backbone folds of MPs can be experimentally determined by fitting simultaneously three angular restraints per peptide plane and, notably, an α -helical configuration does not need to be assumed *a priori*. The experimental restraints consisted of $^1\text{H}_\alpha$ - $^{13}\text{C}_\alpha$ and ^1H - ^{15}N dipolar couplings and ^{15}N CSA. We have developed a new pulse sequence recoupling the $^1\text{H}_\alpha$ - $^{13}\text{C}_\alpha$ dipolar interactions while eliminating the ^{13}C - ^{13}C and ^1H - ^1H dipolar couplings. MMHH transfer ensures selective proton-mediated transfer from the nearest $^1\text{H}_\alpha$ - $^{13}\text{C}_\alpha$ couplings to the amide ^{15}N sites. The pulse sequence has been tested by performing many-spin simulations and by recalculating the known structure of TM domain of Pfl coat protein reconstituted in magnetically aligned bicelles. Moreover, the measured $^1\text{H}_\alpha$ - $^{13}\text{C}_\alpha$ couplings are consistent with the α -helical structure of Pfl, which provides an additional validation of our experimental method. Furthermore, a consensus structure for Pfl TM domain has been calculated by determining the torsion angles using three angular restraints per peptide plane. Including the third, chiral $^1\text{H}_\alpha$ - $^{13}\text{C}_\alpha$ dimension allows one to search for the torsion solutions over the full range of the Ramachandran map, without restricting the torsion angles to an α -helical range, as is necessary when considering only two angular restraints per peptide plane. This new method uniquely positions oriented-sample NMR as a “crystallography” tool in aligned, lipid-rich bilayers at near-physiological conditions. The results advance NMR of uniaxially aligned samples to a new quantitative level and pave way for structure determination of membrane proteins from three-dimensional experiments performed on uniformly doubly labeled samples.

REFERENCES

1. White, S. H., & Wimley, W. C. (1999). Membrane protein folding and stability: Physical principles. *Annual Review of Biophysics and Biomolecular Structure*, 28, 319-365.
2. Lee, A. G. (2011). Lipid-protein interactions. *Biochemical Society Transactions*, 39(3), 761-766.
3. Laganowsky, A., Reading, E., Allison, T. M., Ulmschneider, M. B., Degiacomi, M. T., Baldwin, A. J., & Robinson, C. V. (2014). Membrane proteins bind lipids selectively to modulate their structure and function. *Nature*, 510(7503), 172-175.
4. Hamilton, P. J., Belovich, A. N., Khelashvili, G., Saunders, C., Erreger, K., Javitch, J. A., Sitte, H. H., Weinstein, H., Matthies, H. J. G., & Galli, A. (2014). PIP2 regulates psychostimulant behaviors through its interaction with a membrane protein. *Nature Chemical Biology*, 10(7), 582-589.
5. Martens, C., Stein, R. A., Masureel, M., Roth, A., Mishra, S., Dawaliby, R., Konijnenberg, A., Sobott, F., Govaerts, C., & McHaourab, H. S. (2016). Lipids modulate the conformational dynamics of a secondary multidrug transporter. *Nature Structural & Molecular Biology*, 23(8), 744-751.
6. Traaseth, N. J., Shi, L., Verardi, R., Mullen, D. G., Barany, G., & Veglia, G. (2009). Structure and topology of monomeric phospholamban in lipid membranes determined by a hybrid solution and solid-state NMR approach. *Proceedings of the National Academy of Sciences of the United States of America*, 106(25), 10165-10170.
7. Shi, L. C., Lake, E. M. R., Ahmed, M. A. M., Brown, L. S., & Ladizhansky, V. (2009). Solid-state NMR study of proteorhodopsin in the lipid environment: Secondary structure and dynamics. *Biochimica Et Biophysica Acta-Biomembranes*, 1788(12), 2563-2574.
8. Cady, S. D., Schmidt-Rohr, K., Wang, J., Soto, C. S., DeGrado, W. F., & Hong, M. (2010). Structure of the amantadine binding site of influenza M2 proton channels in lipid bilayers. *Nature*, 463(7281), 689-692.
9. Sharma, M., Yi, M. G., Dong, H., Qin, H. J., Peterson, E., Busath, D. D., Zhou, H. X., & Cross, T. A. (2010). Insight into the Mechanism of the Influenza A Proton Channel from a Structure in a Lipid Bilayer. *Science*, 330(6003), 509-512.
10. Park, S. H., Das, B. B., Casagrande, F., Tian, Y., Nothnagel, H. J., Chu, M. N., Kiefer, H., Maier, K., De Angelis, A. A., Marassi, F. M., & Opella, S. J. (2012). Structure of the chemokine receptor CXCR1 in phospholipid bilayers. *Nature*, 491(7426), 779-783.
11. Renault, M., Bos, M. P., Tommassen, J., & Baldus, M. (2011). Solid-State NMR on a Large Multidomain Integral Membrane Protein: The Outer Membrane Protein Assembly Factor BamA. *Journal of the American Chemical Society*, 133(12), 4175-4177.

12. Wang, S. L., Munro, R. A., Shi, L. C., Kawamura, I., Okitsu, T., Wada, A., Kim, S. Y., Jung, K. H., Brown, L. S., & Ladizhansky, V. (2013). Solid-state NMR spectroscopy structure determination of a lipid-embedded heptahelical membrane protein. *Nature Methods*, *10*(10), 1007-1012.
13. Elkins, M. R., Williams, J. K., Gelenter, M. D., Dai, P., Kwon, B., Sergeyev, I. V., Pentelute, B. L., & Hong, M. (2017). Cholesterol-binding site of the influenza M2 protein in lipid bilayers from solid-state NMR. *Proceedings of the National Academy of Sciences of the United States*, *114*(49), 12946-12951.
14. Wu, C. H., Ramamoorthy, A., & Opella, S. J. (1994). High-resolution heteronuclear dipolar solid-state NMR spectroscopy. *Journal of Magnetic Resonance Series A*, *109*(2), 270-272.
15. Dvinskikh, S. V., & Sandström, D. (2005). Frequency offset refocused PISEMA-type sequences. *Journal of Magnetic Resonance*, *175*(1), 163-169.
16. Dvinskikh, S. V., Yamamoto, K., & Ramamoorthy, A. (2006). Heteronuclear isotopic mixing separated local field NMR spectroscopy. *The Journal of Chemical Physics*, *125*(3), 034507.
17. Nevzorov, A. A., & Opella, S. J. (2003). A "Magic Sandwich" pulse sequence with reduced offset dependence for high-resolution separated local field spectroscopy. *Journal of Magnetic Resonance*, *164*(1), 182-186.
18. Nevzorov, A. A., & Opella, S. J. (2007). Selective averaging for high-resolution solid-state NMR spectroscopy of aligned samples. *Journal of Magnetic Resonance*, *185*(1), 59-70.
19. Gopinath, T., & Veglia, G. (2009). Sensitivity Enhancement in Static Solid-State NMR Experiments via Single- and Multiple-Quantum Dipolar Coherences. *Journal of the American Chemical Society*, *131*(16), 5754-5756.
20. Jayanthi, S., & Ramanathan, K. V. (2010). 2(n)-SEMA-a robust solid state nuclear magnetic resonance experiment for measuring heteronuclear dipolar couplings in static oriented systems using effective transverse spin-lock. *Journal of Chemical Physics*, *132*(13), 134501.
21. Jayanthi, S., Sinha, N., & Ramanathan, K. V. (2010). 2(4)-SEMA as a sensitive and offset compensated SLF sequence. *Journal of Magnetic Resonance*, *207*(2), 206-212.
22. Park, S. H., De Angelis, A. A., Nevzorov, A. A., Wu, C. H., & Opella, S. J. (2006). Three-Dimensional Structure of the Transmembrane Domain of Vpu from HIV-1 in Aligned Phospholipid Bicelles. *Biophysical Journal*, *91*(8), 3032-3042.

23. De Angelis, A. A., Howell, S. C., Nevzorov, A. A., & Opella, S. J. (2006). Structure Determination of a Membrane Protein with Two Trans-membrane Helices in Aligned Phospholipid Bicelles by Solid-state NMR Spectroscopy. *Journal of the American Chemical Society*, *128*(37), 12256-12267.
24. Mahalakshmi, R. & Marassi, F. M. (2008). Orientation of the Escherichia coli outer membrane protein OmpX in phospholipid bilayer membranes determined by solid-state NMR. *Biochemistry*, *47*(25), 6531-6538.
25. Park, S. H., Marassi, F. M., Black, D., & Opella, S. J. (2010). Structure and Dynamics of the Membrane-Bound Form of Pfl Coat Protein: Implications of Structural Rearrangement for Virus Assembly. *Biophysical Journal*, *99*(5), 1465-1474.
26. Mote, K. R., Gopinath, T., Traaseth, N. J., Kitchen, J., Gor'kov, P. L., Brey, W. W., & Veglia, G. (2011). Multidimensional oriented solid-state NMR experiments enable the sequential assignment of uniformly N-15 labeled integral membrane proteins in magnetically aligned lipid bilayers. *Journal of Biomolecular NMR*, *51*(3), 339-346.
27. Gleason, N. J., Vostrikov, V. V., Greathouse, D. V., & Koeppe, R. E. (2013). Buried lysine, but not arginine, titrates and alters transmembrane helix tilt. *Proceedings of the National Academy of Sciences of the United States*, *110*(5), 1692-1695.
28. Gayen, A., Banigan, J. R., & Traaseth, N. J. (2013). Ligand-Induced Conformational Changes of the Multidrug Resistance Transporter EmrE Probed by Oriented Solid-State NMR Spectroscopy. *Angewandte Chemie (International ed in English)*, *52*(39), 10321-10324.
29. Yamamoto, K., Gildenberg, M., Ahuja, S., Im, S. C., Percy, P., Waskell, L., & Ramamoorthy, A. (2013). Probing the Transmembrane Structure and Topology of Microsomal Cytochrome-P450 by Solid-State NMR on Temperature-Resistant Bicelles. *Scientific Reports*, *3*(2556), 1-6.
30. Murray, D. T., Li, C., Gao, F. P., Qin, H., & Cross, T. A. (2014). Membrane Protein Structural Validation by Oriented Sample Solid-State NMR: Diacylglycerol Kinase. *Biophysical Journal*, *106*(8), 1559-1569.
31. Yin, Y. Y., & Nevzorov, A. A. (2011). Structure Determination in "Shiftless" Solid State NMR of Oriented Protein Samples. *Journal of Magnetic Resonance*, *212*(1), 64-73.
32. Lapin, J., Nevzorov, A. A. 2019. Validation of protein backbone structures calculated from NMR angular restraints using Rosetta. *Journal of Biomolecular NMR*, *73*(5), 229-244.
33. Gu, Z. T., & Opella, S. J. (1999). Two- and three-dimensional ¹H-¹³C PISEMA experiments and their application to backbone and side chain sites of aminoacids and peptides. *Journal of Magnetic Resonance*, *140*(2), 340-346.

34. Sinha, N., Grant, C. V., Park, S. H., Brown, J. M., & Opella, S. J. (2007). Triple resonance experiments for aligned sample solid-state NMR of C-13 and N-15 labeled proteins. *Journal of Magnetic Resonance*, 186(1), 51-64.
35. Tang, W. X., Knox, R. W., and Nevzorov, A. A. (2012). A spectroscopic assignment technique for membrane proteins reconstituted in magnetically aligned bicelles. *Journal of Biomolecular NMR*, 54(3), 307-316.
36. Lu, G. J., & Opella, S. J. (2014). Resonance assignments of a membrane protein in phospholipid bilayers by combining multiple strategies of oriented sample solid-state NMR. *Journal of Biomolecular NMR*, 58(1), 69-81.
37. Lapin, J., & Nevzorov, A. A. (2018). Automated assignment of NMR spectra of macroscopically oriented proteins using simulated annealing. *Journal of Magnetic Resonance*, 293, 104-114.
38. Thiriot, D. S., Nevzorov, A. A., Zagayanskiy, L., Wu, C. H., & Opella, S. J. (2004). Structure of the coat protein in Pfl bacteriophage determined by solid-state NMR spectroscopy. *Journal of Molecular Biology*, 341(3), 869-879.
39. Nevzorov, A. A. (2008). Mismatched Hartmann-Hahn Conditions Cause Proton-Mediated Intermolecular Magnetization Transfer Between Dilute Low Spin Nuclei in NMR of Static Solids. *Journal of the American Chemical Society*, 130(34), 11282–11283.
40. Fung, B. M., Khitritin, A. K., & Ermolaev, K. (2000). An improved broadband decoupling sequence for liquid crystals and solids. *Journal of Magnetic Resonance*, 142(1), 97-101.
41. Gan, Z. (2000). Spin dynamics of polarization inversion spin exchange at the magic angle in multiple spin systems. *Journal of Magnetic Resonance*, 143(1), 136-143.
42. De Angelis, A. A., Nevzorov, A. A., Park, S. H., Howell, S. C., Mrse, A. A., & Opella, S. J. (2004). High-resolution NMR spectroscopy of membrane proteins in "unflipped" bicelles. *Journal of the American Chemical Society*, 126(47), 15340-15341.
43. Paramasivam, S., Gronenborn, A. M., & Polenova, T. (2018). Backbone amide N-15 chemical shift tensors report on hydrogen bonding interactions in proteins: A magic angle spinning NMR study. *Solid State Nuclear Magnetic Resonance*, 92, 1-6.
44. Yarov-Yarovoy, V., Schonbrun, J., & Baker, D. (2006). Multipass membrane protein structure prediction using Rosetta. *Proteins: Structure, Function and Bioinformatics*, 62(4), 1010-1025.
45. Leaver-Fay, A., O'Meara, M. J., Tyka, M., Jacak, R., Song, Y. F., Kellogg, E. H., Thompson, J., Davis, I. W., Pache, R. A., Lyskov, S., Gray, J. J., Kortemme, T., Richardson, J. S., Havranek, J. J., Snoeyink, J., Baker, D., & Kuhlman, B. (2013).

Scientific Benchmarks for Guiding Macromolecular Energy Function Improvement. In Keating, A. E. (ed.), *Methods in Enzymology*, 523, 109-143, Academic Press.

46. Shmygelska, A. & Levitt, M. (2009). Generalized ensemble methods for de novo structure prediction. *Proceedings of the National Academy of Sciences of the United States*, 106(5), 1415-1420.
47. Opella, S. J., Zeri, A. C., & Park, S. H. (2008). Structure, Dynamics, and Assembly of Filamentous Bacteriophages by Nuclear Magnetic Resonance Spectroscopy. *Annual Review of Physical Chemistry*, 59, 635–657.
48. Mesleh, M. F., & Opella, S. J. (2003). Dipolar Waves as NMR maps of helices in proteins. *Journal of Magnetic Resonance*, 163(2), 288-299.

APPENDICES

APPENDIX A

MATLAB codes for T1rho rotational diffusion calculation

Figure 3.3-3.6

```
clear all
[A1,A2]=xlsread('/Users/NevezorovLab/Desktop/T1_rho_Height data.xls');
time=[0 .005 .010 .015 .020 .025];
Int=A1(:,4:9);
DC=abs(A1(:,3));
for n=1:17
    Int_norm(n,:)=Int(n,:)/Int(n,1);
End

figure(1)
clf

Noise=141949;
err=Noise/Int(n,1)*ones(size(Int_norm(n,:)));
time_cont=linspace(0, 0.030, 1000);
zcolors=['g' 'r' 'm' 'c' 'y' 'b' 'k'];
size(Int_norm)
x0=[5e3, 10e-3];
for n=1:17
    [fitresult,goodness]=fit(time',Int_norm(n,:)','exp1','StartPoint',x0);
    x00=coeffvalues(fitresult);

    Ampl(n)=x00(1);
    T1rho(n)=-1/x00(2);

    dx00=confint(fitresult);

    dR1rho(n)=abs(x00(2)-dx00(1,2));
    dT1rho(n)=abs((1/x00(2))-(1/dx00(1,2)))
    plot(fitresult,time',Int_norm(n,:));
    hold on
    errorbar(time,Int_norm(n,:),err,'o');
end

figure (2)
clf
for n=1:17
    [fitresult,goodness]=fit(time',Int_norm(n,:)','exp1','StartPoint',x0);
    zcolors=['g' 'b' 'y' 'k' 'c' 'm'];
    n2plot=[1 3 6 11 13 17];
    if sum(n==n2plot)==1;
```

```

    plot(fitresult,time',Int_norm(n,:)','zcolors(mod(n,6)+1));
    hold on
    errorbar(time,Int_norm(n,:),err,'o','color',zcolors(mod(n,6)+1));
end
end

```

```

CSA=A1(:,2);
DIP=A1(:,3);

```

```

[A1,A2]=xlsread('/Users/NevezorovLab/Desktop/T1_rho_Height data.xls');
Dip=A1(:,3);
size(T1rho)
alpha=0.64*9*1e8*4*pi.^2/128;
size(alpha)
Dipmax=4000;
beta=2/3*(1-abs(Dip/Dipmax));
beta.^2;
Rrho=(1./T1rho);
size(Rrho)

```

```

P= polyfit(beta.^2,Rrho',1);

```

```

F1= polyval(P,beta.^2);
[r,m,b]=regression(beta.^2,Rrho','one')
alpha;
e = dR1rho;
Fresid=(Rrho'-F1);
ssresid=sum(Fresid.^2);
sstotal=(length(Rrho')-1)*var(Rrho');
rsq=(1-(ssresid/sstotal))

```

```

figure(3)
clf
plot(beta.^2,Rrho','o')
hold on
plot(beta.^2,F1,'r-');
errorbar(beta.^2,Rrho',e,'o')

```

```

F = @(x,xdata) 0.64*9e8*4*pi^2/(128*x(1))*(((1-(cos(x(2)*pi/180)*cos(15.8*pi/180)-
sin(x(2)*pi/180)*sin(15.8*pi/180)*cos(2*pi*xdata/3.6+x(3))).^2).^2)/(1+(2.2e10/x(1).^2).^1)+x(
4);

```

```

x0= [8e5, 22.28, -0.65, 23];
res=linspace(1,17,17);

```

```

[x,resnom1]=lsqcurvefit(F,x0,res,Rrho);

RMS=@(x) sum((F(x,res)-Rrho).^2);

x_l=[5e5, 22.25, -.7, 10];
x_u=[5e6, 22.29, -.6, 25];

[x,resnom1]=patternsearch(RMS,x0,[], [], [], [], x_l, x_u);

figure(4)
clf

Dpar=alpha/P(1)
Dpar1=x(1)
tilt=x(2)
phase=x(3)
offset=x(4)
rmsdlinear =resnom1

hold on

res_cont=linspace(1,17,170);
plot(25+res_cont,F(x,res_cont))

hold on
e = dR1rho;
plot(25+res, Rrho, 'o')
errorbar(25+res,Rrho,e,'o')

figure(5)
clf

plot(CSA, -DIP, 'o')

axis([50 120 0 5e3])
set(gca,'XDir','Reverse')
for n=1:17

    text(CSA(n)+1, -DIP(n), num2str(n+25));

end

(sum ((F(x,res)-Rrho).^2)/17).^0.5;

```

```
FDip = @(y,ydata) 1e4*(3*(cos(y(1)*pi/180)*cos(15.8*pi/180)-  
sin(y(1)*pi/180)*sin(15.8*pi/180)*cos(2*pi*ydata/3.6+y(2))).^2-1)*0.4/2;  
y0=[0,0];  
res=linspace(1,17,17);  
[y,resnom] =lsqcurvefit(FDip,y0,res,-Dip');
```

```
y(1)  
y(2)  
figure(6)  
clf
```

```
hold on  
plot(25+res, -Dip', 'o')
```

```
res_cont=linspace(1,17,170);  
plot(25+res_cont,FDip(y,res_cont))
```

APPENDIX B

Triple Resonance pulse program with SAMPI4² and MMHH Blocks:

```
1 ze ;
  t1incr

2 d1 do:f2
  1m do:f3
  10u p11:f1 p12:f2 p13:f3
  0.3u fq=cnst0:f3
  1m rpp4
  1m rpp5
  1m rpp6
  1m rpp7

;presaturation of 13C
(p5 ph1):f3
d7
(p5 ph1):f3

(p5 ph1 fq=cnst0):f2
(p15*0.33 ph3):f3 (p15*0.33 ph2):f2
(p15*0.33 ph2):f3 (p15*0.33 ph3):f2
(p15*0.33 ph3):f3 (p15*0.33 ph2):f2

; Multiple contacts with MOIST
3 (p3 ph8):f3 (p3 ph9):f2
  (d3 p5 ph10):f3 (d3 p5 ph1):f2
  (p15*0.33 ph3):f3 (p15*0.33 ph2):f2
  (p15*0.33 ph2):f3 (p15*0.33 ph3):f2
  (p15*0.33 ph3):f3 (p15*0.33 ph2):f2

lo to 3 times l22

; re-equilibration of the protons before the SAMPI4 evolution

if "l20<1" goto 5

;(p3 ph8):f3 (p3 ph9):f2
;(d6 p5 ph10):f3 (d6 p5 ph1):f2
; Magic Sandwich starts here
4 (p16 ph4):f3 (p16 ph4):f2
  (p3 ph11):f3 (p3 ph6 ipp6 ipp4):f2
  (d4 p3*2.0 ph11):f3
  (d4 p3 ph11):f3 (d4 p3 ph7 ipp7 ipp11):f2
```

(p16 ph5):f3 (p16 ph5 ipp5):f2
lo to 4 times l20

; Z-filter
5 (p3 ph8):f3
(d6 p5 ph10):f3

; MMHH
(p18 ph2 pl11):f1 (p18 ph2 pl14):f2 (p18 ph2 pl13):f3

0.3u fq=cnst21:f2
0.3u fq=cnst3:f3
0.3u pl33:f3

; detection
1u cpds2:f2
1u cpds3:f3
aq cpdngs30:f1
1m do:f3
1m do:f2
rcyc=2
1m do:f3
1m do:f2
100m wr #0 if #0 iu20 zd
lo to 2 times td1
exit

ph1=1 3
ph30=0
ph31=1 3
ph2=0
ph3=2
ph4=0 2
ph5=2 0 ; irradiation phases for the third part of the magic sandwich
ph6=1 3 ; phases for the first +-90Y pulse on the high side
ph7=3 1
ph8=3
ph9=3 1
ph10=1
ph11=1 3